THE UNIVERSITY OF CHICAGO

ENGINEERING THERMAL TRANSPORT IN 2D VAN DER WAALS CRYSTALLINE FILMS

A DISSERTATION SUBMITTED TO

THE FACULTY OF THE PRITZKER SCHOOL OF MOLECULAR ENGINEERING

IN CANDIDACY FOR THE DEGREE OF

DOCTOR OF PHILOSOPHY

BY

SHI EN KIM

CHICAGO, ILLINOIS

AUGUST 2022

To family, friends, and the underdogs of the world

TABLE OF CONTENTS

LIST OF FIGURES

LIST OF TABLES

ACKNOWLEDGEMENTS

It takes a village to raise a child, and it probably took a cavalcade to get this one through graduate school. Like any student, I first and foremost have to thank my graduate advisor, Prof. Jiwoong Park for shaping my entire graduate career. Many thanks also to my committee members, Prof. Alex High and Prof. Giulia Galli for your contributions towards my intellectual and personal growth. There's no experience like graduate school to beat humbleness into a person, an everyday reminder that a marathon of adversity breeds—forges—character.

Although graduate school wasn't easy, the last six years were all still worth it, for the folks I've crossed paths with. I've had the fortune of collaborating with the most revered experts of their respective fields: Prof. David G. Cahill of University of Illinois at Urbana-Champaign and Prof. Paul Erhart of Chalmers University, Sweden. A shoutout to Prof. Cahill, in particular—thank you for making me feel that my alternative career choice, science journalism, mattered to the world at large. And for your curiosity over the minutiae of my experiments, for your mischievousness to intellectualize our way out of more experiments.

Many thanks to my lab mates, who breathed fun and empathy into my six years in Chicago, making all the blood and sweat bearable. The infamous "Friday Movie Night Crew"—Fauzia, Josh, and Baorui (plus honorary members, Michelle from the Sibener Lab and Dan)—has been my favorite part of Chicago living. From our kayaking adventures, eclipse chasing in Carbondale, bike rides to Chinatown, birthday celebrations, to hikes around the Midwest, you guys have reminded me there's more to graduate school than just being a one-track racehorse in the lab. For all my frequent failures in my experiments, my lab mates have shown me an equal measure of kindness and encouragement. To my unofficial mentor, without whom I really could

not have survived grad school: Yu, the most talented post-doctoral researcher I've met and a most inspiring friend, who always had an uncanny way of making people feel that they belonged and were going to be ok at the end of the day. Thank you, and may you continue to make academia a kinder and more welcoming place for everyone. To Jack, an incredibly gifted undergrad researcher I've had the chance to work with in my final year of grad school. Another heartfelt thank you goes to the rest of my lab mates who will succeed me: Andrew, Ce, Jingyuan, Yuanke, Hanyu, Tomojit, Jae Hyung, Jong-hoon, Mengyu; the members who came before me: Joonki, Myungjae, Jae-Ung, Hui, Kan-Heng, Preeti, Andy, Chibeom, Kibum, Saien, Lulu. At times, grad school felt endless, but looking back now makes it seem but a mere flash. May we never stop finding reasons to cross paths again.

Outside the lab, my friends and family have shown remarkable forbearance with me in my bleakest of days. MRSEC lab manager Justin Jureller, thank you for your infinite wisdom and for letting me hog a popular shared equipment. Ram and Ananth, who've brought me out of my isolation among my tiny group and led me to adore what this dilettante swimmer opines is Chicago's best attraction: Lake Michigan itself. My sacrifices pale in comparison to those of my family halfway across the world. Dad, for cheering me on and always reminding me to take things easy. My high-flying attorney of a twin sister who has made it in the real world long before me. And Mom, I miss you every day, and I don't know how you wrangled a PhD yourself back in the sunshine of your days—or perhaps, now I finally do.

And my long-distance partner, Mike—I really couldn't have come quite this far without you. Your care and support have been priceless, even from opposite ends of the country. You've been my lodestar in the night, my alpine vista at the end of a grueling backpacking journey.

ABSTRACT

Two-dimensional van der Waals (vdW) materials are layered crystalline solids characterized by their bonding anisotropy, in which the atoms within each monolayer are connected by strong covalent bonds, while the layers are bound by significantly weaker and directionless van der Waals forces in the through-plane direction. The latter feature allows the atomically thin monolayers of these 2D materials to be isolated and recombined without lattice matching, without commensurability, and with any member of the 2D vdW materials family. This allows us to generate a virtually limitless library of designer solids from these monolayers assembled in any arbitrary sequence and orientation. The customizability of the vertical composition and structure of the overall solid at the atomic limit translates to novel vibrational properties, thereby opening up new opportunities for exploring thermal transport phenomena at the nanoscale.

My dissertation will focus on engineering novel thermal transport properties in artificial solids assembled from large-area, polycrystalline 2D vdW materials. Firstly, I will discuss the effect of interlayer rotation on the thermal anisotropy of stacked film assembled from transition metal dichalcogenide (such as MoS_2) monolayers. Our film has a unique rotationally scrambled structure—large crystalline domains in plane, but complete crystalline mismatch in the through-plane direction between atoms from adjacent monolayers—that imbues our material with record-breaking thermal conductivity anisotropy. We reveal new insights on the thermal transport mechanisms in our films and explain them using collaborative-effort atomistic simulations. In this dissertation, I will also characterize the contribution of air-solid interfacial thermal transport in the measurement of the apparent thermal conductance of suspended vdW monolayers. My dissertation will propose several new directions, enabled by this research, for further engineering of thermal transport in 2D vdW crystals. This work paves the way for creating novel materials

solutions for improved thermal management in nanoelectronics and provides a new playground for studying exotic thermal physics at the nanoscale.

CHAPTER 1: INTRODUCTION AND OVERVIEW

1.1 Motivation

Thermal conductivity κ is an important parameter that dictates the functions and performances of various materials in our daily lives. In the past, it was often thought of as an auxiliary property of a material compared to its other electrical and optical characteristics[1]. However, as electronics trend towards miniaturization, their constituent material's thermal properties have become one of the gatekeepers of sustaining this trend. In the semiconductor industry, a high κ is required to promote heat dissipation from the heat sources. Indeed, one of the roadblocks to Moore's Law's predictions is thermal management in shrinking electronics[2], and the finer structures and increased interfaces may lower κ compared to the bulk values. Furthermore, despite the shrinking of electronics, the power consumption per chip has stayed roughly the same[3], so more heat now has to be dissipated in a smaller volume. Inefficiency in this dissipation may lead to overheating, which may reduce device performance and give rise to dangerous hotspots.

On the other extreme, low κ materials are also important for another technology: thermoelectrics. Such materials need to sustain a large temperature gradient to drive the flow of charge carriers and vice versa. But the low κ needed along with high electrical conductivity create a design conflict in thermoelectric materials, as these two properties are often strongly correlated. Nevertheless, there is some room among semiconductor materials for tuning thermal and electrical conductivities independently; with some separation of mean free paths between their heat and electron carriers that allow for the engineering of one transport property partially independently of the other[4]. Nanostructuring is a common strategy to reduce κ in these materials by generating nanoscale internal structures and improve thermoelectric efficiency[5]. Hence, an

understanding of thermal conduction at the nanoscale is crucial for advancing this technology for the future.

Before we discuss thermal transport in previously reported nanomaterial systems, we will first review the basics of thermal conductivity in crystalline solids. This chapter and the rest of the dissertation will only focus on nonmetallic solids, in which the major heat carriers are phonons.

1.2 Fourier's law of heat conduction

Thermal conductivity is defined by Fourier's law: $\boldsymbol{J} = -\kappa\, \boldsymbol{\nabla} T$, where $\boldsymbol{J}$ describes the heat flux vector and $\boldsymbol{\nabla} T$ is the temperature gradient. κ here is assumed to be a material property and independent of the size. However, this assumption is only true when the size of the material structure is much longer than the heat carrier mean free path, which is the average distance traversed by heat carriers between successive collisions. For nanomaterials and nanostructured materials, this assumption is often violated, and size effects may emerge.

In crystalline semiconductors and dielectric materials, heat is primarily carried by wave-like atomic vibrations called phonons. These "packets" of quantized vibrational energy in the crystal lattice are described as quasiparticles propagating diffusively in accordance with the phonon gas model. These phonons have a wide spectrum of mean free paths and frequencies, so no single length scale captures the entire conduction behavior.

Thermal conduction in nanoscale systems can deviate from Fourier's law when the predicted thermal conductivity diverges from experimentally measured values. Oftentimes, Fourier's law overpredicts the heat transfer rate at the nanoscale[6,7]. This is because a significant proportion of phonons may travel ballistically—whereas Fourier's law assumes all phonons are diffusive—and hence do not contribute to temperature equilibration. Fourier's theory assumes that a local

temperature equilibrium is achieved, but this may not be the case when there is a temperature mismatch between ballistic and diffusive phonons.

A simple way to observe this overprediction is to compare diffusive thermal transport as described by Fourier's law and the radiative limit in which no meaningful length scale can be defined[8]. When the material length scale shrinks below the phonon mean free path, phonon-phonon scattering can be neglected and gradually resembles transport across the interface, allowing us to describe transport as a radiative process. Describing absolute heat transfer rate between two concentric, spherical shells at different temperatures and radii T_h at radius r, and T_c and $r + \Delta r$, respectively, we have

Fourier: $Q \sim r^2\ C\ v\ l\ (T_h - T_c)/\Delta r$,

Radiative: $Q \sim r^2\ C\ v\ (T_h - T_c)$, where the factor of r^2 comes from the surface area of a sphere,

Hence,

$$\frac{Q_{Fourier}}{Q_{Radiative}} \sim \frac{l}{\Delta r}$$

At the regime of $l \gg \Delta r$, $Q_{Fourier} > Q_{Radiative}$, Fourier tends to overpredict the heat transfer rate.

Thermal measurements at the nanoscale also show how Fourier's theory can overestimate the thermal conductivity. Examples include (i) κ of nanomaterials showing size dependence[9–12], and (ii) the observation of the ballistic/diffusive dissipation of heat from nanoscale heat sources[13–15], such that the measured κ depends on heater line dimensions.

1.3 Heat conduction by dispersive phonons

The thermal conductivity in a 3D solid is often described as $\kappa = {}^{1}/_{3}\, C_v\, v_g\, l$, whereby C_v is the volumetric heat capacity, v_g is the average phonon group velocity, and l is the average mean free path of the phonons.

However, the direct calculation or prediction of the κ is challenging, because all the parameters in the right side of the equation is spectrally dependent, so a more accurate theoretical description of κ would be

$$\kappa = \frac{1}{3} \int_0^{\omega_D} C_v(\omega)\, v_g(\omega)\, l(w)\, d\omega = \frac{1}{3} \int_0^{\omega_D} C_v(\omega)\, v_g^2(\omega)\, \tau d\omega,$$

where ω_D is the Debye frequency, or the frequency of the highest order vibrational mode, at which all atoms vibrate out of phase with respect to each of their neighbors.

The phonon band structure tracks the relationship between the frequency of all phonons and their wavevectors. Which phonons are excited depends on the energy of the state and the temperature, as dictated by the Planck distribution. The temperature-dependent population of phonon modes is reflected in $C_v(\omega)$, where

$$C_v = \frac{d}{dT}(3 \int_0^{\omega_D} d\omega\ D(\omega) < n > \hbar\, \omega),$$

where $D(\omega)$ is the phonon density of states, and the energy of each phonon mode is $\hbar\, \omega$. $< n >$ is the population of phonons as dictated by the Planck distribution $\frac{1}{e^{\hbar\, \omega / k_B T} - 1}$. $D(\omega)$ dictates the distribution of the energy levels of all the available phonon modes in q-space, whereas the Planck distribution determines how these levels are populated, given the temperature of the surroundings.

The spectral dependence of v_g can be traced to the phonon dispersion of the solid, which in turn depends on the crystal structure. The number of the atoms per unit cell translates to the number

of phonon branches in the dispersion. The branches can be grouped into the acoustic branches, representing the lower energy vibrational modes whereby neighboring atoms vibrate in phase; and the higher energy optical branches, in which atoms vibrate out of phase with the neighbors. v_g depends on the slope of the dispersion curve. Acoustic phonon branches are usually more dispersive and have steeper slopes than the optical branches. The slope $\frac{d\omega}{dq}$ of the branch denotes the v_g for every wavevector q in that branch. Acoustic phonons are the main heat carriers of a solid, since they typically have higher v_g compared to the flatter-branch optical phonons. Furthermore, phonons near the edge of the Brillouin zone also have lower group velocity.

The description of heat transport is still incomplete without factoring in the timescale for which these vibrations persist. This, in other words, is the reciprocal of the scattering rate as dictated by phonon-phonon coupling and the interactions with sample defects. While lower v_g optical phonons and higher ω phonons themselves do not usually carry much heat, they are still able to significantly influence κ by interacting with the dominant phonons and shortening the phonon mean free path l.

Scattering limits transport processes. Phonon-phonon scattering is the most basic scattering mechanism and gives rise to anharmonicity in the lattice. The first kind is normal scattering, where the total crystal momentum is conserved after the collision; i.e., $\boldsymbol{q}_1 + \boldsymbol{q}_2 + \boldsymbol{q}_3 = 0$, where $\boldsymbol{q}$ is the phonon wavevector. At low temperatures, normal scattering alone does not contribute to thermal resistance[16] because this scattering mechanism conserves crystal momentum in the original direction of phonon propagation. But even in a perfect crystal with no defects, l cannot be infinite, due to Umklapp scattering. As two phonons collide, their wavevectors combine into a third wavevector that falls outside the first Brillouin Zone; due to the periodicity of the lattice, the larger wavevector may be mathematically transformed back into

the first Brillouin Zone as a phonon with a momentum pointing in the opposite direction. As such, the resulting superposition phonon travels "backward" and the conservation of momentum becomes $\boldsymbol{q}_1 + \boldsymbol{q}_2 + \boldsymbol{q}_3 = \boldsymbol{G}$, where $\boldsymbol{G}$ is the nonzero reciprocal lattice vector.

Umklapp scattering is especially prominent for higher frequency phonons and at temperatures above the Debye temperature. As the temperature increases, the population of phonons increases, and the increase in collision frequency lowers the thermal conductivity at a rate linearly proportional to the temperature. This is the diffusive limit of phonon transport in ideal crystals[17]. Both the acoustic and optical branches can interact via these scattering processes to impede heat flow, depending on the size of the band gap that separates these two branches. The larger the mass difference between the atoms in the unit cell, the larger the size of the band gap. This may reduce the phonon scattering space if the resulting phonon lies in the band gap region where no phonon should exist. An example of this phenomenon is the high κ value of 1200 W m^{-1} K^{-1} measured in cubic boron arsenide, whereby the large mass difference between the B and the As atoms leads to a large band gap that screens 3-phonon interactions, only permitting higher order interactions such as 4-phonon scattering (Fig. 1.1).

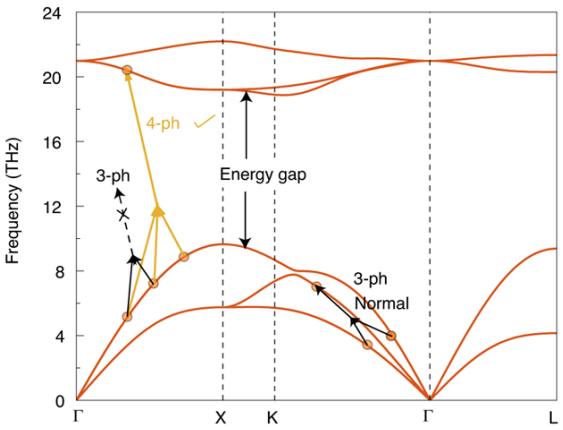

Figure 1.1 Phonon-phonon scattering selection rules as dictated by the phonon dispersion of a material, using cubic BAs as an example. The large energy gap in the phonon dispersion, thanks to the large mass difference between the B atom and the As atom, prevents the lowest order and most common form of Umklapp scattering, 3-phonon scattering. Reproduced from reference [18].

Real-life crystals contain scattering sites that are the defects, interfaces, impurities, and boundaries. Their effects on thermal conductivity values usually manifest at lower temperatures, when the low phonon population probes the intrinsic limiting factors to thermal transport of a material instead of phonon-phonon scattering. Moreover, phonons can also scatter off other heat carriers such as electrons and holes[19]. The combined effects of different sources of scattering is illustrated by Matthiessen's rule, whereby the scattering rate $1/\tau = 1/\tau_{Umklapp} + 1/\tau_{impurities,defects} + 1/\tau_{boundary} + 1/\tau_{phonon-electron}$, and τ is the phonon relaxation time. The equation resembles the total resistance among the individual resistors connected in series. Phonons scatter differently depending on whether their characteristic length scales match the system size. In literature, the definition of these characteristic length scales are vague, and they are often used interchangeably. We will define them in the section below and discuss them in the context of scattering off interfaces, then outline their limitations.

1.4 Characteristic lengths of phonons

Like other quantum particles, phonons show wave-particle duality. Three important length scales define phonons: the mean free path, the phonon coherence length, and the wavelength. The first quantity is more aligned with the particle picture of phonons and hence agrees with the diffusive assumption of Fourier's law, whereas the second and third are more relevant for the discussion of phonons as waves. Phonon coherence length can be thought of as the spread of the wave packet from a superposition of different-wavelength phonons. These length scales are not equivalent to each other. The discussion of wave scattering should include whether the phase behavior of incident phonons is retained or not[20]. Scattering that reduces thermal conductivity often discusses mean free paths. However, coherence lengths and particle mean free paths are of similar order of

magnitude (equivalent at high temperature; the former is longer than the latter at low temperature and boundary scattering is dominant[8]), so in our discussion of thermal conductivity, we can treat them as qualitatively synonymous.

High frequency and hence shorter wavelength phonons have shorter mean free paths[21], and the mapping of wavelength to mean free path is even less well-defined. Literature has often loosely linked these three different length scales to each other. At most, one can define an average phonon wavelength λ from the average energy of a phonon at ambient temperature $< E > \approx < n > \hbar\omega = k_B T$, assuming $< n >$ = 1. If we use the Debye's approximation of a linear phonon dispersion such that $\omega = \frac{2\pi v}{\lambda}$ and v is the phonon speed, then

$$\lambda = \frac{2\pi\hbar v}{k_B T}$$

Nevertheless, size effects in nanomaterials emerge when the system size matches any of these characteristic lengths. Besides diffusive behavior, phonons have also exhibited a wide variety of fluid (hydrodynamic)[22,23] and wave-like (interference, diffraction)[24–26] behavior in nanomaterials depending on the length scales and concentration of phonons, though these phenomena fall outside the scope of this dissertation.

1.5 Interfacial thermal transport

Nanostructures typically contain a high density of interfaces, so thermal transport will be dominated by their properties. Since interfaces have no associated dimension, their transport behavior is described by a modified Fourier's law $\boldsymbol{J} = -G\,\Delta T$, whereby G is the pairwise unique interfacial thermal conductance among two materials that straddle the interface. Interfaces between crystals generate thermal resistance, because phonons may be reflected instead of transmitted across the interface. The acoustic mismatch model (AMM) describes

phonons more like waves, in which their probability of transmission across an interface depends on the difference in the acoustic impedance between two materials in contact. The model is the Snell's Law equivalent for describing the transmission of phonon waves, which are either refracted or reflected specularly at the interface. No scattering occurs. For this reason, AMM typically underpredicts G because it assumes a perfect interface.

For higher temperatures at which phonon-phonon scattering is more prevalent, the diffuse mismatch model (DMM) is a more realistic depiction of conduction across the interface. Here, all phonon scattering across the interface is assumed to be diffusive, which is indeed the case for imperfect interfaces. The probability for phonon transmission depends on only the density of vibrational states in the two materials across the interface. Nevertheless, the DMM is also not always accurate in predicting G.[27,28] To overcome the limitations of both the AMM and DMM, new models have been proposed, which factor in inelastic scattering, phonon scattering with electrons, weighted averaging of the phonon velocities on both sides of the interface, and anharmonicity[29].

One question is whether to treat phonons as waves or as particles, or in other words, whether to apply the AMM or DMM when describing interfacial thermal conduction. The first necessary criterion for wave effects is to for the mean free path/phase coherence length to exceed the material characteristic length, with fewer boundary scattering events that might possibly destroy the phase coherence. Moreover, at interfaces, the length scale of roughness should be much smaller than the wavelength of phonons for these wave effects to be apparent. At room temperature, the average wavelength of phonons in Si ranges from 1-10 Å, based on estimations with the Debye Approximation and equation in the previous section. Given this wavelength is of

the order of atomic length scales, phase-preserving phonon transport across the interfaces is quite rare, and classical size effects usually dominate.

1.6 Thermal transport in 2D vdW films

The rise of nanomaterials for real-world technological applications has spurred interest in thermal transport phenomena at the nanoscale. Thin films in particular have captured much of the attention—their planar geometries in theory allow for them to be integrated with other materials at a large and industrially relevant scale when applied as coatings, thanks to their "1D micro/nano/atomic, 2D macro" architecture.

Among these thin film materials, 2D van der Waals (vdW) layered materials have attracted much interest for their superior thermal stability, tunable electrical and optical properties, broadband absorption, excellent mechanical properties etc. These materials are characterized by their bonding anisotropy, and in particular, their weak and directionless vdW surfaces that allow for the monolayers to be isolated from the crystal and restacked with other monolayers. The weak and directionless vdW interactions between the monolayers allow them to be arbitrarily combined without the constraints of other conventional thin film growth techniques, such as lattice matching, so they can be assembled with other monolayers of different chemical species to create previously inaccessible heterostructures. Combined layer by layer, these materials allow for the tailoring of the vertical structure of the resulting heterostructure at the atomic limit, which will translate to novel vibrational properties for thermal transport.

These properties make 2D vdW materials an interesting material platform for investigating novel thermal transport phenomena at the nanoscale. The wide library of 2D vdW heterostructures that can be accessed via this mix-and-matching opens up a rich playground to explore a diversity of thermal properties in these artificial solids. Moreover, the large surface area of 2D materials

relative to the material volume allows for the incorporation of interfacial properties in the design of the overall solid. When used as building blocks with which to assemble solids, 2D vdW monolayers can enable the customization of with customized overall thermal transport properties, starting from the atomic limit.

1.7 Dissertation overview

The goal of this dissertation is to probe the thermal transport behavior of 2D vdW materials, in particular, how does the polycrystallinity of large-area films influence thermal transport, and can we make use of this property to engineer novel thermal transport phenomena in assembled 2D vdW solids? How do our thin-film materials compare to exfoliated 2D vdW films, and is it possible to preserve the excellent properties associated with single crystallinity where desired? The next chapter provides an overview of the general strategies for engineering thermal conductivity in crystalline solids to lay the groundwork for describing how to engineer the thermal properties of 2D vdW layered crystals. We supplement the discussion with a review of the most common thermal measurement techniques suited for thin film materials. In Chapter 3, we detail our method for designing an artificial solid with directionally dependent disorder, which is based on the concept of interlayer rotation. This led to our observation of record-breaking thermal conductivity anisotropy in our assembled vdW layered thin film, beating that of nature's most anisotropic solid: graphite. We then present our investigations into the origins of this extreme thermal transport behavior via molecular dynamics simulations in Chapter 4, followed by a demonstration of our material's practical application as heat spreaders for nanoelectronics. Chapter 5 discusses the effect of air-solid interfacial thermal conduction on the measurement of the in-plane thermal conductivity of suspended 2D vdW films, and the factors that may influence this air-assisted thermal transport across the film surface. Previous thermal

measurements on suspended vdW films by other research groups have often neglected this effect of air-solid interfacial thermal conduction, which can significantly influence the measured in-plane thermal conductivity value of suspended thin films. Finally, the dissertation will conclude with a discussion on potential research directions for the future.

1.8 References

1. Goodson, K. E. Ordering up the minimum thermal conductivity of solids. *Science* vol. 315 342–343 (2007).

2. Moore, A. L. & Shi, L. Emerging challenges and materials for thermal management of electronics. *Materials Today* **17**, 163–174 (2014).

3. Tekla, S. P. Forget Moore's Law—Chipmakers Are More Worried About Heat and Power Issues. *IEEE Spectrum* (2019).

4. Singh, D. J. & Terasaki, I. Thermoelectrics: Nanostructuring and more. *Nature Materials* vol. 7 616–617 (2008).

5. Kim, W., Wang, R. & Majumdar, A. Nanostructuring expands thermal limits. *Nano Today* vol. 2 40–47 (2007).

6. Chen, G. Nonlocal and Nonequilibrium Heat Conduction in the Vicinity of Nanoparticles. *Journal of Heat Transfer* **118**, 539–545 (1996).

7. Mahan, G. D. & Claro, F. Nonlocal theory of thermal conductivity. *Physical Review B* **38**, 1963 (1988).

8. Yang, R. Nanoscale Heat Conduction with Applications in Nanoelectronics and Thermoelectrics. (2005).

9. Lee, J., Lim, J. & Yang, P. Ballistic Phonon Transport in Holey Silicon. *Nano Lett* **15**, 27 (2015).

10. Sood, A. *et al.* Quasi-Ballistic Thermal Transport Across MoS2 Thin Films. *Nano Letters* **19**, 2434–2442 (2019).

11. Bae, M. H. *et al.* Ballistic to diffusive crossover of heat flow in graphene ribbons. *Nature Communications* **4**, (2013).

12. Chen, L., Braun, J. L., Donovan, B. F., Hopkins, P. E. & Poon, S. J. Ballistic transport of long wavelength phonons and thermal conductivity accumulation in nanograined silicon-germanium alloys. *Applied Physics Letters* **111**, (2017).

13. Siemens, M. E. *et al.* Quasi-ballistic thermal transport from nanoscale interfaces observed using ultrafast coherent soft X-ray beams. *Nature Materials* **9**, 26–30 (2010).

14. Minnich, A. J. *et al.* Thermal conductivity spectroscopy technique to measure phonon mean free paths. *Physical Review Letters* **107**, 095901 (2011).

15. Johnson, J. A. *et al.* Direct measurement of room-temperature nondiffusive thermal transport over micron distances in a silicon membrane. *Physical Review Letters* **110**, 025901 (2013).

16. Maznev, A. A. & Wright, O. B. Demystifying umklapp vs normal scattering in lattice thermal conductivity. *American Journal of Physics* **82**, 1062–1066 (2014).

17. McConnell, A. D. & Goodson, K. E. *Thermal Conduction in Silicon Micro- and Nanostructures*. *Annual Review of Heat Transfer* vol. 14 (2013).

18. Qian, X., Zhou, J. & Chen, G. Phonon-engineered extreme thermal conductivity materials. *Nature Materials* **20**, 1188–1202 (2021).

19. Quan, Y., Yue, S. & Liao, B. Impact of Electron-Phonon Interaction on Thermal Transport: A Review. *Nanoscale and Microscale Thermophysical Engineering* **25**, 73–90 (2021).

20. Macklin, C. Using morphology and structure to tune solid-state thermal properties. *DNA Mediated Assembly of Protein Heterodimers on Membrane Surfaces* 67 (2020).

21. Hori, T. & Shiomi, J. Tuning phonon transport spectrum for better thermoelectric materials. *Science and Technology of Advanced Materials* **20**, 10 (2019).

22. Cepellotti, A. *et al.* Phonon hydrodynamics in two-dimensional materials. *Nature Communications* **6**, 1–7 (2015).

23. Lee, S., Broido, D., Esfarjani, K. & Chen, G. ARTICLE Hydrodynamic phonon transport in suspended graphene. *Nature Communications* **6**, (2015).

24. Maldovan, M. Phonon wave interference and thermal bandgap materials. *Nature Materials* **14**, 667–674 (2015).

25. Maire, J. *et al.* Heat conduction tuning by wave nature of phonons. *Science Advances* **3**, e1700027 (2017).

26. Hanus, R., Garg, A. & Snyder, G. J. Phonon diffraction and dimensionality crossover in phonon-interface scattering. *Communications Physics* **1**, 1–11 (2018).

27. Duda, J. C., Beechem, T. E., Smoyer, J. L., Norris, P. M. & Hopkins, P. E. Role of dispersion on phononic thermal boundary conductance. *Journal of Applied Physics* **108**, 073515 (2010).

28. Stevens, R. J., Smith, A. N. & Norris, P. M. Measurement of thermal boundary conductance of a series of metal-dielectric interfaces by the transient thermoreflectance technique. *Journal of Heat Transfer* **127**, 315–322 (2005).

29. Zhang, P. *et al.* A Theoretical Review on Interfacial Thermal Transport at the Nanoscale. *Small* vol. 14 1702769 (2018).

CHAPTER 2: STRATEGIES TO TUNE AND MEASURE THERMAL TRANSPORT IN CRYSTALLINE THIN FILMS

2.1 Introduction

The values of thermal conductivity κ span nearly five orders of magnitude (Fig. 2.1). Among the most common natural dielectric materials, κ values can be low as 1 W m^{-1} K^{-1}, such as in disordered ceramics[1], or go up to ~ 2000 W m^{-1} K^{-1} in crystalline diamond. Engineering strategies have increased the range of these values. For example, incorporating porosity can lower κ to below 0.1 W m^{-1} K^{-1}. In an extreme case demonstrated by Xu and Duan et al[2], κ was lowered to the order of 0.001 W m^{-1} K^{-1}. On the other end of the extreme, isotopic enrichment has boosted κ in diamond to over 3000 W m^{-1} K^{-1}.[3]

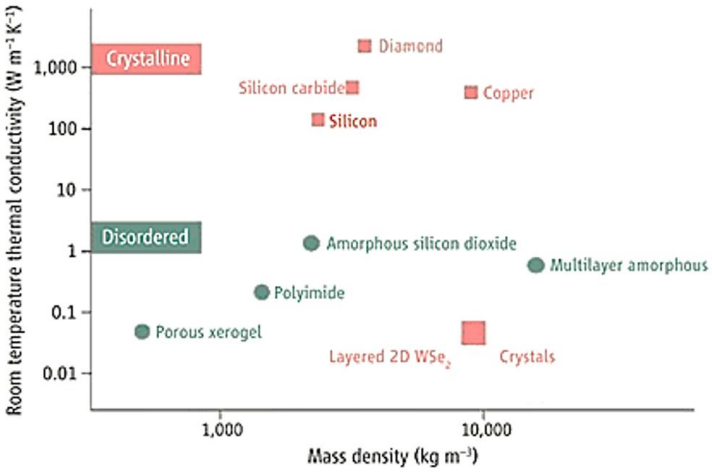

Figure 2.1. Thermal conductivity values of solids span a range of about 40,000 W m^{-1} K^{-1}. Reproduced from reference [4].

The thermal conductivity of thin film materials may diverge from the bulk. Frequently, κ can be lower in a thin film geometry due to boundary scattering, impurities scattering, surface sensitivity etc. This is not always the case, with notable exceptions to be monolayers of 2D vdW

materials[22, 49], whereby the value of κ along the in-plane direction remains constant or even improves at a lower monolayer count. Moreover, thin film materials may also exhibit anisotropy, as their dimensionality may affect their properties along one direction differently from along another.

Using concepts from the previous chapter, this chapter will survey experiments on designing the thermal properties in thin film solids and their interfaces. We will discuss thermal anisotropy and heat conduction in low-dimensional materials, then evaluate various attempts to boost the anisotropy in these materials.

2.2 General strategies for engineering κ

2.2.1 Phonon band engineering

Tailoring the phonon band structure can alter the value of κ via several ways: changing the scattering phase space between phonons, altering v_g, opening up band gaps in the dispersion, zone folding etc. The description and hence the manipulation of a crystal's phonon dispersion starts from the unit cell. The deposition of crystals with large and complex unit cells (Fig. 2.2A) provides many degrees of freedom for tuning the dispersion.

Large unit cells, for example, can result in an optical phonon branch that has low lying branches that hug close to the acoustic branch, leading to optical-acoustic coupling. As these primitive cells become larger, the Brillouin zone shrinks, and this may reduce the size of the acoustic band and the proportion of higher-velocity acoustic phonons participating in heat transport[5]. Heavier-element atoms incorporated in the unit cell and interwoven throughout the crystal structure may lead to sluggish vibrations and weaker chemical bonds, hence can tune the lattice thermal

conductivity by suppressing v_g.[5] Alloying may also remove electrons from bonding states and weaken interactions between atoms, thereby softening the lattice by reducing the sound velocity in a material[6]. Phonon band engineering with complex unit cells containing heavy atoms that have low electronegativity is a good way to reduce κ to amorphous material levels while retaining high electrical conductivity as if the solid is a single crystal. This has given rise to a "phonon glass-electron crystal" paradigm, which is especially crucial for generating high performance thermoelectric materials[7,8].

While synthesis techniques might not be able to produce a new crystal with just about any desired unit cell from scratch, combining different crystals into superlattices with nanoscale periodicity can alter the overall dispersion of the artificial solid. For instance, the fabrication of superlattices is known to lead to ultralow κ values, due to a phenomenon called zone folding in the band structure (Fig. 2.4D). Combining different materials in an alternating fashion at the nanoscale generates a second larger enveloping repeating unit on top of the periodicity of the constituent crystals, leading to zone folding in momentum space. This in turn superimposes a smaller overall Brillouin Zone[9]. Moreover, band gaps open up at the band edge, and this also reduces the average v_g of phonons. Computer simulations have shown that superlattices can beat the amorphous limit of their constituent materials, whereby all coherent lattice vibrations that are scattered to within half to one wavelength[13], as long as there are a large mass mismatch and weak interactions across the interfaces[10].

2.2.2 Mean free path engineering

The most straightforward means to engineer κ of a material is by disrupting the phonon mean free path, l, via nanostructuring, which is the creation of nanoscale internal structures such as

nanograins in a solid[11]. Figures 2.2B, C demonstrate how nanostructuring can tune κ of bulk Si, by modifying its crystallinity. In general, the crystallinity of a solid scales with the coherent length of the phonons; so materials with smaller crystalline domains and hence higher disorder have lower κ compared to its crystalline counterparts. Additional methods to reduce the phonon mean free path include the incorporation of scattering centers such as defects and interfaces throughout the material. Depending on the length scale and spatial frequency of these scattering sites, phonons can be spectrally screened according to their corresponding mean free paths.

An effective way to drastically lower the overall κ in a material involves incorporating defects that cover the entire or most of the spectrum of these length scales (Fig. 2.2D). Using a panoptic and hierarchical engineering approach, Biswas and Kanatzidis *et al.* employed atomic-scale alloy doping, nanoparticles, and mesoscale grain boundaries to achieve maximum phonon scattering in the thermoelectric material PbTe[12]. As a result, the researchers attained a low $\kappa \sim 0.9–3$ W m^{-1} K^{-1} and a then record-high zT thermoelectric figure of merit that indicates a material's efficiency for heat-electricity conversion of ~ 2.2 at 915 K. To achieve high thermoelectric efficiency, a low κ is crucial for maintaining the separation of the hot and cold ends of a material, and this temperature gradient drives the flow of charge carriers in a material.

The complete randomization of the atomic structure leads to the amorphous limit, a theoretical lower bound of the thermal conductivity[13]. Here, phonons are scattered within a wavelength or less. Arguably, the phonon gas model no longer applies in the discussion of thermal transport, since the atomic vibrations are no longer coherent that the very concept of a phonon is not obeyed in this context.

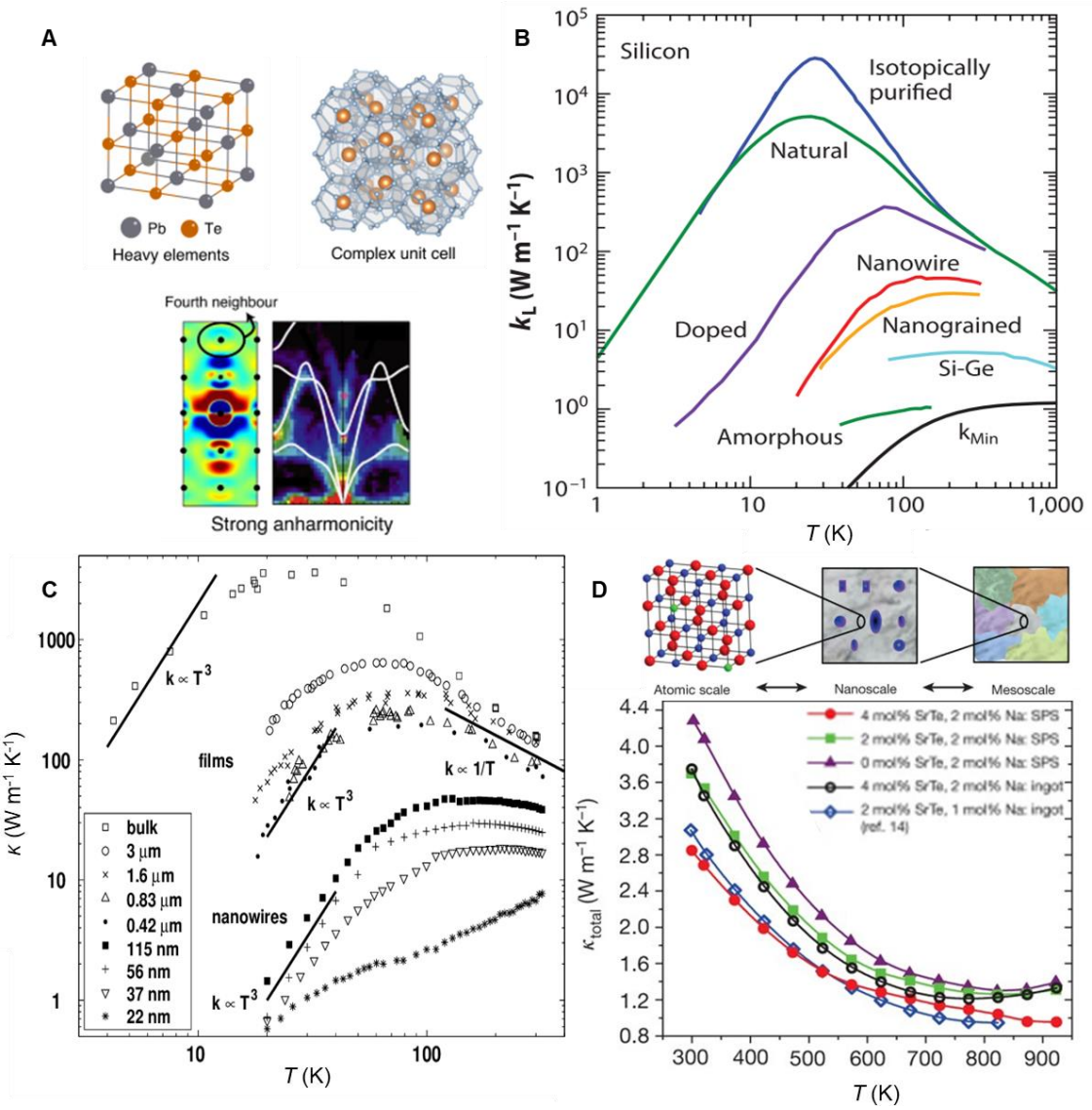

Figure 2.2 Strategies to tune thermal conductivity in bulk crystals. (A) Strategies to reduce thermal conductivity by tailoring the unit cell include incorporating heavy atoms, building in anharmonicity into the band structure and bonding, and engineer complex, cage-like unit cells with rattling vibrations. Reproduced from reference [14]. (B) Nanostructuring techniques and their impact on the thermal conductivity of silicon. Reproduced from reference [15]. (C) Experimentally measured temperature-dependent thermal conductivity values of single-crystal, bulk Si can be tuned by several orders of magnitude depending on the thickness of the film or diameter of the nanowire the semiconducting material is fashioned into. Reproduced from reference [16]. (D) A hierarchical material architecture with different scattering lengths at the atomic, nanoscale, and mesoscale levels can subdue phonon propagation across a spectrum of mean free paths, resulting in a low thermal conductivity for the thermoelectric PbTe. Reproduced from reference [12].

Engineering the crystal structure of solids can also control the phonon scattering rates. Solids such as skutterudites and clathrates have caged unit cells, in which a weakly bonded guest atom can be introduced. These atoms have the propensity to rattle and scatter with other phonons in the crystal. This added phonon coupling can give rise to highly localized vibrations[17].

Creating interfaces by mixing and matching different materials into a heterostructure or a superlattice is another common method to tune thermal conduction. On top of the reduced size of the band structure, the individual interfaces in a superlattice can also scatter heat carriers.

Superlattices employ a high density of interfaces to engineer κ; we will discuss briefly in the following section engineering interfacial thermal transport from a single interface perspective.

2.2.3 Tuning thermal transport across the interface

The value of the interfacial thermal conductance, G (Fig. 2.3A) is sensitive to the environment. Sample preparation protocols may result in roughness, disorder, contamination, or weakened bonding that will dominate the thermal properties of the interface[18].

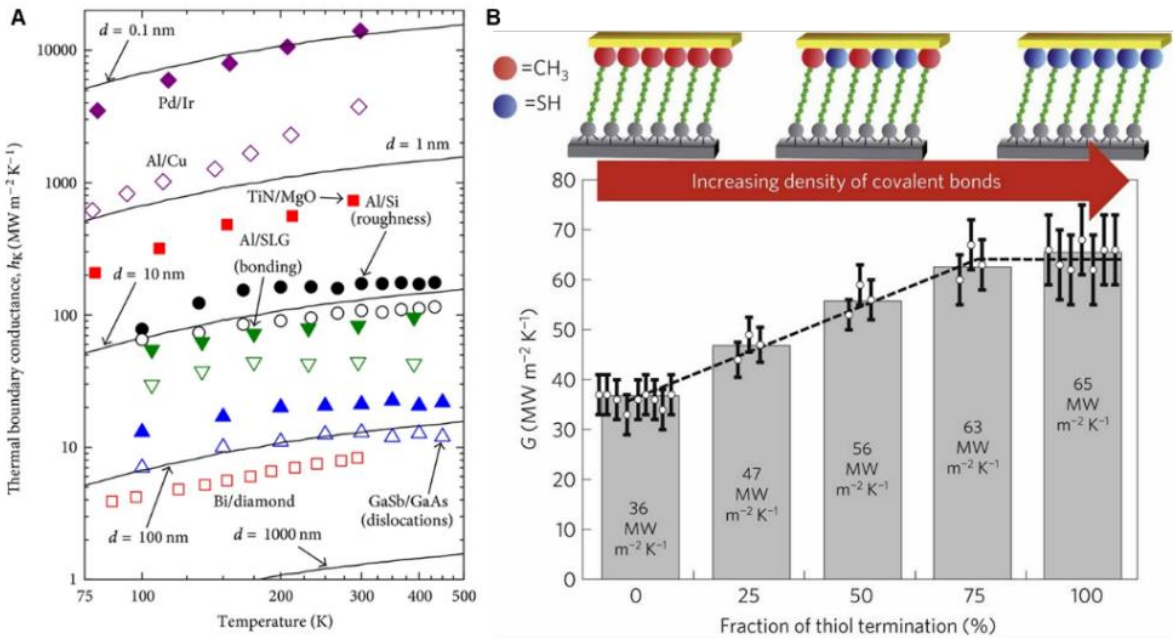

Figure 2.3 Interfacial thermal transport; a materials survey and a modification strategy. (A) A sample of the variety of interfacial thermal conductance values between different solid pairs. *d* refers to the thickness equivalent of SiO_2, shown as solid lines. Reproduced from reference [18]. (B) Increasing the chemical affinity between interfaces, such as functionalizing aurophilic long-chain hydrocarbons promotes thermal transport across a gold-self assembled monolayer interface. Reproduced from reference [19].

While interfaces typically disrupt thermal transport, its phonon transmissibility can be tuned for improving G. Previous research has reinforced the interfacial bonding or physical adhesion between two surfaces using self-assembled monolayers of hydrocarbons[19] or chemical functionalization[20] (Fig. 2.3B). MD simulations by Wang *et al.* demonstrated that controlling the crystal phases at the interface may lower the thermal resistance of epitaxial AlN/GaN interfaces[21].

Interfaces play an important role in thermal engineering as a means for nanostructuring a solid. Introducing a high density of interfaces may alter the overall properties of a material in ways not accessible to a bulk crystal. When nanomaterials are used as building blocks for assembling

artificial solids, the interfaces may dominate the property over the intrinsic features of the constituent material itself.

2.3 The impact of low dimensionality on thermal transport

Heat transport in lower dimensional materials may diverge from their 3D counterparts. Like the electronic band structure, the phonon dispersion is also affected by dimensionality reduction. Lower dimensions may alter the phonon density of states, dispersion, and selection rules for scattering processes, all of which may impact the thermal conductivity of a material. As a result, new thermal transport phenomena may emerge that are not observable in 3D systems. This section will discuss some of these phenomena as well as the impact of lower dimensionality on κ.

Theoretical studies have observed that the intrinsic κ, typically independent of system size in 3D, scales with number of atoms or linear dimension in 1D or 2D crystals[22]. Low dimensionality can be rationalized towards two potential thermal outcomes: higher κ in the direction parallel to the interface, or lower κ—not just in the direction normal to the interface.

In the first scenario, a higher κ parallel to the surface may arise from a smaller phonon phase space, which reduces the scattering between the phonons in this direction. In this case, the low dimensionality causes the material to act as a phonon wave guide. In a more extreme theoretical case, the non-interaction of phonons in reduced dimensionality nonlinear crystal lattices may lead to a phenomenon as defined by the Fermi-Ulam-Pasta-Tsingou model. With the vibrational modes confined in space, phonon modes don't scatter with each other and thus do not thermalize. Hence, the propagation of these modes through the crystal is ballistic, leading to a theoretically infinite thermal conductivity for these modes.

A well-known example of how low dimensionality may boost κ is how the in-plane κ in graphite is lower than that in graphene, a true 2D array of atoms compared to other material candidates[23,24]. It has been observed that the in-plane phonons in graphene have long mean free paths of the order of 800 nm in graphene flakes[22,25]. Ghosh and Balandin *et al.* investigated the dimensional crossover of the in-plane κ in few-layer graphene[22]. Varying the layer number from 1 to 8, the researchers measured higher in-plane κ for exfoliated graphene samples of 1–3 layers in thickness. In particular, the monolayer had a six-fold higher κ compared to the thicker multilayer graphene samples, whose κ saturated at the bulk value at around 1200 W m^{-1} K^{-1}. Another evidence of the increasing in-plane κ of graphene with sample size is work by Xu and Özyilmaz et al[26]. The researchers found that κ scaled with the logarithm of the length of their CVD-grown graphene, even as this sample length exceeded the average phonon mean free path by an order of magnitude. While these examples show how the reduction of dimension can increase κ, the experimental evidence for a diverging κ in agreement with the Fermi-Ulam-Pasta-Tsingou model is less clear and has yet to be proven convincingly[14].

Reducing the size of a material such that the characteristic length scale shrinks to below the mean free path can lead to increased surface scattering and hence a lower κ. The material boundary typically scatters long wavelength phonons, and at small material sizes, boundary scattering may dominate over Umklapp scattering, leading to a lower limit of the thermal conductivity known as the “Casimir limit”. This phenomenon has been observed in bulk Si crystals shaved down to ultrathin films or nanowires[27,28]. Moreover, the κ value of nanostructured crystalline Si has been observed to be lower than fully amorphous Si.

The reduced dimension also alters the phase space and hence the selection rules for phonon scattering. When the sample size is small enough, the scattering off the sample boundaries may dominate over Umklapp scattering, leading to hydrodynamic phonon transport. In this phenomenon, heat is carried in phonon population waves via so-called second sound, analogous to pressure wave propagation in fluids. Second sound is predicted to be observable well above room temperature in a wide range of 2D materials[29], compared to the cryogenic temperatures at which the phenomenon manifests in 3D crystals such as solid He and NaF[30,31].

In reality, both pictures of either increased or decreased κ depend on the system in question and the measurement configuration[23]. The impact of reduced dimensions is often oversimplified by theorical models and challenging to verify experimentally. It also depends on the quality of the interfaces and material boundaries in the prepared sample.

Perhaps the most intuitively, the higher surface-to-volume ratio of materials with reduced dimensionality results in a high sensitivity of thermal transport to the surface properties. Oftentimes, this surface scattering off imperfect interfaces hampers thermal transport and suppresses the value for thermal conductivity. For example, the observation of diverging κ in Si nanowires[32] and membranes has proven challenging, given that the surface is prone to oxidize and hence roughen, thereby scattering phonons. Etching the oxidation layer immediately prior to thermal measurement generates an improvement in the κ value by an order of magnitude[33].

Heat flow in low dimensional materials, in particular thin-film materials, clearly displaying different transport phenomena from 3D crystals, still have many open questions. Given the sensitivity of thermal transport behavior in thin-film materials to the environment and processing conditions, the question is whether the excellent (or “improved”) in-plane properties of these

nanomaterials, 2D crystalline solids in particular, can be retained as the material is extended or assembled into higher dimensions.

2.4 Thermal conductivity anisotropy

2.4.1 Overview

Anisotropic thermal transport occurs when κ in one direction is substantially different from other directions. Low dimensional materials are excellent candidates for generating anisotropic thermal conductors when they are used as building blocks for assembling of 3D artificial solids.

The most well-known anisotropic thermal conductor is graphite, with an anisotropic ratio ρ of over 300[34] when comparing its κ values in the in-plane and out-of-plane directions. Graphite's thermal anisotropy arises from its anisotropic bonding structure, with strong covalent bonds affixing the carbon atoms within the monolayers and comparatively weaker van der Waals forces binding the sheets in the cross-plane direction. Other 2D vdW layered materials such as h-BN, transition metal dichalcogenides, and black phosphorus also have excellent in-plane-to-out-of-plane ρ ratios of ~ 20–100, due to their anisotropic bonding similar to graphene's.

Several theoretical studies have investigated the origins of thermal anisotropy in crystalline solids. Anisotropy in bonding may translate to elastic constants of varying magnitudes along different directions, which in turn scales with the phonon group velocity in each respective direction. These anisotropic crystals with different elastic constants along different orientations have been shown to exhibit phonon focusing. Here, heat flux propagates with a non-spherical wavefront[35], concentrating along certain crystallographic directions. κ may be larger in the

higher-elastic-constant direction, compared to not only the direction of the low elastic constant direction but also to an isotropic crystal with the same higher but uniform elastic constant[36].

In-plane thermal anisotropy is also possible in thin film vdW materials that's not strictly 2D, from a structural point of view. Lee and Wu *et al.* investigated the anisotropic in-plane κ in black phosphorus nanoribbons. From their density functional theory calculations, they concluded that thermal anisotropy arose from the direction-dependent phonon dispersion[37]. Along the zigzag and armchair directions, the slope of the phonon branches was different, leading to a higher average group velocity along the zigzag direction compared to the armchair direction. A smaller contributing factor to black phosphorus's thermal anisotropy was the orientation dependent phonon-phonon scattering, the researchers found. The phonon scattering rate along the zigzag direction is lower than along the armchair direction. As a result, black phosphorus has an in-plane thermal anisotropy ratio of up to two. Given its naturally puckered structure, that black phosphorus is anisotropic in-plane may not come as a surprise.

Significant effort has been made towards engineering artificially anisotropic thermal conductors from largely and inherently 3D isotropic materials. One method is to introduce highly oriented, low dimensional defects. Sun and Koh *et al.* demonstrated anisotropic thermal transport of $\rho \leq 9$ in epitaxially grown InN films on GaN substrates, in which strain introduced during film growth caused threading dislocations (line defects) to form, oriented out of plane (Fig. 2.4A). The difference in the directionality of the scattering, which were the typical Umklapp scattering out of plane and the scattering by dislocations in plane, was the primary cause for anisotropic thermal transport. ρ became more pronounced at lower temperatures, when shorter, Umklapp-scattering-prone phonons were suppressed and the longer wavelength, in-plane phonons susceptible to scattering by the dislocations became the predominant heat carriers.

The most common technique to transform isotropic materials to anisotropic solids is via the fabrication of superlattices, by conjoining two or more materials, dissimilar in terms of their vibrational properties, in a periodic fashion. Examples include layered superlattices made from GaAs/AlAs, Si/Ge (Fig. 2.4B), Mo/Si, or Au/Si. Ideally, the goal is to incorporate a high density of parallel interfaces that are disruptive to through-plane thermal transport, while attaining perfect crystalline order within each constituent layer.

Fabrication-wise, such a goal remains a challenge and undermines the theoretical ρ value achievable. The deposition of these superlattices via sputtering or chemical vapor deposition is limited by the roughness of the interface, which might scatter in-plane phonons, as well as the thickness of each deposited layer. Consequently, this limits the out-of-plane resolution and hence the density of the interfaces that can be introduced. These deposition methods also tend to generate nanocrystalline films, thereby limiting the in-plane thermal transport compared to the single crystalline ideal. Moreover, atomic intermixing tends to occur at the interfaces, leading to further scattering of the in-plane phonons and reduction in the in-plane κ value.

Molecular beam epitaxy is an alternative method to generate near-single crystalline films and atomically sharp interfaces (Fig. 2.4C). However, depending on the lattice mismatch, the strain induced at the interfaces between the different layers may undermine the in-plane thermal conductivity[38–40], on top of the generation of phonon scattering growth defects such as dislocations that propagate from the interface, as shown by the example in Fig. 2.4A. Non-uniform strain may further increase scattering of phonons.

It is generally challenging to decouple the directional dependence of the material quality during the fabrication process. This hampers the value of ρ in superlattices, when the slashing of

thermal transport in one direction also inadvertently undercuts the thermal conductivity in other directions. Despite best efforts, ρ in superlattices fabricated from inherently isotropic constituent materials typically fall around 1–10.

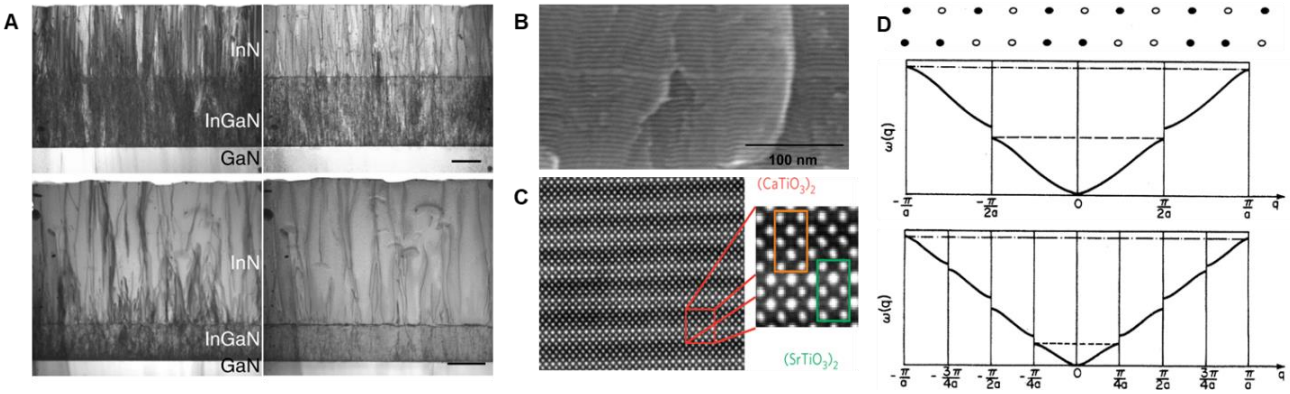

Figure 2.4 Examples of artificially generating thermal anisotropy in largely isotropic materials. (A) Epitaxially grown InN/GaN films with threading dislocations primarily reduces thermal conductivity in the in-plane direction. Scale bars represent 500 nm. Reproduced from reference [41]. (B) Sputtered grown ZrN/SrN films, imaged using scanning electron microscopy. Reproduced from reference [42]. (C) High angle annular dark field transmission electron microscopy image of $CaTiO_3/SrTiO_3$ films grown via molecular beam epitaxy, which resulted in atomically sharp and coherent interfaces in the superlattice. The periodicity of the superlattice is about 1 nm. Reproduced from reference [43]. (D) Theoretical calculations of the effect of a superimposing larger unit cell that leads to zone folding, whereby a larger enveloping periodicity in real space translates to a smaller Brillouin Zone with the generation of mini bands. Crystalline superlattices may suppress thermal conductivity via the zone folding effect. Reproduced from reference [9].

It is easier to attain a large anisotropy if one improves upon the ratio of an intrinsically anisotropic material with a giant ρ to begin with. Materials such as low dimensional vdW crystals are good candidates for these efforts because these materials have strongly anisotropic bonding. 1D and 2D materials make up the bulk of these attempts.

Examples of thermally anisotropic materials are highly oriented assemblages of low dimensional materials, such as layers of 2D materials stacked together or mats of aligned nanowires or

nanotubes (e.g., [44]). Several strategies to generate thermal anisotropy with low dimensional materials include mixing them into matrices of isotropic poor thermal conductors, oftentimes polymers. Examples include adding carbon fiber[45], hBN nanosheets[46], and graphite nanoplatelets[47] embedded in epoxy.

Here, we will focus on boosting anisotropy in already highly anisotropic, inorganic low-dimensional materials themselves, so inorganic/organic composites will be outside the scope of this discussion. Given the availability of scalable production techniques of 2D films, their processibility and ease of alignment compared to 1D materials, this thesis will also focus on using 2D materials to quest for engineering thermal transport, especially high thermal anisotropy.

2.4.2 Engineering anisotropy using 2D vdW materials as building blocks

2D vdW layered materials are excellent candidates for fabricating artificial solids with ultrahigh thermal anisotropy. For starters, these materials have anisotropic bonding: Strong covalent bonds lock together the atoms in plane—conducive for efficient thermal transport—whereas weaker vdW forces hold the sheets together out of plane.

vdW forces, in particular, open up unique opportunities for engineering. vdW attractive forces are relatively weak and omnidirectional. The vdW forces between the layers can be broken and reversibly formed, and the monolayers can be reassembled without commensurate matching between the crystalline structure. As a corollary, the layers of the assembled solid can be strain free. Moreover, vdW forces allow for 2D materials of different chemical species to be stacked together. These unique properties allow for the assembly of solids with unprecedented structures. These include rotationally mismatched solids or heterostructures using any 2D vdW materials as the constituents, combined in any arbitrary layer sequence. Furthermore, the atomic thickness of

2D vdW monolayers provides ample novel opportunities for probing thermal transport at the nanoscale and for investigating interfacial phenomena for thermal anisotropy design.

The ρ values of 2D fall around the order of magnitude of ~100 for graphite and h-BN, and around 10-50 for TMD materials (with a notable exception of ~ 100 for ReS_2[48]). The single crystalline nature of the monolayers isolated from bulk crystals ensures the high in-plane κ. However, the difficulty in isolating these monolayers through exfoliation implies that there is little room for employing them for further engineering solids with tailored out-of-plane κ. This means that if we want to use 2D vdW solids for designing practical thermal conductors, we must look into material preparation techniques that are scalable. This usually involves bottom-up syntheses of vdW monolayers, such as gas-phase growth techniques.

Research by Pop *et al.* on vdW thin film heterostructures has demonstrated the layer-by-layer, combinatorial stacking of chemical-vapor-deposition grown monolayers from the TMD family and graphene (Fig. 2.5). The studies on stacked polycrystalline graphene, vdW heterostructures from different monolayers, and MoS_2/graphene superlattices show that a single monolayer is indeed thermally resistive, with no ballistic transport despite its thickness between one to three atoms. This is contrast with previous research from the same group that had demonstrated that phonons can travel ballistically in exfoliated few-layer MoS_2 up to over 100 nm in thickness [49]. In the vdW heterostructures, the researchers attained a through-plane κ that was on the order of air's or less. They observed a temperature difference across the interfaces of a single monolayer, and a thermal disequilibrium could be measured in every layer of the stack in the through-plane direction. In the graphene/MoS_2 superlattice, the same group proved that the interfaces of the dissimilar materials are the resistive bottleneck for heat transport; switching up the sequence of the monolayers or adding new monolayers to increase the total film thickness do not affect

overall through-plane conductance, as long as the number of dissimilar-material interfaces is the same (Fig. 2.5A). Pop *et al.* claim that the main factors limiting thermal conduction are the mass and rotational mismatch between the layers, and the difference in the vibrational spectra between each constituent material as heat flows from one monolayer to the next.

In some of these studies, especially those involving multilayer graphene stacking, the researchers detected via cross-sectional STEM contamination between the monolayers, likely introduced during the stacking process (Fig. 2.5E). This probably contributed towards the ultralow through-plane thermal transport in the assembled material, since contamination is known to scatter heat carriers. Moreover, the discontinuous films or micron-sized flakes for some of the monolayers hamper in-plane transport, rendering the definition of ρ inapplicable in this material and highlighting the scalability challenge in assembled vdW layered films (Fig. 2.5D). Small-area films impose a limit to the total number of monolayers that can be stacked into a single film. Other studies investigating the vertical assembly of 2D vdW heterofilms have a limited layer number in their stacks despite starting with large-area CVD-grown monolayers, possibly due to fabrication limitations.

Johnson *et al.* conceived a one-pot synthesis method of multilayered TMD films with rotational disorder (Figs. 2.6A, B). Using the modulated elemental reactants method, the researchers deposited alternating layers of metal and chalcogens, then annealed the layers at high temperatures to stimulate the reaction and formation of the interlayer rotated film[53–55]. Cross-sectional TEM images revealed that the layers were pristine, allowing the researchers to isolate the effect of interlayer rotation on thermal transport. One of their synthesized films, WSe_2 with rotational disorder achieved a record-breaking through-plane κ for a fully dense solid that was comparable to that of air[56]. Further studies on other films and superlattices deposited the same

way showed that these films tend to have nanocrystalline domains in the in-plane direction. Hence, the overall ρ was ~ 30 despite the drastic reduction in through-plane κ. This research highlights the challenge of decoupling the directional dependences of thermal conduction in 3D, fully dense solids via nanostructuring.

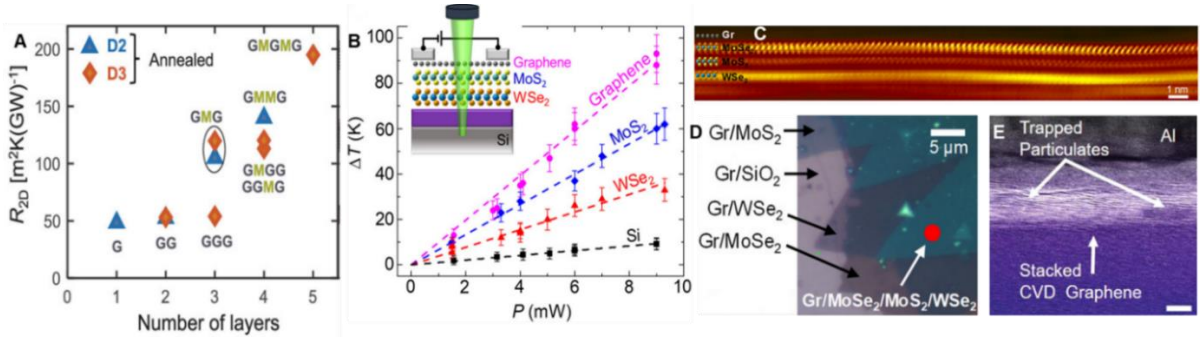

Figure 2.5 Layer-by-layer stacked multilayer vdW films for thermal engineering, by Pop *et al.* (A) Interfacial thermal resistances of stacked graphene (G)/MoS_2 (M) heterostructures. D2 and D3 denote the 2 different stacked samples. Reproduced from reference [50]. (B) Temperature rise across each monolayer in stacked 2D vdW films from graphene, $MoSe_2$, MoS_2, and WSe_2, measured via Raman thermometry. The dark-field TEM image of a film cross section is shown in (C). Both figures are reproduced from reference [51]. The optical images of these films are shown in (D), which is reproduced from reference [50]. (E) Stacked polycrystalline graphene layers with trapped particulates believed to be etchant residues, imaged via bright-field scanning transmission electron microscopy. The scale bar is 5 nm. Reproduced from reference [52].

An ultrahigh ρ value was reported by Renteria and Balandin *et al.* in their reduced graphene oxide films[57]. Annealing liquid processed graphene oxide flakes at 1000 ºC partially reduced the graphene oxide and lowered the defect concentration, thereby increasing the in-plane thermal conductivity. This annealing step also created micron-sized air pockets between the layers (Fig. 2.6C)—the films bulged fourfold in volume post-treatment. The consequence of the air pockets was that the through-plane κ fell twofold to 0.09 W m^{-1} K^{-1}, resulting in strong anisotropy of ρ ~ 675 in the film. The research raises the question whether ultrahigh thermal anisotropy can be

created in a fully dense solid made from vdW layered crystals, without the presence of air pockets or defects and from intrinsic vdW layered materials to begin with.

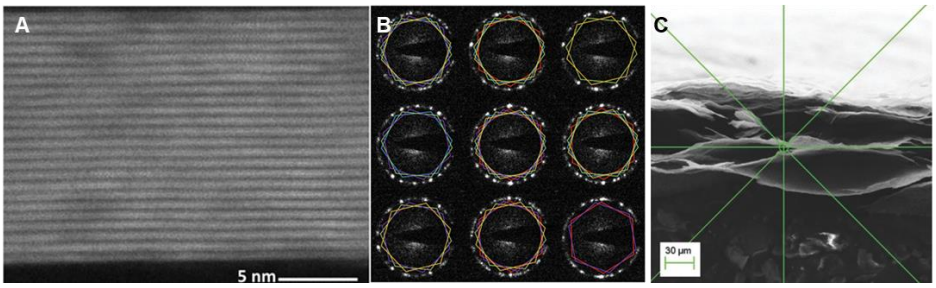

Figure 2.6 Batch synthesis of stacked vdW films. (A) Cross sectional STEM image of 24-layer turbostratic $MoSe_2$ films by Johnson *et al.*, using the modulated elemental reactants method. (B) Map of selected-area nanobeam electron diffraction patterns of turbostratic $MoSe_2$. Each measurement spot is separated by 10 nm. The color of the hexagons represent the grain orientations. Both figures are reproduced from reference [55]. (C) SEM image pf cross section of annealed reduced graphene oxide films by Balandin *et al.* Reproduced from reference [57].

Other efforts include dynamically tuning ρ in bulk TMD crystals. Zhu and Cahill *et al.* discovered that lithiating bulk and CVD-grown MoS_2 crystals increased the anisotropy in thermal conductivity (Figs. 2.7A, B)[58]. Electrochemically intercalated lithium ions boosted ρ by increasing disorder in the through-plane direction to a larger degree than in the in-plane direction. The researchers increased ρ from 52 in the pristine state to a high of 110 by tuning the lithium composition. Nevertheless, while to a lesser extent, lithiation still reduced in-plane κ.

Another method to dynamically tune the thermal properties of 2D vdW crystals is by applying extreme vertical strain, though experiments show this method demonstrably reduces anisotropy. Meng and Wang *et al.* compressed bulk MoS_2 in a diamond anvil cell and achieved a 9 % compressive strain in the through-plane direction (Figs. 2.7C, D)[59]. The result was a smaller interlayer vdW gap which strengthened the interlayer forces and improved v_g, thereby increasing

through-plane κ nearly tenfold. On the other hand, in-plane κ increases non-monotonically to a smaller extent. Overall, ρ decreased from ~ 25 to ~ 3 when a pressure of 20 GPa was applied.

As a general strategy to maximize ρ, one needs to retain κ along the fast-conduction direction as much as possible. It has been a challenge to reliably reduce κ in one direction only, while leaving κ in other directions unmodified.

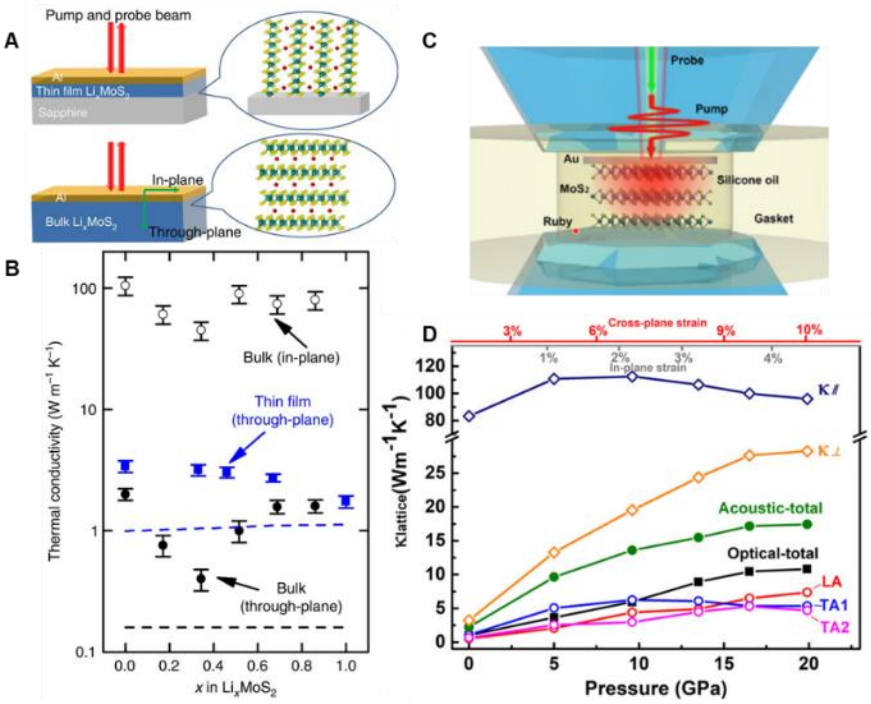

Figure 2.7 Tuning thermal conductivity and anisotropy in 2D vdW crystals. (A) Schematic of Li intercalation into thin film deposited and bulk MoS_2. The measured thermal conductivity by Cahill *et al.* is presented in (B). Both these images were reproduced from reference [58]. (C) Schematic of pressure tuning MoS_2 in a diamond anvil cell and its thermal measurement via an optical pump probe method. The results by Wang *et al.* are presented in (D). Both these images were reproduced from reference [59].

2.5 Thermal metrologies for thin films

Thermal conductivity is challenging to measure, even more so in nanomaterials in which multiple heat loss channels and interface effects exist. Commercially available techniques such

as the laser flash method, steady-state Joule heating, and the hot-disk method work only on large bulk samples with dimensions of over several hundred microns, because the active components or heater elements are around that size or larger[60]. The measurement of thermal transport in thin films requires generating a temperature gradient at nano or microscale lengths, or highly sensitive transient methods that can capture heat dissipation timescales on the order of microseconds. We will discuss several of the most common techniques for thin film thermal measurements here in this section, noting that this is not an exhaustive list (Fig. 2.8).

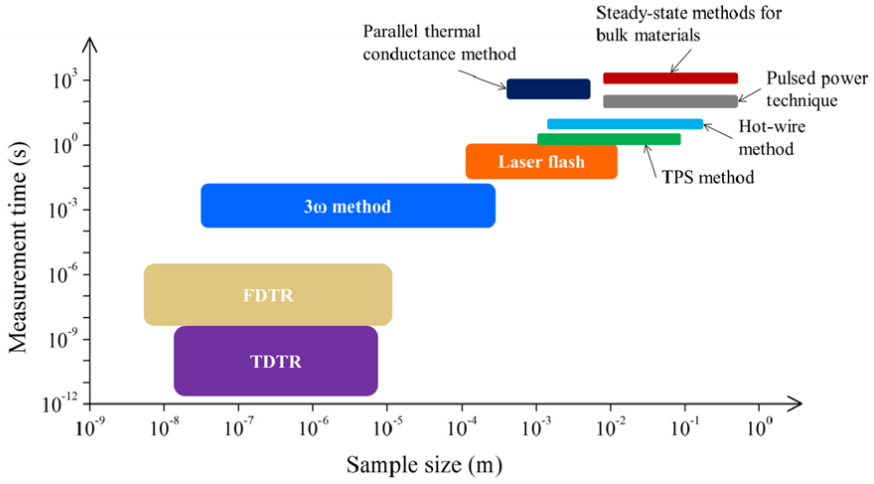

Figure 2.8 Thermal measurement techniques. Which technique to apply depends on the spatial extent of the temperature gradient and the heating period, both of which should be low for smaller samples. Reproduced from reference [60].

2.5.1 Electrothermal methods

Using nanofabrication techniques, nano to microscale heater lines can be fabricated onto thin film samples and act as a heat source through Joule heating. The electrical resistance of this heater line is the readout for the temperature of the surface, thereby revealing the heat dissipation efficiency beneath the heater surface.

Heating can be performed with a D.C. current as a steady state measurement; heating with an A.C. current increases the sensitivity of the measurement for thin samples if lock-in detection is also used. If one heats the metallic line with a sinusoidal current at a frequency of ω, the electrical resistance which is proportional to temperature rise manifests in the third harmonic, 3ω (Fig. 2.9A). This 3ω method is often used to measure the through-plane κ of thin film samples on substrates. Changing the heating frequency ω will alter the through-plane confinement in the fluctuating temperature field near the surface. This method has been used to probe the through-plane thermal conductivity of SiO_2, Si, Ge, and superlattice thin film materials, ranging between 50 nm to 3 μm in thicknesses[61]. By changing the heating frequency, the heater line width, and the sample geometry (such as creating suspended islands from the material rather than continuous films), the in-plane thermal properties of the material can also be probed. Other variations include strategically placing new electrical sensor lines near the heating zone that can pick up the film temperature at a distance from the heat source, thereby revealing the in-plane thermal conduction (Fig. 2.9B)[52]. Electrothermally measuring the in-plane thermal conductivity can also be performed by fashioning the thin film into suspended strips (e.g., Fig. 2.9C), in a technique known as the microbridge method. These modifications to the electrical thermometry method demands significant nanofabrication and sample preparation.

Another downside of contact-based, electrothermal methods is the need to account for interfacial thermal resistances in the measurements. To prevent current leakage from the electrical heater to an electrically conducting film, additional layers of insulation need to be built around the heater line, which complicates the thermal measurement by adding on thermal resistors that may be of unknown magnitude. One method to overcome this problem is to fabricate multiple samples with different thicknesses in the film of interest. Everything else being constant, the variation in the

temperature rise measured can be assumed to come from the thickness differences, and the interfacial thermal resistances can be subtracted as the background. Nevertheless, one can observe that this method has slightly reduced sensitivity to samples that are extremely thin, especially if the interfacial thermal resistance is high.

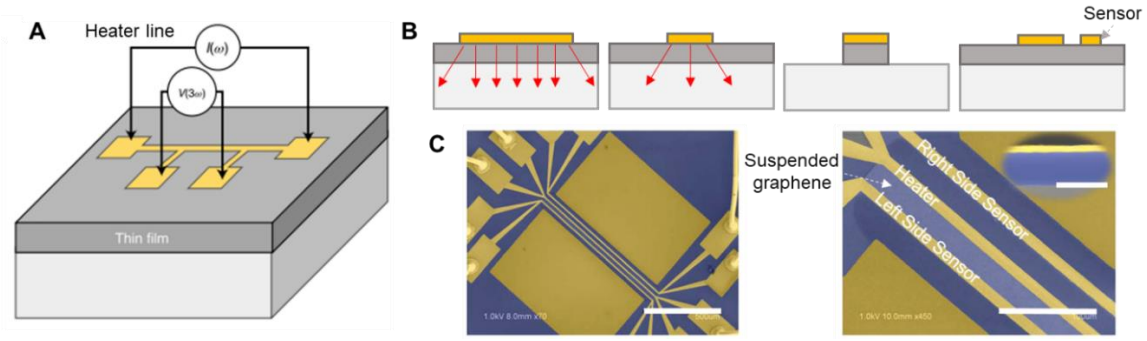

Figure 2.9 Electrothermal methods for measuring the thermal conductivity of thin film materials. (A) Schematic of the 3ω method. Reproduced from reference [14]. (B) Variations of the 3ω method for measuring in-plane thermal conduction. Reproduced from reference [61]. (C) Scanning electron microscopy image of suspended graphene between Au heater and sensor lines for its in-plane thermal characterization. The scale bars are 500 μm (left images) and 100 μm (right image, bottom right corner), and 300 nm (right image, top right corner) respectively. Reproduced from reference [52].

2.5.2 Noncontact, optical methods

These methods typically use light sources to deliver heating to the sample. Besides bypassing the creation of new additional interfacial thermal resistances, this method also requires minimal sample preparation, and hence has lower chances of introducing defects or damage to the delicate thin film sample.

The temperature readout typically involves probing an optical response that is sensitive to temperature. Examples include the Raman signal of a Raman active thin film sample, or depositing metal transducer layer, whose reflectance is indicative of temperature. Steady-state

techniques, such as Raman thermometry, usually apply to the measurement of the in-plane properties of suspended samples. Standard Raman thermometry techniques use a continuum-wave laser to heat a thin film that also reads out the film temperature from the Raman peak position simultaneously. This peak position needs to be calibrated to the temperature beforehand and is usually linear with respect to the temperature. One modification of this technique was carried out by Vaziri and Pop *et al.* and is presented in Fig. 2.5B[51]. In this report, the researchers measured the through-plane conductance of a 4-layer stacked graphene/$MoSe_2$/MoS_2/WSe_2 by probing the temperatures across every interface by observing the characteristic Raman signatures of each monolayer. This feat was attainable via a steady state Raman thermometry method, given that the 4-layer heterostructure is thermally resistive enough to sustain a temperature gradient across each monolayer, and the characteristic Raman shifts of the 4 disparate vdW monolayers do not overlap.

Given the atomic or nanoscale thinness of 2D materials, generally transient techniques are needed to measure through-plane thermal transport. The method time-domain thermoreflectance (TDTR) is a pump-probe technique that relies on ultrafast pulsed lasers to generate and measure heating. TDTR measures the thermoreflectance decay of a metal transducer layer deposited on the film surface as a function of the time delay between the probe beam relative to the pump beam (Fig. 2.10A). A similar method called frequency-domain thermoreflectance (FDTR) instead uses continuous-wave laser heating that is frequency modulated, which changes the penetration depth of the thermal wave into the sample. FDTR measures thermoreflectance as a function of heating frequency (Fig. 2.10B).

Compared to other thin film techniques, these optical transient methods usually have sufficient sensitivity to separate out the effects of the thin film and its interfaces during measurement, provided the film is sufficiently resistive.

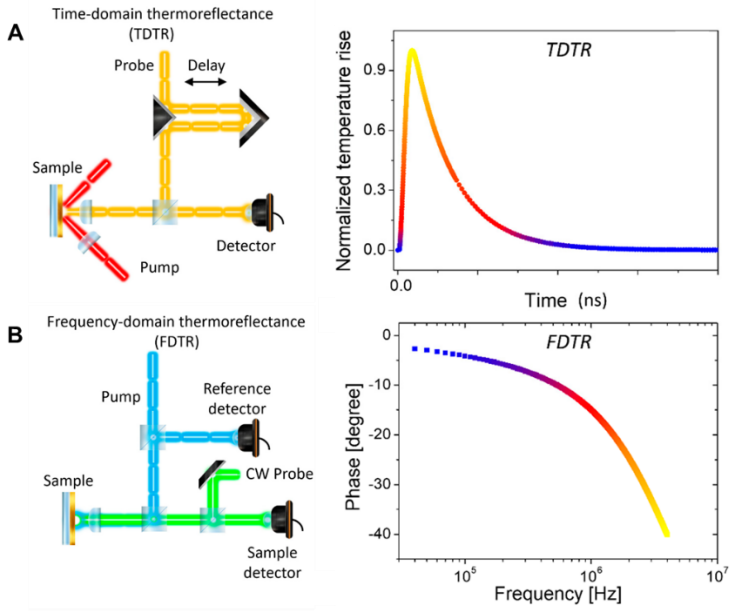

Figure 2.10 Transient pump probe thermal measurement methods. (A) Schematic of experiment configuration and example data of TDTR. (B) Schematic of experiment configuration and example data of FDTR. The images here are reproduced from reference [62].

For sufficiently thick and thermally resistive samples of at least ~ 100 nm in thickness, TDTR and FDTR can be adapted to measure the in-plane properties, although complete confinement of heat flow along the in-plane direction is not possible. An elliptical pump, pump-probe spatial offset, and varying the pump spot size are ways to enable in-plane thermal measurement of thin films.

2.5.3 Challenges in thermal metrology for thin films

The thinness of nanomaterials makes measuring their thermal transport properties challenging. Ultimately, thermal measurements “feel” thermal resistance rather than resistivity. Despite

ultrahigh thermal resistivity, the thinness of a material will translate to a low resistance value that a measurement method may not be able to detect. For techniques that measure κ using a comparative method among samples with and without the nanomaterial of interest, the presence of this nanomaterial may not be perceptibly different compared to the control sample/blank substrate. Also for this reason, high-κ nanomaterials are especially challenging to measure.

Nanomaterials are extraordinarily sensitive to their environment. Contact methods usually require sample processing, and this might alter the quality of the material of interest and hence reduce its measured thermal conductivity from the pristine value.

The intrinsic κ of a film may be challenging to decouple from its interfaces, especially if the interfacial thermal resistance values dominate over the overall resistance. For the through-plane transient thermal transport measurement of thin films, the thinness of the material might pose a challenge for spatially and temporally separating thermal transport between the interfaces and the film.

Measuring the intrinsic thermal conductivity of thin film materials also requires the measurement of parameters other than temperature that are relevant to solve the thermal energy balance equation. This includes the heat capacity and the material dimensions. In the next chapter, we demonstrate how the precise control of the film dimensions allows us to calculate the intrinsic value of κ from extrinsic thermal conductance.

2.6 Summary

This chapter presented several real-world strategies to modify κ at large, then gradually focused on the role of 2D materials in assembling high-anisotropy solids. The main challenge for

employing 2D materials is fabrication: to retain their excellent qualities and keep the materials at a scale that's practically useful.

The next chapter will introduce one method that makes the directional dependence of thermal engineering possible. Here, we will show how we used 2D vdW materials to assemble highly anisotropic artificial solids. We used two techniques mentioned here—Raman thermometry and TDTR—to measure their thermal properties along different directions. For the cross-plane measurement, we chose TDTR for its sensitivity that makes it a suitable technique for measuring ultrathin materials.

2.7 References

1. Li, Y., Wang, J. & Wang, J. Approaching extremely low thermal conductivity by crystal structure engineering in Mg2Al4Si5O18. *Journal of Materials Research* **30**, 3729–3739 (2015).

2. Xu, X. *et al.* Double-negative-index ceramic aerogels for thermal superinsulation. *Science (1979)* **363**, 723–727 (2019).

3. Wei, L., Kuo, P. K., Thomas, R. L., Anthony, T. R. & Banholzer, W. F. Thermal conductivity of isotopically modified single crystal diamond. *Physical Review Letters* **70**, 3764 (1993).

4. Benton, T. G. Managing farming's footprint on biodiversity. *Science* vol. 315 341–342 (2007).

5. Chen, Z., Zhang, X. & Pei, Y. Manipulation of Phonon Transport in Thermoelectrics. *Advanced Materials* vol. 30 1705617 (2018).

6. Tan, G. *et al.* High Thermoelectric Performance in SnTe-AgSbTe2 Alloys from Lattice Softening, Giant Phonon-Vacancy Scattering, and Valence Band Convergence. *ACS Energy Letters* **3**, 705–712 (2018).

7. Daniel, M. v. *et al.* Structural and thermoelectric properties of FeSb3 skutterudite thin films. *Physical Review B - Condensed Matter and Materials Physics* **91**, 085410 (2015).

8. Nolas, G. S., Morelli, D. T. & Tritt, T. M. SKUTTERUDITES: A Phonon-Glass-Electron Crystal Approach to Advanced Thermoelectric Energy Conversion Applications. *http://dx.doi.org/10.1146/annurev.matsci.29.1.89* **29**, 89–116 (2003).

9. Ren, S. Y. & Dow, J. D. Thermal conductivity of superlattices. *Physical Review B* **25**, 3750–3755 (1982).

10. Mizuno, H., Mossa, S. & Barrat, J. L. Beating the amorphous limit in thermal conductivity by superlattices design. *Scientific Reports* **5**, (2015).

11. Singh, D. J. & Terasaki, I. Thermoelectrics: Nanostructuring and more. *Nature Materials* vol. 7 616–617 (2008).

12. Biswas, K. *et al.* High-performance bulk thermoelectrics with all-scale hierarchical architectures. *Nature* **489**, 414–418 (2012).

13. Cahill, D. G., Watson, S. K. & Pohl, R. O. Lower limit to the thermal conductivity of disordered crystals. *Physical Review B* **46**, 6131–6140 (1992).

14. Qian, X., Zhou, J. & Chen, G. Phonon-engineered extreme thermal conductivity materials. *Nature Materials* **20**, 1188–1202 (2021).

15. Toberer, E. S., Baranowski, L. L. & Dames, C. Advances in Thermal Conductivity. *Annu. Rev. Mater. Res* **42**, 179–209 (2012).

16. McConnell, A. D. & Goodson, K. E. *Thermal Conduction in Silicon Micro- and Nanostructures*. *Annual Review of Heat Transfer* vol. 14 (2013).

17. Jana, M. K. & Biswas, K. Crystalline Solids with Intrinsically Low Lattice Thermal Conductivity for Thermoelectric Energy Conversion. *ACS Energy Letters* vol. 3 1315–1324 (2018).

18. Hopkins, P. E. Thermal Transport across Solid Interfaces with Nanoscale Imperfections: Effects of Roughness, Disorder, Dislocations, and Bonding on Thermal Boundary Conductance. *ISRN Mechanical Engineering* **2013**, 1–19 (2013).

19. Losego, M. D., Grady, M. E., Sottos, N. R., Cahill, D. G. & Braun, P. v. Effects of chemical bonding on heat transport across interfaces. *Nature Materials* **11**, 502–506 (2012).

20. Kaur, S., Raravikar, N., Helms, B. A., Prasher, R. & Ogletree, D. F. Enhanced thermal transport at covalently functionalized carbon nanotube array interfaces. *Nature Communications* **5**, 1–8 (2014).

21. Wang, Q., Wang, X., Liu, X. & Zhang, J. Interfacial engineering for the enhancement of interfacial thermal conductance in GaN/AlN heterostructure. *Journal of Applied Physics* **129**, 235102 (2021).

22. Ghosh, S. *et al.* Dimensional crossover of thermal transport in few-layer graphene. *Nature Materials* **9**, 555–558 (2010).

23. Donadio, D. Simulation of dimensionality effects in thermal transport. *Lecture Notes in Physics* **921**, 275–304 (2016).

24. Nika, D. L. & Balandin, A. A. Two-dimensional phonon transport in graphene. *Journal of Physics Condensed Matter* vol. 24 233203 (2012).

25. Ghosh, S. *et al.* Extremely high thermal conductivity of graphene: Prospects for thermal management applications in nanoelectronic circuits. *Appl. Phys. Lett* **92**, 151911 (2008).

26. Xu, X. *et al.* Length-dependent thermal conductivity in suspended single-layer graphene. *Nature Communications 2014 5:1* **5**, 1–6 (2014).

27. Marconnet, A. M., Asheghi, M. & Goodson, K. E. From the Casimir limit to phononic crystals: 20 years of phonon transport studies using silicon-on-insulator technology. *Journal of Heat Transfer* **135**, (2013).

28. Zhou, Y. & Hu, M. Record Low Thermal Conductivity of Polycrystalline Si Nanowire: Breaking the Casimir Limit by Severe Suppression of Propagons. *Nano Letters* **16**, 6178–6187 (2016).

29. Cepellotti, A. *et al.* Phonon hydrodynamics in two-dimensional materials. *Nature Communications 2015 6:1* **6**, 1–7 (2015).

30. Huberman, S. *et al.* Observation of second sound in graphite at temperatures above 100 K. *Science (1979)* **364**, 375–379 (2019).

31. Guyer, R. A. & Krumhansl, J. A. *Thermal Conductivity, Second Sound, and Phonon Hydrodynarmc Phenomena in Nonmetallic Crystals**. vol. 148 https://journals.aps.org/pr/pdf/10.1103/PhysRev.148.778 (1966).

32. Chen, R. *et al.* Thermal Conductance of Thin Silicon Nanowires. *Physical Review Letters* **101**, 105501 (2008).

33. Neogi, S. *et al.* Tuning Thermal Transport in Ultrathin Silicon Membranes by Surface Nanoscale Engineering. *ACS Nano* **9**, 3820–3828 (2015).

34. Touloukian, Y. S., Liley, P. E. & Saxena, S. C. *Thermophysical Properties of Matter - The TPRC Data Series. Volume 3. Thermal Conductivity - Nonmetallic Liquids and Gases*. https://apps.dtic.mil/sti/citations/ADA951937 (1970).

35. von Gutfeld, R. J. & Nethercot, A. H. Heat pulses in quartz and sapphire at low temperatures. *Physical Review Letters* **12**, 641–644 (1964).

36. Wei, Z., Chen, Y. & Dames, C. Negative correlation between in-plane bonding strength and cross-plane thermal conductivity in a model layered material. *Applied Physics Letters* **102**, 11901 (2013).

37. Lee, S. *et al.* Anisotropic in-plane thermal conductivity of black phosphorus nanoribbons at temperatures higher than 100 K. *Nature Communications 2015 6:1* **6**, 1–7 (2015).

38. Xu, L., Zhang, X. & Zheng, Y. Local strain effect on the thermal transport of graphene nanoribbons: a molecular dynamics investigation. *Physical Chemistry Chemical Physics* **17**, 12031–12040 (2015).

39. Zhang, X. & Wu, G. Effect of Strain on Thermal Conductivity of Si Thin Films. *Journal of Nanomaterials* **2016**, (2016).

40. Li, X., Maute, K., Dunn, M. L. & Yang, R. Strain effects on the thermal conductivity of nanostructures. *Physical Review B - Condensed Matter and Materials Physics* **81**, 245318 (2010).

41. Sun, B. *et al.* Dislocation-induced thermal transport anisotropy in single-crystal group-III nitride films. *Nature Materials* **18**, 136–140 (2018).

42. Rawat, V., Koh, Y. K., Cahill, D. G. & Sands, T. D. Thermal conductivity of (Zr,W)N/ScN metal/semiconductor multilayers and superlattices. *Journal of Applied Physics* **105**, 24909–2957 (2009).

43. Ravichandran, J. *et al.* Crossover from incoherent to coherent phonon scattering in epitaxial oxide superlattices. *Nature Materials* **13**, (2013).

44. Qiu, L. *et al.* Remarkably enhanced thermal transport based on a flexible horizontally-aligned carbon nanotube array film. *Scientific Reports 2016 6:1* **6**, 1–14 (2016).

45. Joven, R., Das, R., Ahmed, A., Roozbehjavan, P. & Minaie, B. Thermal properties of carbon fiber-epoxy composites with different fabric weaves. *SAMPE International Symposium Proceedings At Charleston, SC* (2012).

46. Wu, Y. *et al.* BN Nanosheet/Polymer Films with Highly Anisotropic Thermal Conductivity for Thermal Management Applications. *ACS Applied Materials and Interfaces* **9**, 43163–43170 (2017).

47. Tian, X., Itkis, M. E., Bekyarova, E. B. & Haddon, R. C. Anisotropic Thermal and Electrical Properties of Thin Thermal Interface Layers of Graphite Nanoplatelet-Based Composites. *Scientific Reports 2013 3:1* **3**, 1–6 (2013).

48. Jang, H., Ryder, C. R., Wood, J. D., Hersam, M. C. & Cahill, D. G. 3D Anisotropic Thermal Conductivity of Exfoliated Rhenium Disulfide. *Advanced Materials* **29**, 1700650 (2017).

49. Sood, A. *et al.* Quasi-Ballistic Thermal Transport Across MoS2 Thin Films. *Nano Letters* **19**, 2434–2442 (2019).

50. Sood, A. *et al.* Engineering Thermal Transport across Layered Graphene-MoS2 Superlattices. *ACS Nano* **15**, 19503–19512 (2021).

51. Vaziri, S. *et al.* Ultrahigh thermal isolation across heterogeneously layered two-dimensional materials. *Science Advances* **5**, 1325–1341 (2019).

52. Estrada, D. *et al.* Thermal transport in layer-by-layer assembled polycrystalline graphene films. *npj 2D Materials and Applications* **3**, (2019).

53. Hadland, E. *et al.* Synthesis, Characterization, and Ultralow Thermal Conductivity of a Lattice-Mismatched SnSe2(MoSe2)1.32 Heterostructure. *Chemistry of Materials* **31**, 5699–5705 (2019).

54. Chiritescu, C. *et al.* Low thermal conductivity in nanoscale layered materials synthesized by the method of modulated elemental reactants. *Journal of Applied Physics* **104**, 802 (2008).

55. Hadland, E. C. *et al.* Ultralow thermal conductivity of turbostratically disordered MoSe2 ultra-thin films and implications for heterostructures. *Nanotechnology* **30**, (2019).

56. Chiritescu, C. *et al.* Ultralow Thermal Conductivity in Disordered, Layered WSe2 Crystals. *Science (1979)* **315**, 351–353 (2007).

57. Renteria, J. D. *et al.* Strongly Anisotropic Thermal Conductivity of Free-Standing Reduced Graphene Oxide Films Annealed at High Temperature. *Advanced Functional Materials* **25**, 4664–4672 (2015).

58. Zhu, G. *et al.* Tuning thermal conductivity in molybdenum disulfide by electrochemical intercalation. *Nature Communications* **7**, (2016).

59. Meng, X. *et al.* Thermal Conductivity Enhancement in MoS 2 under Extreme Strain. *Physical Review Letters* **122**, (2019).

60. Zhao, D., Qian, X., Gu, X., Jajja, S. A. & Yang, R. Measurement techniques for thermal conductivity and interfacial thermal conductance of bulk and thin film materials. *Journal of Electronic Packaging, Transactions of the ASME* **138**, (2016).

61. Dames, C. Measuring the Thermal Conductivity of Thin Films: 3 Omega and Related Electrothermal Methods. *Annual Review of Heat Transfer* **16**, 7–49 (2013).

62. el Sachat, A., Alzina, F., Sotomayor Torres, C. M. & Chavez-Angel, E. Heat transport control and thermal characterization of low-dimensional materials: A review. *Nanomaterials* vol. 11 1–32 (2021).

CHAPTER 3: OBSERVATIONS OF GIANT THERMAL CONDUCTIVITY ANISOTROPY IN STACKED 2D VDW FILMS

3.1 Introduction

Engineering anisotropy from isotropic materials is challenging; most engineered anisotropic thermal conductors have a thermal anisotropy ratio $\rho = \frac{fast-axis\ \kappa}{slow-axis\ \kappa} \leq 20$. Natural materials with giant $\rho > 100$—graphite and hBN are notable examples raised in the previous chapter—still have some degree of symmetry (such as crystallinity along three dimensions). That means, despite their already high anisotropy, their ρ can still be increased, if fabrication techniques can break these symmetries. The work presented in this chapter and the next, based on my publication in *Nature*[1], discusses one method to create extremely anisotropic thermal conductors.

In general, any approach to design materials with high ρ needs to satisfy these conditions: i) a candidate material with intrinsically high κ in at least one direction to begin with, usually one with efficient phonon-mediated thermal transport; ii) a method to significantly reduce κ without affecting the value along the fast axis; and iii) facile, scalable production of such a material with precise control of the material dimensions (e.g., film thickness). We use 2D vdW layered crystals as the building blocks for generating high ρ solids. In single crystalline form, these solids have excellent intrinsic in-plane thermal conductivity $\kappa_{||}$, satisfying the first condition. Their through-plane weak vdW bonding gives rise to a much lower κ along that direction. Moreover, vdW forces allow monolayers to be stacked together free of strain and without crystalline alignment simply by bringing the sheets into close contact. This provides a method to further tune the through-plane thermal conductivity $\kappa_{\perp}$ by controlling the through-plane structure of the assembled solid, thereby providing access to the second condition. Lastly, as per the third

condition, there are established methods to synthesize TMD monolayers at the wafer scale and then assemble them layer by layer with atomic precision. This chapter will demonstrate how we applied existing techniques to propose a general approach to decreasing $\kappa_{\perp}$ not at the expense of $\kappa_{||}$, creating ultrahigh ρ solids assembled from 2D vdW layered crystals.

The central concept for generating our thermally anisotropic solids is interlayer rotations in stacked 2D vdW solids as a means to generate maximally anisotropic crystals in terms of the structural crystallinity (Fig. 3.1). Interlayer rotation breaks the through-plane translational symmetry at the atomic scale while retaining the long-range in-plane crystallinity in each monolayer, thereby providing an effective means to suppress only through-plane thermal transport. The interlayer rotations in our solids are random, so the films are disordered exclusively in the vertical direction. We also demonstrate that our films are large area and have large crystalline domains in-plane.

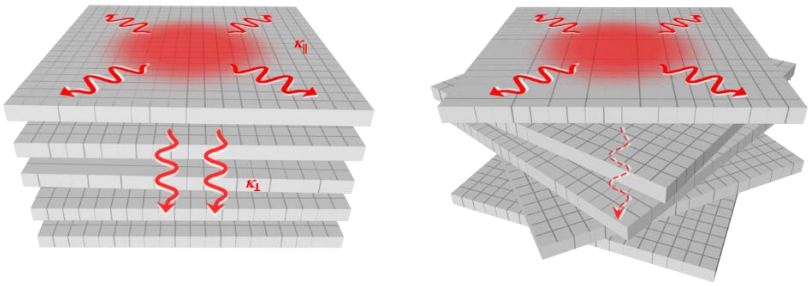

Figure 3.1 Conceptual strategy for engineering thermal anisotropy in a single material system, using interlayer rotation in vdW layered materials.

The goal of this chapter is to characterize the effect of interlayer rotation on thermal anisotropy, especially on the reduction in $\kappa_{\perp}$ via generating one-dimensional structural disorder. This chapter will detail the method of fabricating r-TMD thin films (the prefix r denotes films with interlayer

rotation), namely monolayer growth followed by stacking, and the experimental results from our thermal measurements of these materials.

3.2. Synthesis of r-TMD films

Large-area, polycrystalline monolayers of TMD (namely MoS_2 and WS_2) were grown using an established technique of metal-organic chemical vapor deposition (MOCVD) reported by Kang and Xie et al (Fig. 3.2A)[2]. This gas phase synthesis generates wafer-scale monolayers with well-stitched grains and tunable crystalline domain sizes.

The key features of this growth technique that enabled our r-TMD film preparation were as follows: The gas phase synthesis generated monolayers that were clean and largely free of contaminants, compared to those usually present in liquid-processed films. Having clean interfaces between rotationally misaligned films allowed us to isolate the impact of interlayer rotation on thermal transport. Secondly, the TMD monolayers were polycrystalline, with grain sizes ranging from several hundred nanometers to several microns. The polycrystalline nature of the monolayers, with random crystal alignment in plane, resulted in the films necessarily being randomly rotated in the through-plane direction when these monolayers were stacked. Despite the polycrystalline nature, these monolayers were well-stitched and continuous. So, they could be easily peeled off their growth substrates, as the monolayer-substrate interaction was purely weak vdW forces; the presence of grain defects and incomplete stitching would have pinned the monolayer to the substrate and hampered delamination from the substrate. Moreover, the crystalline domains were large relative to the film thickness ($\leq$ 15 nm). This, along with the interconnectedness of the domains, were crucial to retaining excellent in-plane thermal transport that was within an order of magnitude from the single crystalline value. The large area of the

monolayers allowed us to stack these films layer by layer to generate films amenable to thermal transport and anisotropy measurements. Previous stacking methods of CVD-grown flakes or exfoliated crystals yielded films with much smaller sizes, so the thermal measurements on these samples were local and not systematic.

Following the growth of these large-area monolayers, we generated multilayer assemblies using a previously developed method of programmed vacuum stack process reported by Kang and Lee *et al.* (Fig. 3.2B)[3] Stacking was carried out without the use of liquid etchants, since TMD monolayers could be peeled off directly from the substrate. The low-pressure environment of ~ 1 Torr during the stacking process itself further reduced potential contamination between the interfaces of the monolayers. On top of the polycrystalline nature of our films, the stacking process did not involve any alignment, so the crystalline domains between monolayers are completely randomly oriented. The layer-by-layer nature of the stacking process allowed us to achieve precise control of the atomic thickness of the resulting film.

The stacking conditions were relatively mild. For example, the film heating temperature during the stacking step itself was ~ 90 ºC. Further post-stacking bake of the film as conducted at 180 ºC while the film was capped with a PMMA layer that shielded the film from direct oxygen exposure. Annealing the film and substrate to remove this PMMA layer was performed under 400 SCCM/100 SCCM Ar/H_2 at 350 ºC, which is about 200 ºC lower than the monolayer growth temperature. As such, the in-plane properties of the monolayers were not altered during the stacking process. In fact, the two discrete growth and stacking steps allowed for the decoupling of the in-plane and out-of-plane properties of the film: The in-plane properties of the film are largely pre-determined by the growth process, and the out-of-plane properties are entirely dictated by stacking. Theoretically, given that the thermal properties of similarly assembled

solids along the horizontal and vertical directions can be independently tuned by the growth and stacking process respectively, this would allow for the tuning of ρ itself in the assembled material, the extent of which could be one avenue for future exploration.

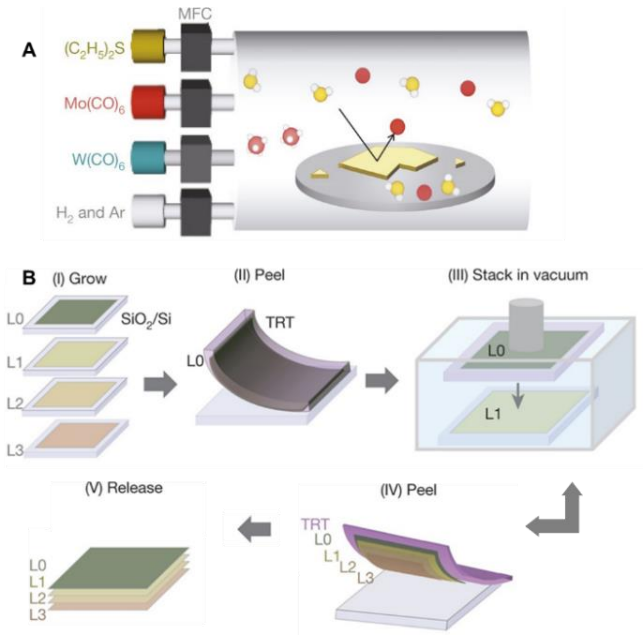

Figure 3.2 The r-TMD film fabrication technique. (A) Large-area, polycrystalline monolayer growth using gas-phase metal-organic chemical vapor deposition. (B) Programmed vacuum stacking of TMD monolayers to form films with interlayer rotation. The images are adapted from references [2] and [3].

3.3 Structural characterization of stacked films

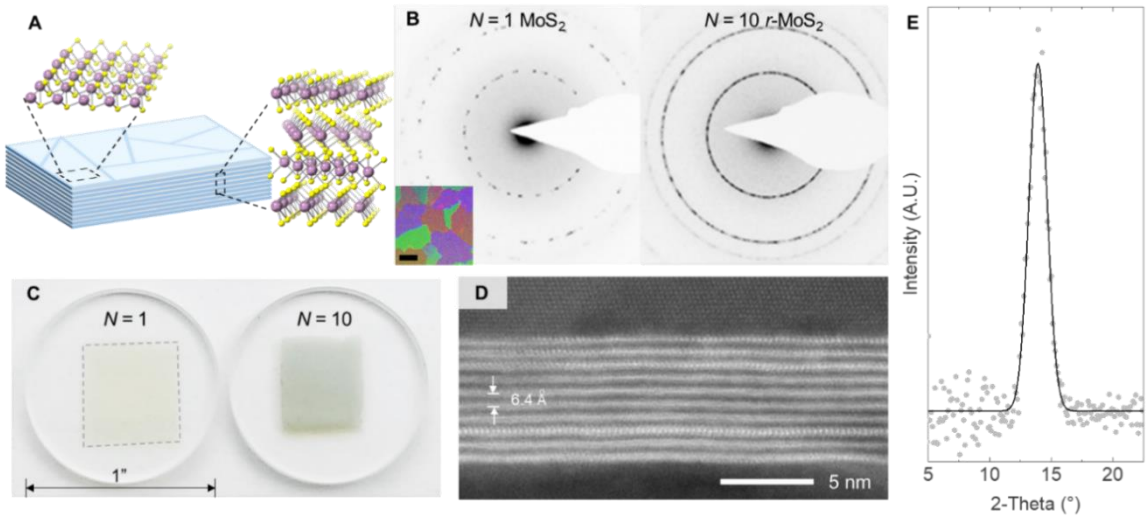

Figure 3.3 Structural characterization of r-TMD films. (A) Schematic of an r-TMD film with random crystalline orientation. (B) Grayscale-inverted TEM electron diffraction patterns, probed from a 500 nm x 500 nm area of a monolayer and a N = 10 r-MoS_2 film. Inset: Dark-field TEM image of a monolayer; the scale bar denotes 400 nm and the colors denote different grain orientations from different crystal domains. (C) Large-area MoS_2 films transferred onto 1-inch-diameter fused silica substrates. (D) High-angle annular dark field STEM image of a cross-section of a N = 10 r-MoS_2 film, with an interlayer spacing of 6.4 Å. (E) GIWAXS data of r-MoS_2, with a peak position of 2-Theta ≈ 14 °, which translates to an interlayer spacing of 6.4 Å in the scattering direction (through-plane).

The r-TMD films possessed long-range crystallinity in-plane and relative lattice rotations at every interlayer interface (Fig. 3.3A). As seen from its electron diffraction pattern in Fig. 3.3B, the monolayer was polycrystalline. Dark-field TEM revealed randomly oriented crystal domains in the monolayer, with grain sizes, $D \sim 1$ μm connected laterally to form a continuous polycrystalline film. Inside the stacked film, the random domain orientations between adjacent monolayers directly led to interlayer rotation at every stacked interface. This can be seen from the TEM diffraction pattern of a layer number N = 10 stacked r-MoS_2 film, which showed a ringed pattern analogous to powder diffraction. This was due to the increase in the number of

diffraction spots that emphasized the random interlayer crystalline orientation along the through-plane direction.

As both the monolayer growth and stacking steps were scalable, the eventual films produced also had large lateral dimensions. This two-step process could generate centimeter-wide films, as shown from the optical images of a monolayer and an N = 10 r-MoS_2 film on fused silica substrates in Fig 3.3C. These films could also be transferred onto a wide range of substrates of choice, from sapphire substrates for through-plane thermal transport measurements, to holey SiN_x/Si TEM grids such that the film itself was suspended. The large-scale uniformity of these films also enabled the precise and reproducible measurements of the films' thermal properties.

As alluded to previously, the interfaces between the monolayers were pristine and well defined, thanks to the etchant-free stacking technique. Figure 3.3D shows a cross-section of a representative r-MoS2 film, taken by our collaborators led by David Muller at Cornell University. The cross-sectional high-angle annular dark field scanning TEM (HAADF-STEM) image of an N = 10 r-MoS_2 film revealed 10 bright, parallel lines representing each constituent MoS_2 monolayer in the film, matching N exactly as targeted. These monolayers in the stack had a uniform interlayer spacing of ~ 6.4 Å, measured via grazing-incidence wide-angle x-ray scattering (Fig. 3.3E). This value was close to the expected value of 6.5 Å for twisted MoS_2 multilayers based on theoretical calculations[4]. As a demonstration of the films' uniformity, we performed cross-sectional STEM on multiple sites of a N = 10 and a N = 20 r-MoS_2 film each (Fig. 3.4). The three images shown here reveal well-defined monolayers, similar to those shown in Fig. 3.3D for each of the sample, despite taking the images at different locations of the sample.

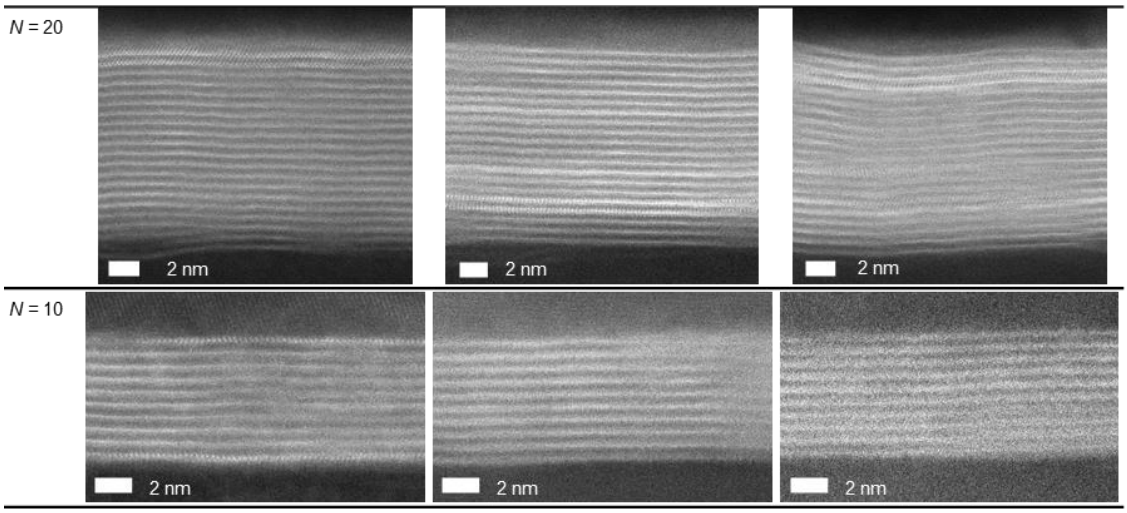

Figure 3.4 Cross-sectional STEM images of N = 20 and 10 r-MoS_2 films. Each set of images from N-thick films was taken from the same sample at different locations.

3.4 Experimental measurements of the through-plane thermal transport properties of r-TMD films

3.4.1 Time-domain thermoreflectance

As discussed in Chapter 2, time-domain thermoreflectance (TDTR) is an optical pump-probe, transient technique that is suited for measuring thermal transport in ultrathin films. The method relies on an Al layer coating the top surface of the sample to act as the transducer layer that reflects the surface temperature. The reflectance of Al depends on its temperature, so measuring the reflection intensity of light and its phase shift under lock-in detection with a photodetector provides the temperature readout.

To perform TDTR, we used a mode-locked Ti:sapphire laser with a pulse repetition rate of 74.86 MHz and a wavelength of 785 nm. The laser light was split into the pump and probe beams, and a mechanical delay stage moved the optical elements along the probe path to delay the probe beam's arrival to the sample. The pump beam was modulated at a frequency of 9.3 MHz so that

the thermoreflectance change at the sample surface could be detected by the probe beam through lock-in detection. The ratio of the in-phase and out-of-phase signals from the lock-in was fitted to a thermal diffusion model, whereby the thermal parameters of the other layers sandwiching the r-TMD film (namely the Al layer and the sapphire substrate) were taken to roughly follow bulk values. The thickness of the Al layer was measured using the picosecond acoustics of the reflected pulse from the Al/r-MoS_2 interfaces (Fig. 3.5). The parameter to fit for was the overall thermal conductance of the film, G, which is the reciprocal of the sum of the Al/r-TMD and r-TMD/Al_2O_3 interfacial thermal resistances as well as the thermal resistance across the r-TMD film itself. The full details of the TDTR measurement can be found elsewhere[5,6]. The TDTR measurements were performed by our collaborators in the David Cahill group at the University of Illinois Urbana-Champaign.

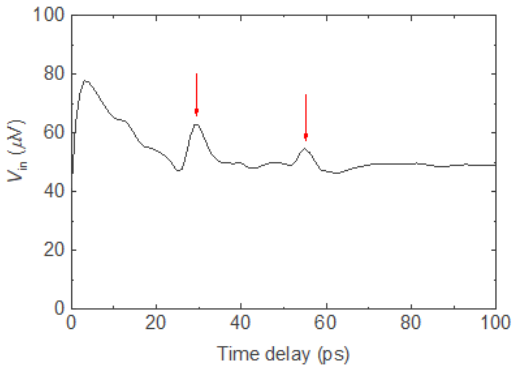

Figure 3.5 Picosecond acoustics of an MOCVD-grown MoS_2 monolayer coated with an Al transducer layer on thick sapphire substrate. The y-axis V_{in} is the in-phase signal of the lock-in amplifier. The red arrows indicate the acoustic waves reflected at the Al/MoS_2 interface.

For the experimental measurement, we deposited via electron-beam deposition an array of ~ 70 nm thick, 90 μm x 90 μm squares on the surface of the r-TMD films that were transferred onto sapphire substrates. The size of the squares was much larger than our film thicknesses (≤ 15 nm) and beam spot sizes ($1/e^2$ radius = 10.7 μm), so the discontinuity of the Al layer did not interfere

with the thermal measurements, and the heat flow from the Al surface was primarily in the through-plane direction. We directed a stream of pump laser pulses to the Al pads to heat up the surface, followed by the Al thermoreflectance readout of the temperature signal via the probe ($-{}^{V_{in}}/_{V_{out}}$). Repeating the pump-probe measurements with varying probe time delays produced a cooling curve corresponding to the heat dissipation from Al to the underlying r-TMD films and eventually to the substrate heat sink.

3.4.2 TDTR Results

The TDTR measurement yielded decay curves that corresponded to the Al surface temperature (Fig. 3.6A). From the three representative cooling curves measured from 1-, 2-, and 10-layer r-MoS_2, we see that the underlying film became more thermally resistive, and the curves flattened as N increased. We fitted the curve to the thermal diffusion model to calculate the overall thermal resistance, R_{TDTR}.

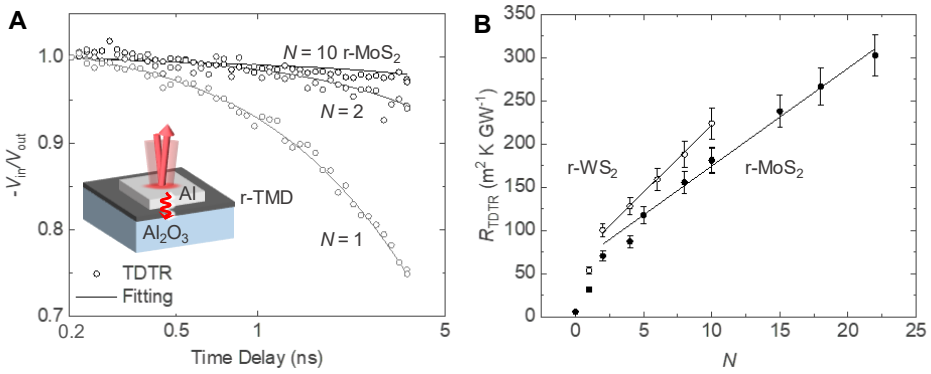

Figure 3.6 TDTR results for the through plane thermal conductivity measurement of r-TMD. (A) Decay curves of r-MoS_2 of various N. Inset: TDTR sample geometry. (B) Fitted R_{TDTR} values for r-WS_2 and r-MoS_2 from the cooling curves in (A).

Given the films' nanoscale thickness (≤ 15 nm), we were unable to separate the effects of the films' top and bottom interfaces from the resistance that's solely due to the r-MoS_2 film itself (the sum of which is R_{TDTR}). However, given the layer number precision for our films' target thicknesses, we could carefully measure the thickness-dependent increases of R_{TDTR}, from which the intrinsic value of $\kappa_\perp$ could be calculated.

Figure 3.6B shows how R_{TDTR} varied with N for our r-MoS_2 and r-WS_2 films, all of which were measured under ambient conditions. The plot has several notable features. Firstly, R_{TDTR} monotonically increases with N. This feature signifies that heat flow in the through-plane direction was diffusive in nature, so that the effect of a thickness increase by even one monolayer had measurable impact on the thermal resistance. This is surprising, given how thin the films were—this contrasted with previous thermal observations in single crystalline MoS_2, through which phonon transport was ballistic in crystals up to 240 nm thick[7]. Even epitaxially grown AlAs/GaAs superlattices had shown coherent phonon transport in films as thick as 216 nm, which meant that their interfaces were perfect and did not scatter phonons[8]. On the other hand, the interfaces between the rotationally misaligned monolayers in our r-TMD films demonstrated the opposite effect.

Another feature of Fig. 3.6B is that R_{TDTR} is linear with respect to N. A uniform slope indicates that a single parameter $\kappa_\perp$ characterizes the through-plane thermal resistance across the r-TMD film for $N \geq 2$, according to the equation $R_{TDTR} = R_0 + {N \cdot d}/{\kappa_\perp}$, whereby d is the monolayer thickness measured via X-ray scattering in Fig. 3.3E (so $N \cdot d$ is the total film thickness) and R_0 is a constant corresponding to the total interface resistance (r-TMD/Al and r-TMD/sapphire). Hence, we can neglect the interfaces in our calculations of κ, simply by looking at the slope.

Applying linear fitting to the data in Fig. 3.6B, we determined $\kappa_\perp$ = 0.057 ± 0.003 W m^{-1} K^{-1} for r-MoS_2 and $\kappa_\perp$ = 0.041 ± 0.003 W m^{-1} K^{-1} for r-WS_2. Notably, these values were similar to the lowest value ever observed in a fully dense solid (disordered nanocrystalline WSe_2 synthesized by Johnson *et al.*[9]) and comparable to that of air at ambient pressures (~ 0.026 W m^{-1} K^{-1}). Despite the clean and well-defined homointerfaces, the measured values of our r-TMD films were also two orders of magnitude smaller than $\kappa_\perp$ of bulk MoS_2 (2-5 W m^{-1} K^{-1}) or WS_2 (~ 3 W m^{-1} K^{-1}). This points to the only difference, interlayer rotation, as the reason for the ultralow $\kappa_\perp$ value in our r-TMD films.

Another evidence for diffusive phonon transport is the weakly positive dependence on the through-plane thermal conductivity with respect to the temperature (Fig. 3.7). This trend resembles that of other amorphous materials. On the other hand, crystalline materials show that κ varies as ~ T^{-1}, due to Umklapp phonon scattering that reduces the mean free path at high temperatures.

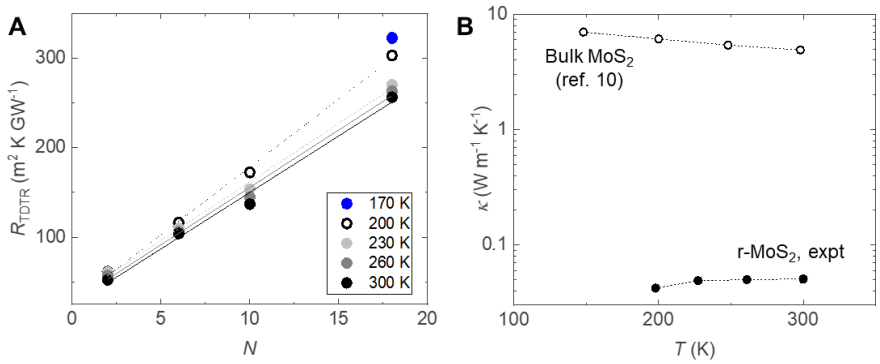

Figure 3.7 Temperature-dependent TDTR on r-MoS_2 films. (A) R_{TDTR} values of r-MoS_2 films with different N, measured at various temperatures. (B) Through-plane κ values of r-MoS_2, as measured from the slope of the linear fit in (A), compared to experimentally measured values for bulk MoS_2 taken from reference [10].

3.5 Experimental measurements of the in-plane thermal transport properties of r-TMD films

3.5.1 Raman thermometry

Raman thermometry is a technique suitable for measuring the in-plane thermal transport of 2D films with signature peaks in their Raman spectra. It makes use of the fact that certain Raman peaks have a strong temperature dependence, which can be calibrated for non-contact temperature readout[11,12].

We used the Raman thermometry to measure the in-plane thermal transport of r-MoS_2 films, assessing the position of the A_{1g} Raman peak to read out local temperature. Our calibration measurements showed that the A_{1g} peak position shifted linearly with temperature, and the magnitude of the slope gives the temperature coefficient χ. This, along with the laser power dissipated by the r-MoS_2, the sample geometry, and appropriate heat sink/boundary conditions let us calculate the value for $\kappa_{||}$. Performing the measurement with a suspended film and at low pressures confined heat flow to within the film in the in-plane direction.

To prepare suspended samples for Raman thermometry, we used the same MOCVD and programmed vacuum stacking technique to synthesize N-layered films. We then suspended the stacked films over 5 μm-diameter holes on SiN_x/Si TEM grids (Fig. 3.8C) before annealing the films under 400/100 SCCM Ar/H_2 at 350 ºC for 3.5 hours to remove the PMMA polymer handling layer.

We conducted our Raman measurements in a Linkam THMS6000 stage (Fig. 3.8A, B). The chamber had been modified to enable low-pressure measurements from ~ 10 Torr to ambient pressures. We used a fixed laser wavelength of 532 nm for all the measurements.

Before the thermal measurement, we first calibrated the A_{1g} peak with respect to the temperature by inducing global heating in the chamber containing the sample, then reading out the peak position ω (Fig. 3.8D). We read out the temperature with the lowest possible laser powers to induce minimal heating to the sample, and that the laser probed only the temperature of the film in equilibrium with its environment. So, the temperature of the film was assumed to be largely uniform, and no net heat flux flowed within. We also performed this measurement in N_2 gas under ambient pressures because the gas helped establish uniform temperatures across the film via air thermal conduction. N_2 also prevented oxidation of the film at higher calibration temperatures of ~ 200 ºC. We noticed that χ did not vary significantly across different samples of similar domain size (D) and different N (Fig. 3.8E). Nevertheless, we performed this temperature calibration prior to thermal measurement for every sample.

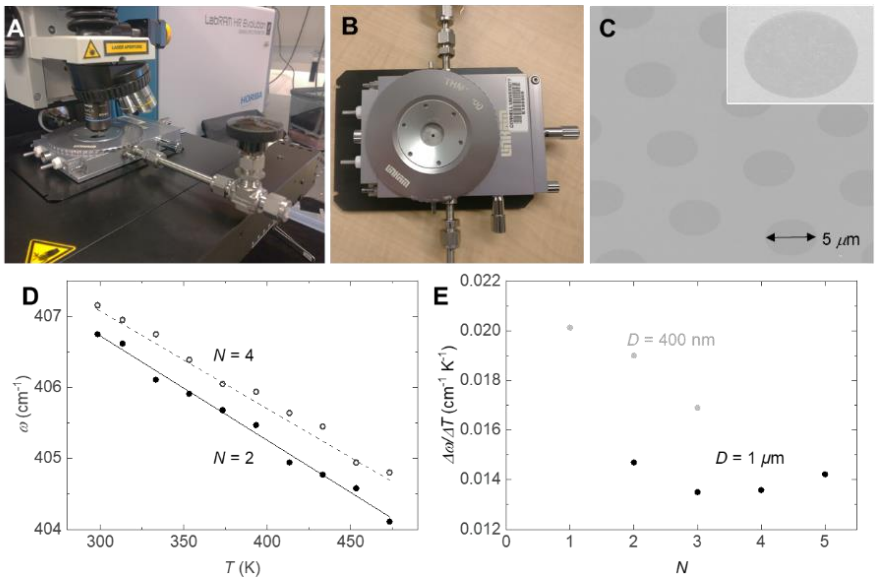

Figure 3.8 Temperature calibration of the r-MoS_2 A_{1g} peak. Side-view (A) and top-view (B) photos of the Linkam stage with a variable stage heating function, modified to be compatible with low pressures. (C) A 45˚ SEM micrograph of a N = 4 r-MoS_2 film suspended on a TEM grid for Raman thermometry. (D) Representative temperature-calibration curves of suspended N = 2, 4 r-MoS_2 films. (E) χ values for r-MoS_2 films with various D and N.

To measure $\kappa_{||}$, a local heating was needed to generate a measurable temperature gradient along the film. To achieve that, we varied the laser power P and recorded the corresponding ω (Fig. 3.9). The laser power absorbed by the film (P_{abs}) increased the local temperature (ΔT), which was reflected in the value of ω that measured the average temperature of the r-MoS_2 in the laser region. The in-plane thermal conductance was obtained from the reciprocal of the slope of the $\Delta\omega$-P linear fit and is denoted by $\left|{}^{d(\Delta\omega)}/_{dP_{abs}}\right|$.

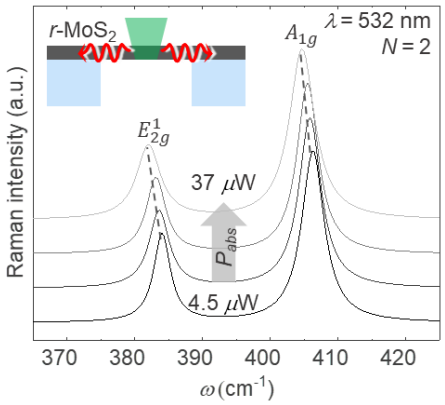

Figure 3.9 Representative Raman spectra of N = 2 r-MoS_2. The peaks redshift with higher laser power due to a local temperature rise. Inset: The Raman thermometry sample geometry.

The $\Delta\omega$-P measurements were conducted at a pressure of 15 Torr to eliminate any heat loss to air. The presence of gas may facilitate thermal equilibration from the laser-heated area to its surroundings. At this low pressure, we confirmed that all heat was confined to conduction through the film. We verified this by repeating the measurements for N = 2 r-MoS_2 films at a lower pressure of 4 mTorr, which gave rise to similar $\Delta\omega$-P values weighted by the beam spot size. On the other hand, the values of $|\Delta\omega|$ were significantly smaller at atmospheric pressure due to the extra heat loss channel by air, so the temperature rise in the film was not as pronounced (Fig. 3.10).

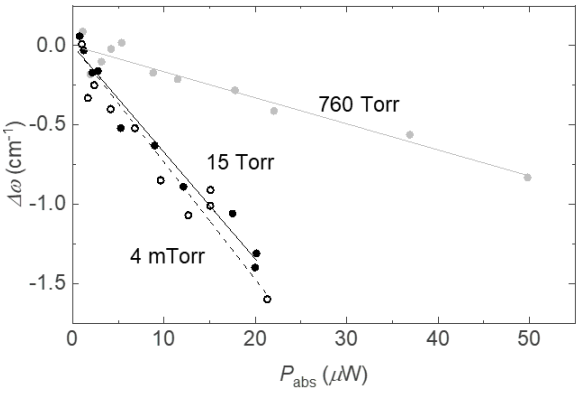

Figure 3.10 Pressure-dependent $\Delta\omega$-P_{abs} measurements of a representative N = 2 r-MoS_2 film obtained via Raman thermometry. The P_{abs} values along the x axis were normalized to account for the slight differences in beam spot sizes (Δr_0 = 20%) due to the different sample chambers to enable the ultralow vacuum measurement. The plot shows that thermal conduction across the film-air boundary is negligible at 15 Torr or less.

A linear slope indicates that $\kappa_{||}$ was roughly constant within the temperature range as induced by the laser. As κ is known to change with temperature in crystalline solids, we kept laser powers below 250 μW to induce a relatively small ΔT in the film and minimize changes in the value of $\kappa_{||}$. Given that the $\Delta\omega$-P slope is roughly linear for our range in laser powers of $P < 250\ \mu W$, we verified that this condition was met. Any higher laser powers caused the $\Delta\omega$-P curve to deviate from the linear regime with $\frac{d^2(\Delta\omega)}{dP^2} < 0$ (Fig. 3.11). In this regime, the local temperature in the film increased faster at higher $P > 250\ \mu W$, which signified that the thermal conductivity could no longer be assumed to be constant. Instead, κ decreased with increasing T, agreeing with what we expect for crystalline solids at high T above their Debye temperatures, and this is indeed consistent with our high laser-power Raman measurements.

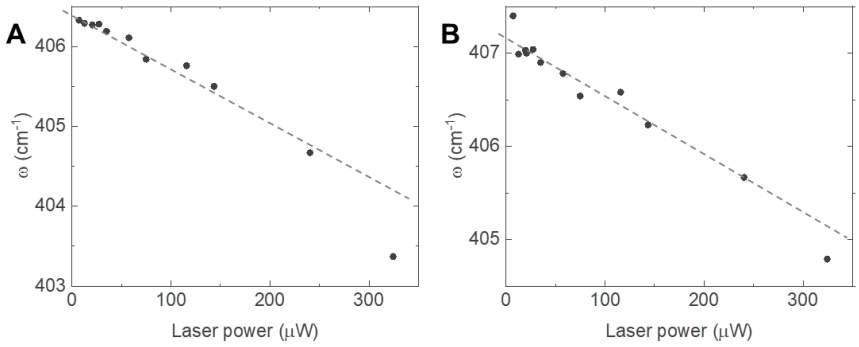

Figure 3.11 ω vs. laser power of a N = 2 (A) and N = 4 (B) r-MoS_2 films measured via Raman thermometry. The data points deviate from a linear trend (indicated by the grey dotted lines) at high laser powers.

Detailed below are all the considerations for every measured parameter involved in the calculation of $\kappa_{||}$ of r-MoS_2.

3.5.1.1 r-MoS_2 absorbed laser power

First, we measured the power of the direct laser using a Thorlabs standard silicon photodiode power sensor. To understand what fraction of this laser power was absorbed by the r-MoS_2 film, we measured absorbance $A = \frac{Absorbed\ light\ intensity}{Incident\ light\ intensity}$ at room temperature on a white-light microscope with a 532 nm band-pass filter and a low numerical condenser aperture. We separately measured the light intensity transmitted through and reflected from a r-MoS_2 film suspended on a TEM grid (Fig. 3.12A, B), then compared it against a blank TEM grid and a silver mirror respectively. The values for A were calculated using the formula $A = 1 - T - R$. We measured $A(N)$ for N = 1-5, then fitted A to the power law $A = 1 - {T_0}^N$ (Fig. 3.12C). Our fit yielded T_0 = 0.92, matching previous reports[3].

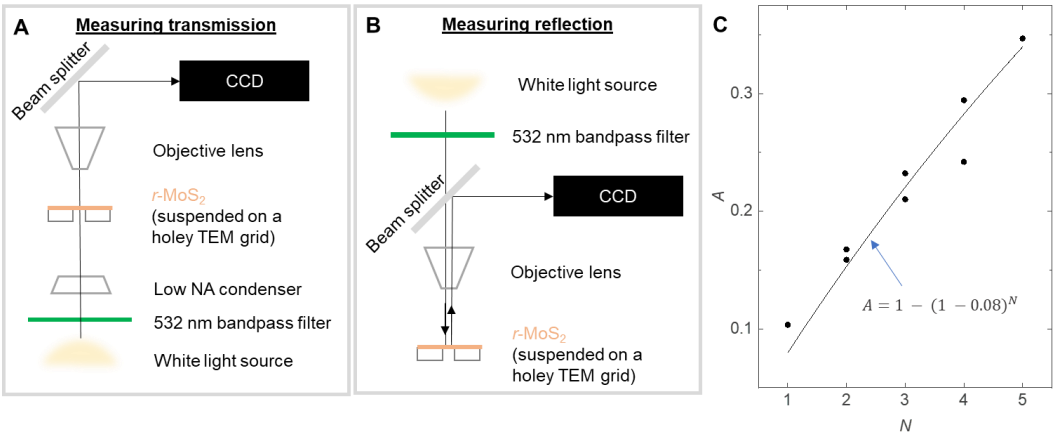

Figure 3.12 Measuring A of r-MoS_2. Measurement setup for the transmission (A) and reflectance (B) of r-MoS_2 suspended on a holey TEM grid with diameters of 5 μm. We calculated the absorbance using the formula $A = 1 - T - R$. (C) A measurements and fitting for r-MoS_2 films with various N.

3.5.1.2 Laser spot size measurements

We used the knife-edge technique to measure the laser beam spot size. We perform a 1D Raman map across a sharp gold step, created using nanofabrication techniques, on a Si wafer (Fig. 3.13A). We tracked the area of the Si Raman peak integrated from the spectral range 510–530 cm^{-1} across the gold edge. The area under the Raman peak can be fitted to an error function, and the slope of the mathematical step is indicative of the laser spot size, which was assumed to be Gaussian (Fig. 3.13C).

Our beam spot size and laser power measurements were performed as closely as possible to the measurement conditions, such as through the glass window viewport of the Linkam stage (0.5 mm thick). The lens used for the measurement (50x, LMPlanFL N) was not equipped with a correction collar that would reduce the spherical aberration to yield a more focused laser spot.

The surface heights of the Si substrate and the r-MoS_2 TEM grids are different. So, it was a challenge to maintain the same focus from the Si substrate on which we measured the laser spot

size to the TEM grids, because the height differences necessitated adjusting the lens height to achieve the same focus after switching between imaging samples. This was the main source of error for the $\kappa_{||}$ measurement. To maintain the focus, we had to use "eyeballing" to recreate the same laser focus on the r-MoS_2 sample after measurement of the beam spot size on the Au-Si sample (Fig. 3.13B). This was assisted by the presence of Airy diffraction patterns as observed under the laser, due to the thin glass window in the viewport positioned between the lens and the r-MoS_2 sample. Although the glass window reduced the focus of the laser, the Airy patterns changed drastically with lens height Δz near the best focus, so we could approximately recreate the beam focus conditions just by observing the Airy patterns.

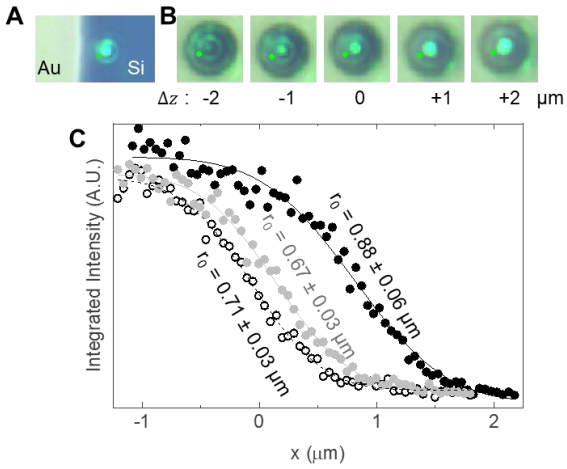

Figure 3.13 Measuring the laser spot size, r_0 using the knife-edge method. (A) Photo of laser spot on a Si substrate next to a 200 nm–high Au step edge. (B) Photos of the laser spot on the surface of a N = 1 r-MoS_2 film suspended on a 5 μm-hole SiN_x/Si TEM grid. The lens height at Δz = 0 was the selected focus for all the Raman measurements, and the other photos show how the Airy patterns of the laser changed with Δz, which was used to reproduce the laser focus across different samples. The small green off-centered dot next to each beam spot is the alignment marker for the Raman instrument software. (C) Mapping of the integrated intensity of the Si Raman peak from 510–520 cm^{-1} across the Au step edge. The uncertainty in r_0 originated from the uncertainty of the fit to an error function.

3.5.2 Thermal conductance results; calculation of $\kappa_{||}$ and errors

We plot $\Delta\omega$ vs P_{abs} for r-MoS_2 films of various N (2-5) in Fig. 3.14. The data points for each N lay along a linear curve, indicating that the thermal conductance was constant and well defined for any given N. This slope of the linear fit decreased in magnitude with higher N, which agreed with the intuition that thermal conductance increases with thicker films. Plotting the slope $\frac{\Delta P_{abs}}{\Delta(\Delta\omega)}$ or the thermal conductance against N once again produced a linear relation, which indicated that $\kappa_{||}$ was well defined and independent of N.

To obtain the value of $\kappa_{||}$, we used the 2D thermal diffusion equation with a radial symmetry, following previous reports of Raman thermometry of 2D films[13–15]. We assumed a Gaussian laser profile $q(r) = \frac{PA}{(\pi {r_0}^2)t}\ exp\left(-\frac{r^2}{{r_0}^2}\right)$. We solved for $\kappa_{||}$ numerically using the following equations:

$$\kappa_{||}\frac{1}{r}\frac{d}{dr}\left(r\frac{dT_{susp}(r)}{dr}\right) + q(r) = 0;\ r\ \leq\ R$$

$$\kappa_{||}\frac{1}{r}\frac{d}{dr}\left(r\frac{dT_{supp}(r)}{dr}\right) - \frac{G}{t}\left[T_{supp}(r) -\ T_a\right] = 0;\ r\ \geq\ R$$

and applied the boundary conditions

$$T_{susp}(R) =\ T_{supp}(R)$$

$$\frac{dT_{susp}}{dr}(R) =\ \frac{dT_{supp}}{dr}(R)$$

where r is the distance from TEM hole center, P is the laser power, t is the film thickness, R is the TEM hole radius, T is the film temperature where $T_{susp}, r \leq R$ and $T_{supp}, r \geq R$, T_a is the ambient temperature, A is the fraction of laser power absorbed by the r-MoS_2 film, and G = 10 MW m^{-2} K^{-1} is the interfacial thermal conductance between r-MoS_2 and SiN_x.

We solved for the expression of $T(r)$ and obtained an expression for the average temperature measured by the Raman shift in the laser spot area

$$T_m = \frac{\int_0^R T(r)\, r \cdot exp\left(-\frac{r^2}{{r_0}^2}\right) dr}{\int_0^R r \cdot exp\left(-\frac{r^2}{{r_0}^2}\right) dr}$$

We substituted the experimentally measured value for the calculated expression of T_m and solved the above equation numerically for $\kappa_{||}$. For the error calculations for $\kappa_{||}$, please refer to the Appendix Section 3.8.3 at the end of this chapter.

We calculated $\kappa_{||}$ for each N, and we obtained the average value of 50 ± 6 W m^{-1} K^{-1} for r-MoS_2 films of D ~ 1 μm. Notably, this value was close to the single crystal MoS_2 value of (35 - 84 W m^{-1} K^{-1}) at room temperature. This implies that $\kappa_{||}$ of these r-MoS_2 films was close to the intrinsic phonon-limited value despite the films being made of polycrystalline monolayers. This result was further supported by our $\Delta\omega$-P_{abs} measurements on continuous r-MoS_2 films with a smaller D ~ 400 nm. The measured value of $\kappa_{||}$ ~ 44 ± 6 W m^{-1} K^{-1} was within the margin of error to that of the D ~ 1 μm films. This suggested that the phonon mean free path is smaller than 400 nm, which is consistent with previous reports[16–20]. Furthermore, the Raman thermometry measurements of r-MoS_2 conducted at different temperatures showed that the in-plane conductance decreased with T. This agreed with the phonon-mediated thermal transport

mechanism in-plane, in contrast to the glass-like thermal conduction along the through-plane direction. This further attested to the long-range crystallinity of the r-MoS_2 films in-plane.

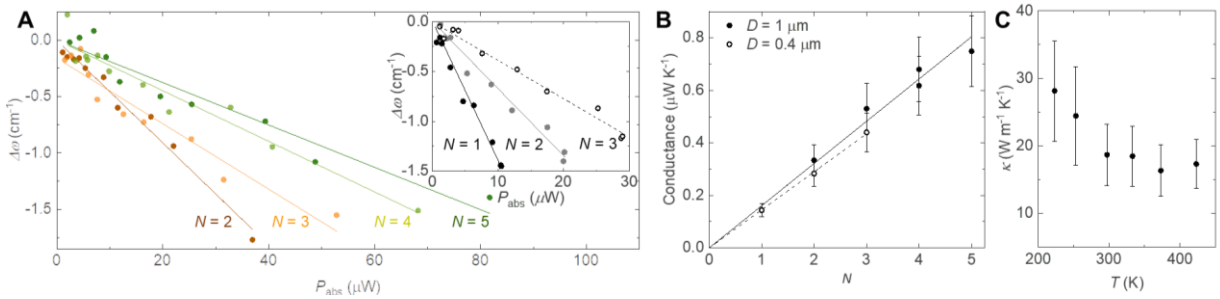

Figure 3.14 Power-dependent Raman measurements for $\kappa_{||}$ calculations. (A) A_{1g} Raman peak shifts vs power absorbed by r-MoS_2 films of various N. Inset: $\Delta\omega$-P_{abs} curves of r-MoS_2 films made from D = 400 nm (grain size) monolayers. (B) Layer-dependent thermal conductance values (absorbed laser power divided by the temperature rise) in D = 1 μm and D = 400 nm r-MoS_2 films. (C) $\kappa_{||}(T)$ of a N = 4 r-MoS_2 film measured using Raman thermometry. (We note that the measured values of $\kappa_{||}$ here were lower than the room-temperature values reported in (B). We ascribe this to the sub-optimal growth conditions for the constituent monolayers used for this sample, which were synthesized specifically for this temperature-dependence measurement.)

3.6 Measured anisotropy

Altogether, our independent thermal measurements in the through-plane and in-plane directions demonstrate that interlayer rotation in r-TMD films resulted in highly direction-dependent thermal conductivity. First, it significantly reduced $\kappa_{\perp}$ while maintaining high $\kappa_{||}$, leading to an ultrahigh value of ρ. We estimated the room-temperature $\rho \sim 880 \pm 110$ for our r-MoS_2 films, which is higher than that of pyrolytic graphite, one of the most anisotropic thermal conductors found in nature ($\rho \approx 340$)[21]. Second, interlayer rotation in r-TMD introduced disorder only along the through-plane direction, affecting almost exclusively the inter-planar force constants while maintaining the intra-planar force constants and the in-plane periodicity. This gave rise to a behavior that can be suitably described as one-dimensional glass-like conduction and

two-dimensional crystal conduction simultaneously realized in a single material. Further evidence of this could be found in the diverging temperature dependence of κ along the through-plane and in-plane directions (Fig. 3.15A), a unique characteristic that has yet to be reported in any material thus far, to the best of our knowledge.

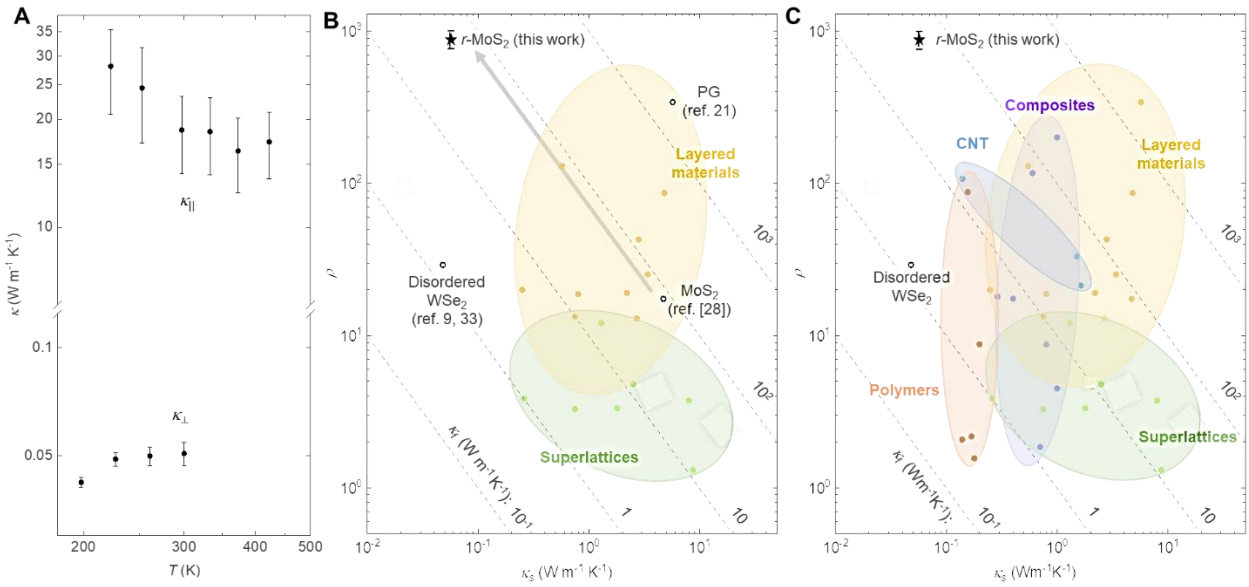

Figure 3.15 Thermal anisotropy in r-MoS_2 films. (A) Different temperature dependences of κ along the in-plane and through-plane directions, compiled from Figs. 3.7B and 3.14C. (B) Anisotropy ratios vs slow-axis thermal conductivity κ_s of thermally anisotropic materials. r-MoS_2 had an ultrahigh thermal anisotropy ratio compared to other materials such as bulk MoS_2, pyrolytic graphite (PG), and disordered layered WSe_2. (C) Full catalogue of experimentally measured ρ values at room temperature vs κ_s of thermally anisotropic materials from literature, by category.

We compared our result with previously reported values of ρ in other phonon-based solids[10,21–32]. We also included the full comparison with all other engineered materials that involve organic and non–phonon-based materials (Fig. 3.15B, C). Compared to a bulk MoS_2 crystal ($\rho \sim 20$)[10] or disordered layered WSe_2 ($\rho \sim 30$)[9,33], r-MoS_2 had a significantly larger ρ because interlayer rotation reduces only $\kappa_\perp$ while leaving the high $\kappa_{||}$ relatively unaffected, as denoted by the gray

arrow parallel to the equi-κ_f (κ in the fast-axis direction) lines. In contrast, previous reports of 2D vdW layered materials with interlayer rotation, such as disordered layered WSe_2 by Johnson *et al.* were able to achieve a similarly low $\kappa_\perp$ as this work[9], but did not retain the TMD material's intrinsically high $\kappa_{||}$ to attain ultrahigh ρ. Moreover, our results suggest that ρ can be even larger if we start with vdW monolayers with a higher $\kappa_{||}$ value, such as graphene, and proceed to use interlayer rotation to generate a similarly low $\kappa_\perp$. A similar 100-fold reduction in $\kappa_\perp$ due to interlayer rotation in few-layer graphene could produce $\rho > 10^4$.

3.7 Conclusion and discussion

Introducing disorder to break the crystallinity of a solid is a powerful and effective way to tune κ. But it is challenging to generate disorder in a directionally controlled way to create extremely anisotropic thermal conductors. Interlayer rotation provides one avenue to generate disorder in vdW layered thin films, as we have demonstrated in this chapter. Moreover, we expect interlayer rotation to be an effective and generalizable way to tune thermal anisotropy in a variety of layered materials. While this work only focused on characterizing r-TMD films assembled from the same monolayer building blocks, this approach can be used to produce engineered vdW superlattices and heterostructures[34] of any arbitrary sequence with highly tailorable ρ, allowing for the customization of thermal properties along any direction with a potentially unprecedented level of spatial control.

From a theory perspective, the impact of interlayer rotation in 2D vdW thin films raises several intriguing questions. How does the complete randomization of atoms along one direction lead to an ultralow thermal conductivity compared to air, despite being a fully dense solid? How does one model disorder in 3D solids that are crystalline along other directions? In the next chapter,

we answered these questions and performed molecular dynamics simulations to understand the mechanism behind r-MoS_2's unique thermal transport properties.

3.8 Appendix

3.8.1 Additional TDTR experiments to gauge film uniformity

To understand the film uniformity for through-plane thermal transport, we performed a 4-by-4 area map of a N = 10 r-MoS_2 film (Fig. 3.16). The mapping locations are indicated by the square array of 16 Al transducer pads covering a large square area (approximately 0.5 mm by 0.5 mm) on a N = 10 r-MoS_2 film. The histogram of R_{TDTR} and our calculations showed that the variation was approximately 4 % of the average, which was consistent with previous observations and confirmed the spatial uniformity of our measurements.

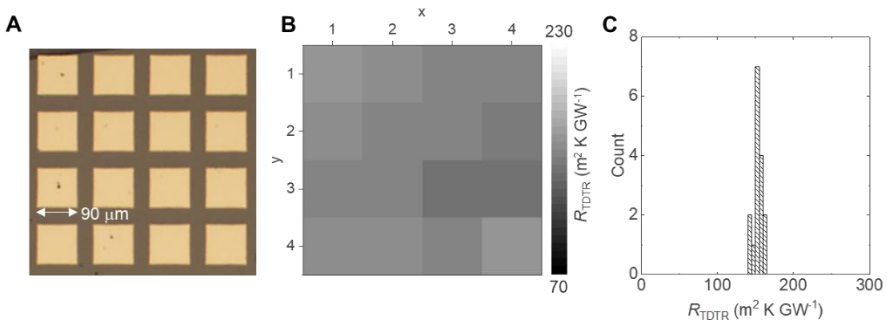

Figure 3.16 Additional TDTR measurements for studying the film uniformity. (A) Microscope image of a N = 10 r-MoS_2 film coated with a square grid of Al pads. (B) 4 x 4 TDTR map of R_{TDTR} of a N = 10 r-MoS_2 film. (C) Histogram of the R_{TDTR} array measurements in (B).

3.8.2 Interface quality of TDTR samples

In our TDTR measurement, we could not separate the different contributions of the films from their top and bottoms interfaces, as our r-TMD films were still relatively thin < 15 nm. Instead, our linear fit method gave the sum of the top Al/r-TMD (R_1) and the bottom TMD/sapphire (R_2)

interfacial resistances, where $R_0 = R_1 + R_2$ was the y-intercept. The values we obtained were 61 ± 7 m^2 K GW^{-1} and 67 ± 3 m^2 K GW^{-1} for r-MoS_2 and r-WS_2 respectively. The sum values we obtained were comparable to those reported in literature (Table 3.1)[7,10,35].

Table 3.1. Comparison of literature thermal boundary resistances with experimentally measured values.

Interface	Thermal boundary resistance (m^2 K GW^{-1})	Reference
Al/MoS_2, R_1	13-30 20-29	A. Sood et al., *Nano Lett.*, 2019 P. Jiang et al., *Adv. Mater.*, 2017
MoS_2/sapphire, R_2	27-53	X. F. Yue et al., *J. Appl. Phys.*, 2020
R_1 + R_2	40-83	
This work (experiment)	61 ± 7 (*r*-MoS_2) 67 ± 3 (*r*-WS_2)	

Our TDTR sample preparation method, such as the choice of metal and the quality of the interface, did not affect the $\kappa_\perp$ that we calculated. As a demonstration, we compared our TDTR results from r-MoS_2 films with Al pads and Au pads as the transducers. We demonstrated that the slopes from the $R_{TDTR}(N)$ plot was similar (Fig. 3.17), indicating the same $\kappa_\perp$ was derived, whereas the y-intercepts were different due to the different interfaces probed (Al/r-MoS_2 vs. Au/r-MoS_2). Comparing the new data from Au with the data with Al confirmed the validity of our approach for determining $\kappa_\perp$.

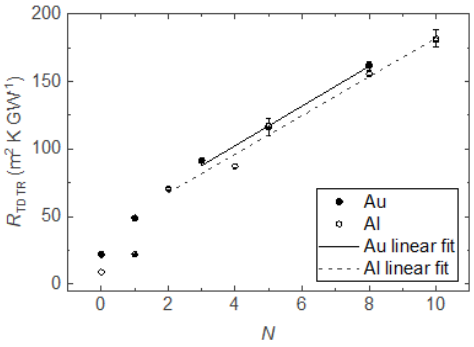

Figure 3.17 TDTR measurements of $N \leq 10$ r-TMD films coated with Au or Al.

3.8.3 Error calculations for Raman thermometry

The total measurement uncertainty of $\kappa_{||}$ was calculated based on the error assessment for individual parameters. We used an approximate analytical solution

$$\Delta T = T_m - T_a \approx -\left(\frac{P_{abs}}{\kappa}\right)\left(\frac{1}{2\,\pi\,r\,t}\right)\ln\left(\frac{R}{r_0}\right)$$

$$\kappa \approx \left(\left(\frac{\Delta\omega}{\Delta P}\right)^{-1}\left(\frac{\Delta\omega}{\Delta T}\right)\right)\left(\frac{A_0}{2\,\pi\,d}\right)\ln\left(\frac{R}{r_0}\right)$$

where A_0 is the absorption of the monolayer. The difference between the full numerical solution and this analytical form was below 3 %[15]. We identified the following independent quantities that carry uncertainty for consideration in our overall uncertainty estimation of $\kappa_{||}$.

(1) $\frac{\Delta P}{\Delta T} = \left(\frac{\Delta\omega}{\Delta P}\right)^{-1}\left(\frac{\Delta\omega}{\Delta T}\right)$: The associated uncertainty was derived from the error in the linear fit of $\left(\frac{\Delta\omega}{\Delta P}\right)$ and $\left(\frac{\Delta\omega}{\Delta T}\right)$ for every sample measured. The total uncertainty in the average $\frac{\Delta P}{\Delta T}$ value was 9 % for D ~ 1 μm films and 8 % for D ~ 400 nm films.

(2) $\left(\frac{A_0}{2\,\pi\,d_0}\right)$: The uncertainty in A_0 from the $A(N)$ fit was 4 %.

(3) ln $(\frac{R}{r_0})$: The uncertainty originated from the uncertainty in r_0. From 14 repeated measurements of the beam spot size using the knife-edge method (Section 3.5.1.2), we calculated the standard deviation of r_0 to be 12 %, which translated to an uncertainty in the expression of ln $(\frac{R}{r_0})$ to be 9 %.

Total uncertainty in $\kappa_{||}$: 13 % (for both D ~ 1 μm and D ~ 400 nm films)

3.8.4 Interfacial thermal conductance between the supported r-MoS_2 film and SiN_x on the TEM grid for Raman thermometry

From other similar Raman thermometry measurements of MoS_2 on SiN_x/Si TEM grids in literature, we referenced the interfacial thermal conductance value, G, to be 10 MW m^{-2} K^{-1}.[36] However, we note that the $\kappa_{||}$ calculations were largely insensitive to the value of G within the range of 1–1000 MW m^{-2} K^{-1}, and the variation in $\kappa_{||}$ lay around 5 %. Further evidence of this can be seen from the theoretical temperature distribution calculations with various hypothetical G values in Fig. 3.18. The temperature profile of the film near the laser spot is largely indistinguishable for the region $x \leq 1$ μm.

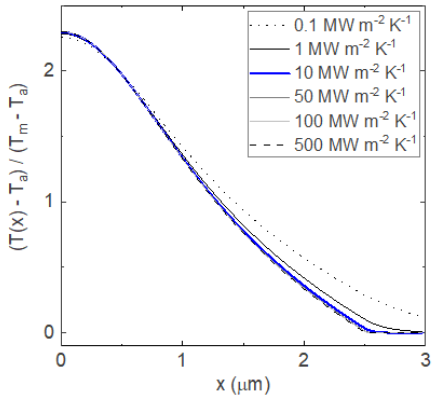

Figure 3.18 Calculated and normalized temperature distribution of the laser-heated N = 2 r-MoS_2 film away from the center of the laser spot. The temperature distribution is largely insensitive to the r-MoS_2/SiN_x interfacial thermal conductance. The value of 10 MW m^{-2} K^{-1} is what was used in our $\kappa_{||}$ calculations.

3.9 References

1. Kim, S. E. *et al.* Extremely anisotropic van der Waals thermal conductors. *Nature 2021 597:7878* **597**, 660–665 (2021).

2. Kang, K. *et al.* High-mobility three-atom-thick semiconducting films with wafer-scale homogeneity. *Nature* **520**, 656–660 (2015).

3. Kang, K. *et al.* Layer-by-layer assembly of two-dimensional materials into wafer-scale heterostructures. *Nature* **550**, 229 (2017).

4. Liu, K. *et al.* Evolution of interlayer coupling in twisted molybdenum disulfide bilayers. *Nature Communications* **5**, (2014).

5. Cahill, D. G. Analysis of heat flow in layered structures for time-domain thermoreflectance. *Review of Scientific Instruments* **75**, 5119–5122 (2004).

6. Liu, J. *et al.* Simultaneous measurement of thermal conductivity and heat capacity of bulk and thin film materials using frequency-dependent transient thermoreflectance method. *Review of Scientific Instruments* **84**, 034902 (2013).

7. Sood, A. *et al.* Quasi-Ballistic Thermal Transport Across MoS2 Thin Films. *Nano Letters* **19**, 2434–2442 (2019).

8. Luckyanova, M. N. *et al.* Coherent Phonon Heat Conduction in Superlattices. *Science (1979)* **338**, 932–939 (2012).

9. Chiritescu, C. *et al.* Ultralow Thermal Conductivity in Disordered, Layered WSe2 Crystals. *Science (1979)* **315**, 351–353 (2007).

10. Jiang, P., Qian, X., Gu, X. & Yang, R. Probing Anisotropic Thermal Conductivity of Transition Metal Dichalcogenides MX2 (M = Mo, W and X = S, Se) using Time-Domain Thermoreflectance. *Advanced Materials* **2**, 1701068 (2017).

11. Balandin, A. A. *et al.* Superior thermal conductivity of single-layer graphene. *Nano Letters* **8**, 902–907 (2008).

12. Calizo, I., Balandin, A. A., Bao, W., Miao, F. & Lau, C. N. Temperature dependence of the raman spectra of graphene and graphene multilayers. *Nano Letters* **7**, 2645–2649 (2007).

13. Yan, R. *et al.* Thermal conductivity of monolayer molybdenum disulfide obtained from temperature-dependent Raman spectroscopy. *ACS Nano* **8**, 986–993 (2014).

14. Lee, J. U., Yoon, D., Kim, H., Lee, S. W. & Cheong, H. Thermal conductivity of suspended pristine graphene measured by Raman spectroscopy. *Physical Review B - Condensed Matter and Materials Physics* **83**, 81419 (2011).

15. Cai, W. *et al.* Thermal transport in suspended and supported monolayer graphene grown by chemical vapor deposition. *Nano Letters* **10**, 1645–1651 (2010).

16. Li, Z. *et al.* Size Dependence and Ballistic Limits of Thermal Transport in Anisotropic Layered Two-Dimensional Materials. *Preprint at arXiv* (2017) doi:10.48550/arxiv.1711.02772.

17. Jo, I., Pettes, M. T., Ou, E., Wu, W. & Shi, L. Basal-plane thermal conductivity of few-layer molybdenum disulfide. *Applied Physics Letters* **104**, 201902 (2014).

18. Lindroth, D. O. & Erhart, P. Thermal transport in van der Waals solids from first-principles calculations. *PHYSICAL REVIEW B* **94**, 115205 (2016).

19. Wei, X. *et al.* Phonon thermal conductivity of monolayer MoS2 : A comparison with single layer graphene. *Appl. Phys. Lett* **105**, 103902 (2014).

20. Cai, Y., Lan, J., Zhang, G. & Zhang, Y. W. Lattice vibrational modes and phonon thermal conductivity of monolayer MoS 2. *Physical Review B - Condensed Matter and Materials Physics* **89**, 035438 (2014).

21. Ho, C. Y., Powell, R. W. & Liley, P. E. Thermal Conductivity of the Elements . *Journal of Physical and Chemical Reference Data* **1**, 279 (1972).

22. Jiang, P., Qian, X., Yang, R. & Lindsay, L. Anisotropic thermal transport in bulk hexagonal boron nitride. *Physical Review Materials* **2**, 64005 (2018).

23. Jang, H., Wood, J. D., Ryder, C. R., Hersam, M. C. & Cahill, D. G. Anisotropic Thermal Conductivity of Exfoliated Black Phosphorus. *Advanced Materials* **27**, 8017–8022 (2015).

24. Luckyanova, M. N. *et al.* Anisotropy of the thermal conductivity in GaAs/AlAs superlattices. *Nano Letters* **13**, 3973–3977 (2013).

25. Mavrokefalos, A., Nguyen, N. T., Pettes, M. T., Johnson, D. C. & Shi, L. In-plane thermal conductivity of disordered layered W Se2 and (W)x (W Se2) y superlattice films. *Applied Physics Letters* **91**, 171912 (2007).

26. Zhou, Y. *et al.* Direct Synthesis of Large-Scale WTe_2 Thin Films with Low Thermal Conductivity. *Advanced Functional Materials* **27**, 1605928 (2017).

27. Lee, W. Y. *et al.* Anisotropic temperature-dependent thermal conductivity by an Al2O3 interlayer in Al2O3/ZnO superlattice films. *Nanotechnology* **28**, 105401 (2017).

28. Aksamija, Z. & Knezevic, I. Thermal conductivity of Si 1−x Ge x /Si 1− y Ge y superlattices: Competition between interfacial and internal scattering. *PHYSICAL REVIEW B* **88**, 155318 (2013).

29. Liu, W. L., Borca-Tasciuc, T., Chen, G., Liu, J. L. & Wang, K. L. Anisotropic Thermal Conductivity of Ge Quantum-Dot and Symmetrically Strained Si/Ge Superlattices. *Journal of Nanoscience and Nanotechnology* **1**, 39–42 (2001).

30. Yang, B., Liu, W. L., Liu, J. L., Wang, K. L. & Chen, G. Measurements of anisotropic thermoelectric properties in superlattices. *Appl. Phys. Lett* **81**, 3588 (2002).

31. Medvedev, V. V. *et al.* Anisotropy of heat conduction in Mo/Si multilayers. *Journal of Applied Physics* **118**, (2015).

32. Jang, H., Ryder, C. R., Wood, J. D., Hersam, M. C. & Cahill, D. G. 3D Anisotropic Thermal Conductivity of Exfoliated Rhenium Disulfide. *Advanced Materials* **29**, 1700650 (2017).

33. Zhu, G. *et al.* Tuning thermal conductivity in molybdenum disulfide by electrochemical intercalation. *Nature Communications* **7**, (2016).

34. Vaziri, S. *et al.* Ultrahigh thermal isolation across heterogeneously layered two-dimensional materials. *Science Advances* **5**, 1325–1341 (2019).

35. Yue, X. F. *et al.* Measurement of interfacial thermal conductance of few-layer MoS2 supported on different substrates using Raman spectroscopy. *Journal of Applied Physics* **127**, 104301 (2020).

36. Yalon, E. *et al.* Temperature-Dependent Thermal Boundary Conductance of Monolayer MoS2 by Raman Thermometry. *ACS Applied Materials and Interfaces* **9**, 43013–43020 (2017).

CHAPTER 4: THE ORIGINS AND POTENTIAL APPLICATIONS OF ULTRAHIGH THERMAL ANISOTROPY IN 2D VDW FILMS

4.1 Introduction

The understanding of thermal transport in solids is challenging. Experimentally measured thermal conductivity is a single value that overwrites all the nuances of the individual phonon modes involved as suggested by theory. Accurately describing the thermal transport in solids using theory requires knowledge of the crystal structure of the solids and the phonon interactions.

The theory of thermal conduction usually starts with describing the phonon dispersion of the solid from the solid. On top of that, the scattering rates of phonons need to be accounted for. Molecular dynamics (MD) is one way to describe heat conduction in solids with arbitrary structures, dictated only by the interatomic potential. For this reason, we chose MD as our technique of choice for studying the microscopic origins of thermal transport in r-TMD films. One challenged we faced was that we had to employ large supercells to capture the disordered and random nature of the films that ran only along the through-plane direction. This chapter details our MD simulations and the results, as well as the experimental observations that support some of the findings. The results here were primarily based on our publication in *Nature*[1], and the MD simulations were performed by our collaborators from Chalmers University in Sweden.

In this chapter, we also discuss the applicability of r-TMD films as heat spreaders for nanoelectronics. We highlight the strength of anisotropy for thermal management and include auxiliary advantages of our film, such as its integrability with delicate nanoelectrodes. We

accompany our demonstration of r-MoS_2's efficacy as heat spreaders with finite-element simulations.

4.2 Atomistic simulations of r-MoS_2

We applied MD simulations to generate atomistic structures of bulk and r-MoS_2. We used an algorithm described in Hermann 2012[2] and implemented it in Python using the atomic simulation environment software package[3]. Our r-MoS_2 model was made from 10 layers with a total of 10,152 atoms (Appendix, Fig. 4.8A). To make the model more tractable, we simulated the sheets in 5 pairs, where each pair was related by a 60 º rotation. The four primitive angles between the 5 pairs were 16.1, 25.28, 34.72, and 43.9 º. All these 10 monolayers with five different orientations were then distributed randomly throughout the stack. In the fully relaxed structure, the average interlayer distance was 6.33 Å corresponding to an increase of 3.5 % relative to the ideal bulk structure (6.09 Å). The value was also comparable to our experimentally measured value of 6.4 Å using GIWAXS (Fig. 3.3E) as well as other theoretical predictions of the increase in layer spacing obtained from first-principles calculations in previous studies[4,5].
Further details of the MD simulations are documented in Appendix 4.5.1.

4.2.1 1D glass-like transport, 2D phonon transport

Our MD simulations closely reproduced the experimentally measured $\kappa_\perp$ and $\kappa_{||}$ values. We plot $\kappa(T)$ in Fig. 4.1. The MD simulations reproduced two main effects of interlayer rotations on $\kappa_\perp$ seen in our TDTR experiments: suppressing $\kappa_\perp$ and altering its temperature dependence from the bulk. The calculated value for $\kappa_\perp$ dropped by a factor of approximately 30, from 4.3 ± 0.2 W m^{-1} K^{-1} in bulk MoS_2 to 0.15 ± 0.1 W m^{-1} K-1 in r-MoS_2 at 300K. The value for $\kappa_\perp$ of r-MoS_2 did not decrease with T, suggesting a transition away from phonon-meditated thermal transport

observed in bulk MoS_2 to glass-like thermal conduction in crystals with interlayer rotation. In contrast, our MD simulations predicted that $\kappa_{||}$ remained high in r-MoS_2 with only a modest reduction of less than a factor of two compared to the ideal bulk crystal. The $\kappa_{||}$ curve also exhibited a temperature dependence consistent with the phonon-limited transport mechanism. This was indeed what we also observed in our Raman thermometry experiments.

The calculated values for $\kappa_{\perp}$ were still a little higher than the experimental values. Contributing to the discrepancy might had been that the simulations were based on an empirical potential that had not been explicitly optimized for the structures considered. Moreover, the average interlayer spacing at 300 K was 6.33 Å for the r-MoS_2 model according to our simulations, slightly smaller than the value of 6.4 Å observed experimentally. The smaller value in the simulations was consistent with a slightly stronger coupling and a slightly larger $\kappa_{\perp}$. In other previous modelling studies, an increase in interlayer spacing of less than 4 % could affect $\kappa_{\perp}$ in layered crystals by an order of magnitude[4]. Furthermore, we can also attribute the discrepancy to our neglect of any quantum effects and all boundary scattering in our simulations, which could potentially further suppress the simulated value of $\kappa_{\perp}$.

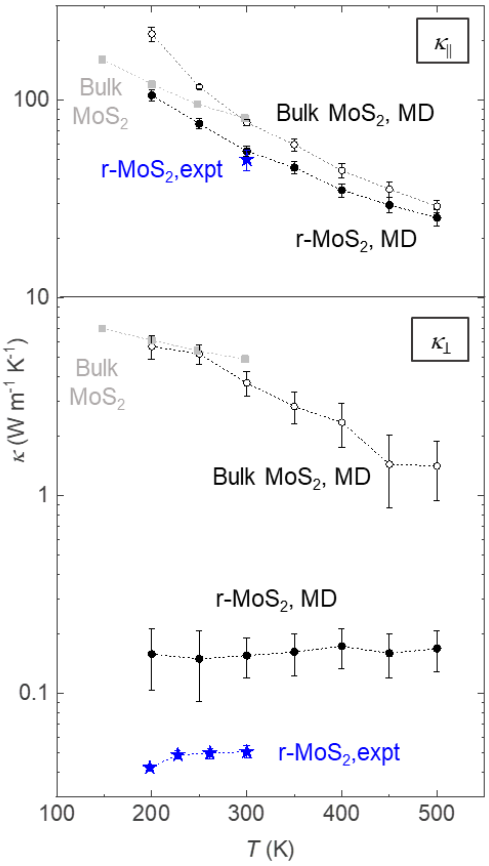

Figure 4.1 Experimental and MD simulation results of $\kappa(T)$ of MoS_2 films. The experimentally measured bulk MoS_2 values were taken from reference [9]. The experimental values for r-MoS_2 also appeared in Fig. 3.7B.

4.2.2 Phonon dispersion

To understand the microscopic origins of suppressed $\kappa_{\perp}$, we analyzed the vibrational spectrum of r-MoS_2 to break down the reduction in $\kappa_{\perp}$ in terms of the changes to the group velocity (v_g) and lifetime (τ), two factors that determine the thermal conductivity according to Boltzmann transport theory.

We first generated the bulk MoS_2 phonon dispersion in the harmonic limit to be used as a reference to phonon dispersion calculations using MD simulations. We computed the harmonic (0 K) phonon dispersion using the PHONOPY package[7], and then computed the forces for

6×6×2 supercells using the LAMMPS code. We used the lowest applicable order of perturbation theory of the PHONO3PY package[8] to compute τ, allowing us to solve for the thermal conductivity using the Boltzmann transport equation[9]. Comparing this MD simulated phonon dispersion of bulk MoS_2 to reports elsewhere allowed us to verify the accuracy of our method to obtain the phonon dispersion of r-MoS_2.

For both bulk and r-MoS_2, we extracted the phonon dispersions and lifetimes at 300 K by analysing the longitudinal and transverse velocity current correlation functions generated by MD simulations in the NVE ensemble using dynasor[10]. The MD simulations details were otherwise identical to the HNEMD simulations. The obtained correlation functions were Fourier transformed and fitted to peak shape functions corresponding to (over)damped harmonic oscillators to obtain the phonon frequencies and lifetimes.

Analysis of the individual branches in the phonon dispersion in Fig. 4.2A yielded several notable features. The v_g of the longitudinal acoustic (LA) mode in r-MoS_2 remained similar to that of bulk MoS_2. On the other hand, the through-plane transverse acoustic (TA) modes in r-MoS_2 underwent extreme softening with their group velocities practically vanishing, as seen from the flattening of the dispersion curve. A non-existent TA group velocity also implied a loss of resistance with respect to lateral shear.

This was consistent with the experimentally measured, low-frequency Raman spectra of N = 2, 3, and 4 r-MoS_2 films. From the layer-dependence of the peak positions, we assigned these to be the breathing modes of MoS_2[11]. With interlayer rotation, the film exhibited no measurable shear vibrational peaks, whereas the breathing mode peaks were intact and roughly matched the positions for exfoliated few layer MoS_2 as reported in literature (Fig. 4.2B, C)[11,12]. Our findings

agree with theoretical studies of low-frequency Raman modes of twisted MoS_2 bilayers, which showed that the shear mode peaks redshift to below the detection capabilities (2 cm^{-1})[13]. Our low-frequency Raman results agreed with our MD simulations that suggested that the transverse vibrational mode in r-MoS_2 was suppressed by interlayer rotation, while the longitudinal vibrational mode was retained.

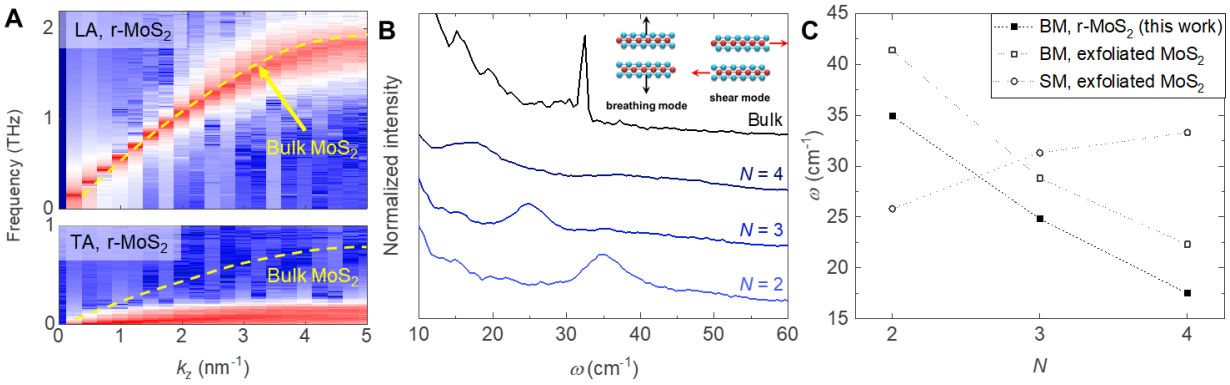

Figure 4.2 Vibrational modes of r-MoS_2. (A) LA and TA phonon dispersion curves of r-MoS_2 along the Γ-A direction. The dotted lines denote the acoustic curves corresponding to bulk MoS_2. (B) Raman spectra reflecting the breathing modes of r-MoS_2 and the shear mode for bulk MoS_2. (C) The low-frequency Raman peak positions of r-MoS_2 and exfoliated MoS_2. The filled squares indicate the breathing mode peak positions of r-MoS_2. The open squares indicate the breathing mode peak positions of exfoliated MoS_2, taken from reference [14]. The open circles indicate the shear mode peak positions of exfoliated MoS_2, also taken from reference [14].

In Fig. 4.3E, we plot τ for the LA and TA vibrational modes, which were extracted from fitting the current correlation functions to a damped harmonic oscillator model (Fig. 4.3A-D). Specifically, the correlation functions were fitted to $C(\omega) = A2\Gamma\omega^2 / [(\omega^2 - \omega_0^2)^2 + (\Gamma\omega)^2]$, where A, Γ and ω_0 are the fitting parameters corresponding to the prefactor, phonon lifetime ($\tau = 2/\Gamma$), and phonon frequency respectively. The plot shows that τ of both the LA and TA modes in r-MoS_2 were more than one order of magnitude smaller than in bulk MoS_2. The LA lifetimes were close to the period of the LA mode vibration (dashed line, extracted from Fig.

4.3E), indicating strongly overdamped behavior. From these results, the median mean free path $\tilde{\lambda} = v_g\tau$ for the LA modes was estimated to be 2 nm, suggesting that the heat-carrying LA modes were strongly scattered, even though the r-MoS_2 films were of nanoscale thicknesses.

In summary, we concluded that the strongly suppressed TA modes that led to a loss of resistance to lateral shear and the overdamping of the dominant heat carrying LA modes resulted in extremely inefficient thermal transport along the through-plane direction in r-MoS_2. Along with the very weak temperature dependence, this result pointed towards a glass-like conduction mechanism.

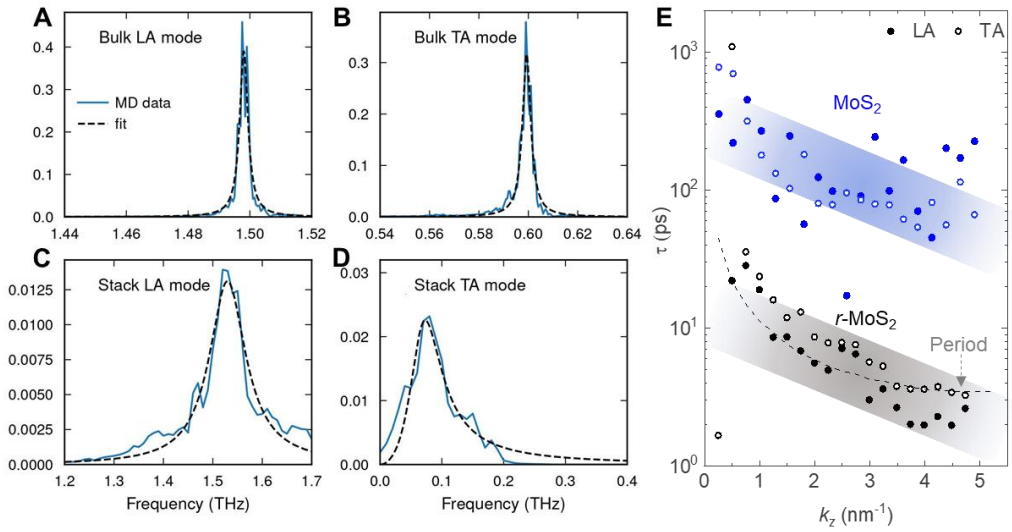

Figure 4.3 Extracting the phonon lifetimes of r-MoS_2 from the MD simulations. Current correlation functions at 300 K for the (a) longitudinal acoustic (LA) and (b) transverse acoustic (TA) modes in bulk MoS_2 as well as the (c) LA and (d) TA modes in r-MoS_2. The k-points shown here are $|k_z| =$ 3.3535 nm^{-1} for bulk MoS_2 and $|k_z|$ = 3.2389 nm^{-1} for the N = 10 model of r-MoS_2. (E) Lifetime of the LA and TA phonons parallel to the Γ-A direction in bulk and r-MoS_2. The dashed line is the LA mode vibration period derived from the dispersion curve in Fig. 4.3A.

4.3 Demonstration of a practical application of thermal anisotropy: Ultrathin heat spreaders

4.3.1 Introduction to heat spreaders for electronics

Here, we demonstrate the use of r-MoS_2 as passive heat spreaders to reduce the likelihood of electromigration failure in nanoelectronics. Electromigration is a phenomenon that occurs at high current levels, when the collision of electrons drifting under the influence of an electric potential imparts momentum to the lattice and causes a gradual diffusion of atoms. This phenomenon can cause device failure by breaking electrical interconnects as atoms inside the current-carrying electrical pathways migrate. It is qualitatively described using Black's equation,

$$Mean\ time\ to\ failure = \frac{A}{J^n}\ e^{E_a/k_BT}$$

where A is a proportionality factor, J is the current density, E_a is the activation energy for diffusion, n is a scaling factor, and T is the temperature in Kelvins. As seen from the equation, one strategy to reduce electromigration failure is to maintain a low T. Standard on-chip thermal management strategies employed in modern-day devices include passive cooling using heat sinks, spreaders, and phase change materials; and/or active cooling technologies such as forced convection cooling and micro-thermoelectric coolers[14,15]. As electronics miniaturize, some of these thermal strategies may hinder keeping up with a device's portable function. As such, an increase in the reliance on passive cooling methods on chip—especially heat spreaders—is necessary to reduce the amount of material in the device, such that lightness of the device can be maintained. Moreover, heat spreaders are arguably the simplest method, requiring the least construction material, and can make use of the device chassis as the heat sink. Typical heat spreaders can be strips of metal with good thermal conductivity. We make the case for an anisotropic heat spreader such as r-MoS_2 in the following sections.

4.3.2 Fabrication of an ultrathin r-MoS_2 heat spreader film for Au nanoelectrodes

To demonstrate the utility of r-MoS_2 as heat spreaders, we fabricated nanoscale Au electrodes, onto which we would drape our MoS_2 film. All Au electrodes were fabricated on Si substrates with 50 nm dry SiO_2 in three nanopatterning and deposition layers: (A) the nanoelectrodes (10 μm long, 100 nm wide, 15 nm thick), (B) the contact pads which would interface with the external electronics (200 μm long, 300 μm wide, 100 nm thick), and (C) the leads connecting the nanoelectrodes and the contact pads (~ 1000 μm long, 50 μm wide, 15 nm thick). The nanoelectrodes, being the thinnest junctions, would be the site where electromigration failure was most likely to occur.

We first defined the leads (C) and then the contact pads (B) using standard photolithography, followed by the electron-beam evaporation of Ti (1nm)/Au, and then lift-off. The final step was our defining of the nanoelectrodes (A) using electron-beam lithography (a bilayer of resists: copolymer P(MMA-MAA 11%) in ethyl lactate and 950K PMMA A4; writing: Raith EBPG 5000 Plus E-beam Writer with the beam conditions of 25 nA current, a dose of 1200 mC/cm^2, 300 mm aperture size, 100 kV), deposition of 15 nm Au, and lift-off. Notably, we did not deposit any Ti as the adhesion layer for our Au electrodes.

After the fabrication of the nanoelectrodes, leads, and pads, the device was cleaned with an O_2 plasma for 30 s to remove any resist residue and to promote adhesion of the r-MoS_2 film to the Au electrodes and the SiO_2 surface during the film transfer step. A PMMA-coated, N = 16 r-MoS_2 film (10 nm thick) was transferred onto the electrodes using the programmed vacuum stacking method. The PMMA on the r-MoS_2 film was removed by immersing the entire chip in a toluene bath at 60 ºC for 1 hour.

All measurements were performed under ambient conditions with a two-probe geometry on a home-built probe station. To measure the critical current threshold I_c at which the Au electrode failed, we swept the voltage bias in only one direction at a rate such that the rate in current increase is 0.05 mA per 20 s.

For comparison, we deposited SiN_x onto Au electrodes (10 μm long, 10 nm thick, 100 nm wide) using plasma-enhanced chemical vapor deposition with the following conditions: 10 s deposition at 90 ºC and 10 Torr and 1000 W plasma power, with 25 SCCM/35 SCCM SiH_4/N_2 as the precursors. The film thickness was measured via ellipsometry to be 16 nm.

4.3.3 Critical current measurements

Both the bare and coated Au electrodes showed similar electrical resistance R at low currents. This showed that the r-MoS_2 film could be integrated with the Au electrodes using mild conditions that did not affect the electrodes' electrical properties. This non-destructive processing conditions of r-TMD film integration posed an advantage compared to the deposition of other electrically insulating materials with a comparable κ, such as SiN_x. The preparation of a SiN_x film using plasma-enhanced chemical vapor deposition negatively affected the performance of the Au nanoelectrodes and increased their electrical resistances (Fig. 4.4A).

At higher currents, current-induced Joule heating leads to the thermally activated electromigration process which causes the electrodes to fail[16]. Comparing the representative I-V curves measured from a bare and coated Au electrode, we showed that the Au electrode covered with r-MoS_2 could carry a larger current before reaching electromigration failure (Fig. 4.4B). The histogram of critical current I_c (the maximum current a Au electrode could sustain for at least 20 s without failing) measured from 20 electrodes (10 bare and 10 covered with r-MoS_2) revealed a ~ 50% increase in the median I_c values (Fig. 4.4C). These results demonstrated our

r-MoS_2 film's ability to efficiently dissipate Joule heat and keep the electrodes cool. As the electromigration process is dominated by the temperature, the observed increase in I_c and the maximum electrical power before breaking were in good agreement with our finite-element simulations results, which we detail in the next section.

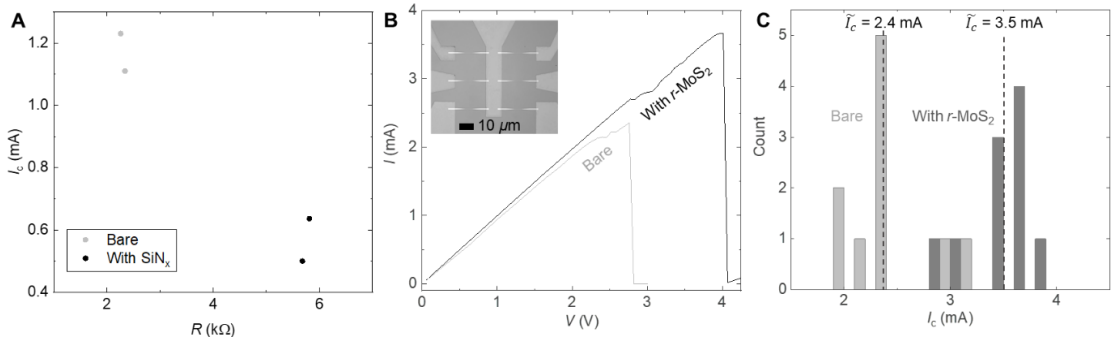

Figure 4.4 Demonstration of the efficacy of r-MoS_2 to act as a heat spreader for Au nanoelectrodes. (A) Electrical resistances R of Au nanoelectrodes before and after the deposition of SiN_x as heat spreaders. (B) The I-V curve of an Au electrode, with and without N = 16 r-MoS_2. Inset: Optical micrographs of six fabricated Au electrodes, connected to the thicker and larger area contact pads. (C) Histogram of I_c of Au electrodes with and without a N = 16 r-MoS_2 heat spreader and their median values.

4.3.4 Finite-element analysis of r-MoS_2 as heat spreaders

To understand the impact on the temperature distribution of r-MoS_2 as a heat spreader, we performed finite-element simulations and showed that the extreme anisotropy of our r-MoS_2 films can lead to excellent heat dissipation in-plane from a heat source and drastic thermal insulation through-plane. Using the COMSOL Multiphysics software, we created a virtual geometry of a 10 nm-thick r-MoS_2 film draped over a nanoscale Au electrode (15 nm tall, 100 nm wide) on a 50 nm SiO_2/Si substrate (Fig. 4.5A). For the thermal anisotropy consideration, we defined the thermal conductivity slow-axis direction to always be perpendicular to the film surface, including when it was draped over the Au electrode side walls. We supplied the Au

electrode with a heat source of 8 mW uniformly over the entire volume, matching the power conditions at which the bare Au electrodes failed in our experiments. As the boundary condition, we set the bottom surface on the Si substrate to be at 293.15 K. We also accounted for the interfacial thermal resistances between all the heterogeneous surfaces in our calculations, which include r-MoS_2/Au, r-MoS_2/SiO_2, Au/SiO_2, SiO_2/Si obtained from literature[17–20]. All the effects of radiation were neglected as they did not affect the temperature values in our simulations. We also neglected any heat loss to air.

Our simulation results showed that for a fixed power of 8 mW supplied to the Au, the temperature rise ΔT of the Au electrode covered by r-MoS_2 was 50 K lower than that of the bare electrode, thereby demonstrating our film's effectiveness at spreading heat due to its excellent $\kappa_{||}$ (Fig 4.5C). Interestingly, our r-MoS_2 films provided significant thermal insulation in the through-plane direction (Fig. 4.5B), with much lower MoS_2-surface ΔT values that were only a third of the value of the bare Au electrode (Fig. 4.5C).

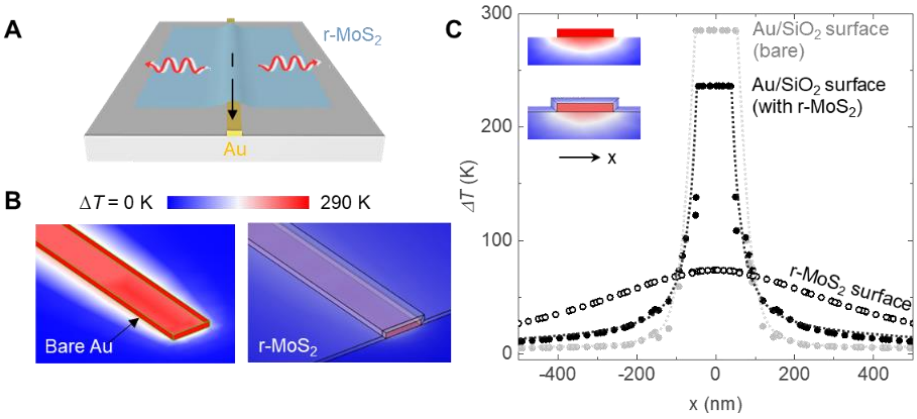

Figure 4.5 Simulated temperature profiles of the r-MoS_2 film to investigate its heat spreading efficiency on Au electrodes. (A) Schematic of the sample configuration of a r-MoS_2 film draped on a current-carrying Au electrode simulated to be 100 nm wide, 15 nm thick, and 10 μm long. (B) Finite-element modelling results of a 3D temperature map of Au electrodes (bare, covered with 10 nm–thick r-MoS_2) supplied with a uniform power of 8 mW via Joule heating. (C) Lateral profiles of the temperature rise across the Au electrodes top surface and the SiO_2 surface (solid dots) and on the r-MoS_2 top surface (open circles). Inset: Cross-sectional 2D mapping of the temperature distribution of the Au electrodes, with and without r-MoS_2.

Although our simulated single crystal MoS_2 heat spreaders displayed excellent electrode cooling capabilities, the insulation effect was stronger in r-MoS_2 (Fig. 4.6). For r-MoS_2, this implied that heat was efficiently directed away from the hot Au electrode laterally through r-MoS_2 but not to the surface of r-MoS_2. This made the surface of the entire device significantly cooler.

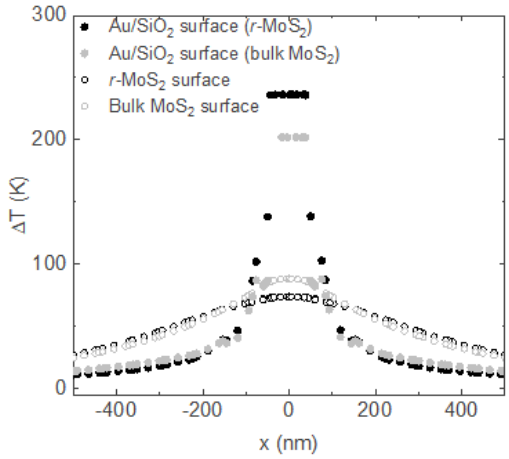

Figure 4.6 Linear temperature profiles for Au electrodes on SiO_2/Si substrates from finite element simulations of r-MoS_2 and single crystalline MoS_2 heat spreaders.

4.3.5 Evaluation of r-MoS_2 as heat spreaders

As an anisotropic heat spreader, our r-MoS_2 film has advantages over isotropic thermal conductors and insulators. Isotropic thermal conductors can spread heat away from heat sources, but they raise the temperature everywhere all at once. Isotropic thermal insulators protect nearby components from the heat source, but the heat source itself is at risk of overheating. Anisotropic heat spreaders provide some degree of control over where heat from the source is dissipated to by allowing engineers to harness the benefits of both thermal conduction and insulation for thermal management.

The extreme anisotropy of our films speaks of the exceptional potential for direction control in thermal management. Their ultralow $\kappa_\perp$ allows for the material to be used in ultrathin

dimensions to achieve a significant insulation effect. Our r-MoS_2 as an ultrathin film allows it to be integrated with delicate electrical components without adding much extra bulk to the system, thereby is potentially compatible with the pursuit of increasingly miniaturized electronics. Moreover, given the electrically insulating nature of our r-MoS_2 films, its deployment means users will not need to be concerned with current leakage or short circuiting in their devices. One limitation of r-MoS_2 is its high interfacial thermal resistances, given its unreactive vdW surfaces. From our finite-element simulations, we found that these interfaces reduced the efficacy of r-MoS_2 to act as heat spreaders (Fig. 4.7). However, given that the interfacial thermal resistances are likely independent of the film thickness, r-MoS_2 films with higher N will reduce the overall contribution of the interface on the total conductance of the film, by providing a larger heat dissipation channel through the film itself.

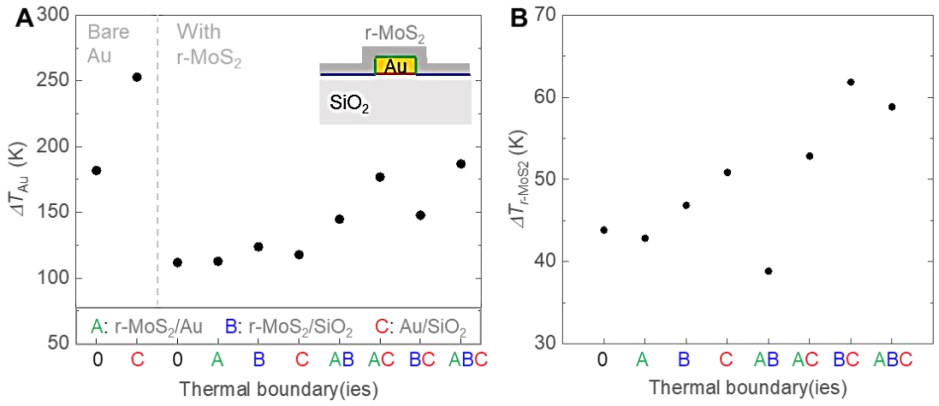

Figure 4.7 Finite element analyses of the effect of interfacial thermal resistance on the efficacy of r-MoS_2 as a heat spreader for Au nanoelectrodes. (A) Surface temperature of the Au electrodes. Inset: Cross-sectional view of the simulated geometry and the relevant thermal interfaces. (B) Temperature of the top surface of the r-MoS_2 heat spreader film. The values of the interfacial thermal resistances used in the simulations are r-MoS_2/Au: 48.1 m^2 K GW^{-1}, r-MoS_2/SiO_2: 7.1 m^2 K GW^{-1}, and Au/SiO_2: 7 m^2 K GW^{-1}.

4.4 Summary

In this chapter, we employed simulations to understand the origins for the ultralow through-plane thermal conductivity and extreme anisotropy. In our MD simulations, we showed that the uniquely suppressed group velocity of the TA phonon mode and the low lifetimes of the dominant heat-carrying LA phonons contributed to the inefficiency of the through-plane thermal conduction. In this regime, the through-plane phonons were scattered within a length scale of a monolayer thickness, which highlighted the glass-like nature of the thermal transport mechanism and the practical limitations of ascribing phonons to the system to describe its transport properties.

Along with the low-frequency Raman measurements, we confirmed a lack of the vibrational shear mode in the layers of the stacked film. This potentially points to a "liquid-like" thermal transport mechanism, because liquids only propagate longitudinal vibrations and lack any shear vibrational modes. This phenomenon has been purportedly observed by Li and Kanatzidis et al. in heavily intercalated, vdW layered $AgCrSe_2$, for the complete disappearance of TA phonon modes in the material[21]. However, on our end, more data needs to be collected to make this claim, such as Li and Kanatzidis's demonstration of an anomalously low volumetric heat capacity of the phonons that resembled the theoretical value for liquids, compared to solids.

We also demonstrated a potential application for our highly anisotropic films: as heat spreaders for nanoelectronics. The efficient in-plane thermal transport helped funnel heat away from heat sources such as current-carrying nanoelectrodes, allowing them to carry more current before reaching electromigration failure. Compared to other isotropic, excellent thermal conductors, our r-MoS_2 film had the additional advantage of an ultrahigh thermal insulation in the through-plane direction. As our finite-element analyses suggest, this property can be useful for maintaining

cooler surfaces while efficiently draining heat from heat sources at the same time. Lower surface temperatures may allow for better user safety and increased user comfort for electronic wearables, in which r-MoS_2 can be incorporated as heat spreaders.

4.5 Appendix

4.5.1 MD simulations details

These four different angles for each pair came about on the condition that each layer did not have more than 10 % strain. We included the 60 º rotations because of the hexagonal symmetry of the system, so the lattice is invariant under a 60 º rotation. This meant that symmetrically distinct commensurate supercells came in pairs as both structures were compatible with the boundary conditions which only depend on the lattice. This allowed us to double the number of layers in our stack "for free". Otherwise, we would have to use cells that are larger in-plane (to accommodate more angles) and/or accept larger strains.

The MD simulations method is defined by the interaction potential between atoms, so we verified that this potential that we used produces phonon dispersions and thermal conductivity values that agree with previous experimental observations and Boltzmann transport calculations based on density functional theory[22]. To study the thermal properties, we excited the system with an optimized (minimized error) driving force then allowed the system to relax (Fig A4.1B). In the context of driving force optimization, an underdriven system (too small of a driving force) gives a large statistical uncertainty in $\kappa_{\perp}$; an overdriven system (too large of a driving force) mainly reflects the thermostat's response. We find that this optimization significantly improves the statistical and numerical quality of the results by leading to smaller error bars for $\kappa_{\perp}$.

The thermal conductivity was computed using homogeneous non-equilibrium molecular dynamics (HNEMD) simulations[23] and implemented in the Graphics Processing Units Molecular Dynamics (GPUMD) package[24]. We also included the effects of thermal expansion by considering the temperature-adjusted lattice constants, which did not have a significant impact on the $\kappa_\perp$ values (Fig. 4.8C). We neglected any quantum effects and all boundary scattering in our simulations. We collected the statistics and averages from 10 independent simulation runs for each system and temperature. The other parameters used in these simulations are compiled in Table 4.1.

Table 4.1. The GPUMD parameters used for the calculation of $\kappa_\perp$.

General	
Time step	1 fs
Equilibration	
Run time	100 ps
Thermostat	Berendsen barostat (nvt.ber)
Thermostat coupling	0.01
Sampling	
Run time	1 ns
Thermostat	Nose-Hoover chains (nvt.nhc)
Thermostat coupling	500 fs
RTC interval	1000 steps
Driving force	1×10^{-4} eV / Å; 5×10^{-4} eV / Å for r-MoS_2 in the z direction

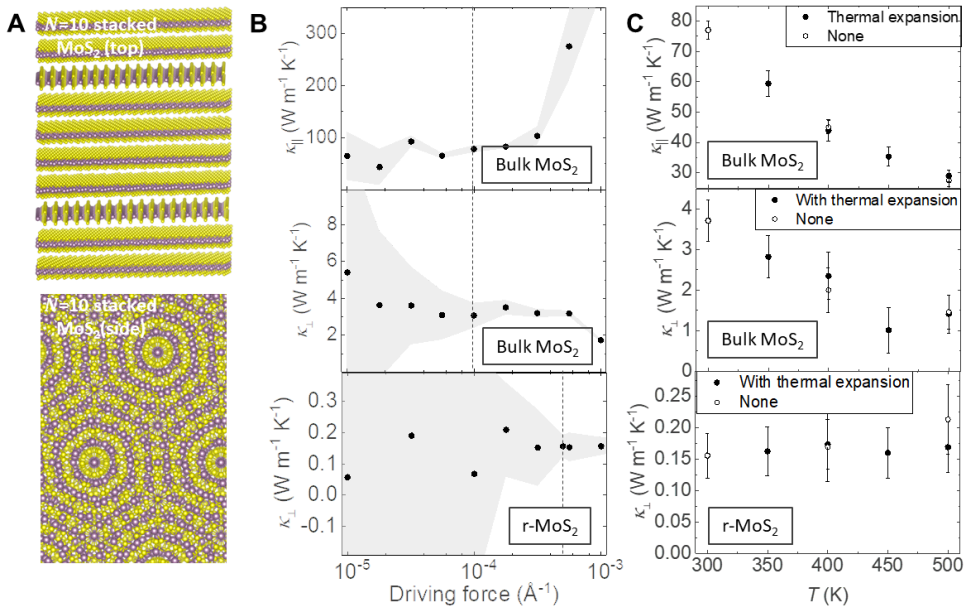

Figure 4.8 Setting up the MD simulations. (A) Atomic model of r-MoS_2, with different orientations of 16.1, 25.28, 34.72, and 43.9 º between the 5 monolayer pairs in relation to one another. (B) The optimized driving forces that were used to thermally excite the model, whereby the grey zone denotes the error. The dashed line denotes the selected driving forces that were eventually used to compute the MoS_2 thermal properties. The ideal driving forces for the bulk and r-MoS_2 in the through-plane direction were found to be 10^{-4} $Å^{-1}$ and ~ 5×10^{-4} $Å^{-1}$ respectively. (C) Effect of thermal expansion on κ.

4.5.2 Supercell size effects on MD simulations

To study the effects of the size of our r-MoS2 atomistic model, we carried out simulations at 300 K for a 2x2x2 supercell of our original r-MoS_2 model, leading to an 8-fold increase from ~ 10,000 atoms to ~ 80,000 atoms. We found that the values of $\kappa_\perp$ and $\kappa_{||}$ already converged for the smaller size. For example, $\kappa_\perp$ for r-MoS_2 only increased slightly within the error bars from 0.16 W m^{-1} K^{-1} to 0.20 W m^{-1} K^{-1}.

Our real-world r-TMD films had finite thicknesses, but the periodic boundary conditions in our MD simulations effectively made our theory germane to infinitely thick films. However, we argue that the ultralow $\kappa_\perp$ does not arise from size effects as seen in other experimentally

interrogated nanomaterials. In the r-MoS_2 system, using the group velocities and lifetimes obtained for the periodic system, we found that the mean free paths (l) of the heat carriers were ~ 2 nm and ~ 10 nm in the through-plane and in-plane directions. $l_\perp$ was thus much shorter than the system dimensions (10 and 20 layers in the 10,000 and 80,000 atom-systems, corresponding to approximately 6 and 12 nm, respectively). As a result, our simulations were a fair representation of the experimental situation even in the case of $\kappa_\perp$ for r-MoS_2 despite the finite size of our model.

4.6 References

1. Kim, S. E. *et al.* Extremely anisotropic van der Waals thermal conductors. *Nature 2021 597:7878* **597**, 660–665 (2021).

2. Hermann, K. Periodic overlayers and moiré patterns: theoretical studies of geometric properties. *Journal of Physics: Condensed Matter* **24**, 314210 (2012).

3. Hjorth Larsen, A. *et al.* The atomic simulation environment—a Python library for working with atoms. *Journal of Physics: Condensed Matter* **29**, 273002 (2017).

4. Erhart, P., Hyldgaard, P. & Lindroth, D. O. Microscopic Origin of Thermal Conductivity Reduction in Disordered van der Waals Solids. *Chemistry of Materials* **27**, 5511–5518 (2015).

5. Liu, K. *et al.* Evolution of interlayer coupling in twisted molybdenum disulfide bilayers. *Nature Communications* **5**, (2014).

6. Jiang, P., Qian, X., Gu, X. & Yang, R. Probing Anisotropic Thermal Conductivity of Transition Metal Dichalcogenides MX2 (M = Mo, W and X = S, Se) using Time-Domain Thermoreflectance. *Advanced Materials* **2**, 1701068 (2017).

7. Togo, A. & Tanaka, I. First principles phonon calculations in materials science. *Scripta Materialia* **108**, 1–5 (2015).

8. Togo, A., Chaput, L. & Tanaka, I. Distributions of phonon lifetimes in Brillouin zones. *Physical Review B - Condensed Matter and Materials Physics* **91**, 94306 (2015).

9. Chaput, L. Direct solution to the linearized phonon boltzmann equation. *Physical Review Letters* **110**, (2013).

10. Fransson, E., Slabanja, M., Erhart, P. & Wahnström, G. Dynasor - A Tool for Extracting Dynamical Structure Factors and Current Correlation Functions from Molecular Dynamics Simulations dynasor — A Tool for Extracting Dynamical Structure Factors and Current Correlation Functions from Molecular Dynamics Simulat. *Advanced Theory and Simulations* **4**, 2000240 (2021).

11. Zhao, Y. *et al.* Interlayer breathing and shear modes in few-trilayer MoS2 and WSe2. *Nano Letters* **13**, 1007–1015 (2013).

12. Zhang, X. *et al.* Raman spectroscopy of shear and layer breathing modes in multilayer MoS2. *Physical Review B - Condensed Matter and Materials Physics* **87**, 115413 (2013).

13. Huang, S. *et al.* Low-Frequency Interlayer Raman Modes to Probe Interface of Twisted Bilayer MoS2. *Nano Letters* **16**, 1435–1444 (2016).

14. Bar-Cohen, A. Thermal management of on-chip hot spots and 3D chip stacks. *2009 IEEE International Conference on Microwaves, Communications, Antennas and Electronics Systems, COMCAS 2009* (2009) doi:10.1109/COMCAS.2009.5385939.

15. Shakouri, A. & Zhang, Y. On-chip solid-state cooling for integrated circuits using thin-film microrefrigerators. *IEEE Transactions on Components and Packaging Technologies* **28**, 65–69 (2005).

16. Ho, P. S. & Kwok, T. Electromigration in metals. *Reports on Progress in Physics* **52**, 301 (1989).

17. Yalon, E. *et al.* Energy Dissipation in Monolayer MoS2 Electronics. *Nano Letters* **17**, 3429–3433 (2017).

18. Freedy, K. M., Olson, D. H., Hopkins, P. E. & McDonnell, S. J. Titanium contacts to Mo S2 with interfacial oxide: Interface chemistry and thermal transport. *Physical Review Materials* **3**, 104001 (2019).

19. Lombard, J., Detcheverry, F. & Merabia, S. Influence of the electron–phonon interfacial conductance on the thermal transport at metal/dielectric interfaces. *Journal of Physics: Condensed Matter* **27**, 015007 (2014).

20. Kimling, J., Philippi-Kobs, A., Jacobsohn, J., Oepen, H. P. & Cahill, D. G. Thermal conductance of interfaces with amorphous SiO2 measured by time-resolved magneto-optic Kerr-effect thermometry. *Physical Review B* **95**, 184305 (2017).

21. Li, B. *et al.* Liquid-like thermal conduction in intercalated layered crystalline solids. *Nature Materials* **17**, 226–230 (2018).

22. Lindroth, D. O. & Erhart, P. Thermal transport in van der Waals solids from first-principles calculations. *Physical Review B* **94**, 115205 (2016).

23. Evans, D. J. Homogeneous NEMD algorithm for thermal conductivity-Application of non-canonical linear response theory. *Physics Letters A* **91**, 457–460 (1982).

24. Fan, Z., Chen, W., Vierimaa, V. & Harju, A. Efficient molecular dynamics simulations with many-body potentials on graphics processing units. *Computer Physics Communications* **218**, 10–16 (2017).

CHAPTER 5: AIR-SOLID INTERFACIAL THERMAL CONDUCTION IN SUSPENDED VDW THIN FILMS

5.1 Introduction

Given their atomic thinness, 2D nanomaterials are highly sensitive to their environment. That also means their interfaces should be considered when measuring their thermal properties.

Since the 2000s, many previously published measurements of suspended 2D vdW were conducted at ambient pressures. Measured $\kappa_{||}$ values for one to few layer MoS_2 lay within the range of 30 – 90 W m^{-1} K^{-1} for both exfoliated[1,2] and vapor phase-grown[3,4] samples. Other thermal measurements of suspended 2D vdW materials under ambient pressures include $MoSe_2$[2], WS_2[5], and graphene[6,7]. These studies did not mention the gas-solid interface effect altogether or assumed it was low without performing the control experiments to verify the assumption.

One of the earliest experiments that considered the effect of air on Raman thermometry measurements was by Chen and Ruoff et al[8]. It was a follow up study from their experiment measuring $\kappa_{||}$ of suspended CVD-grown graphene, for which they neglected air-solid heat interfacial conduction at first. In the later study, they found that the presence of air or CO_2 could increase the apparent value by 20 % from that measured under vacuum, due to an additional parasitic heat loss channel via the gas-solid interface. Later, another study measured the effect of gas on suspended $MoSe_2$ via Raman thermometry, noting that air can leak over 80 % power to the air compared to through the suspended film[9]. In both these experiments, the heat transfer coefficient h, the solid-fluid equivalent of G and defined in the equation for the heat flux, $J = h\,(T_{solid} - T_{fluid})$, was measured to be ~ 10^4 W m^{-2} K^{-1}. That is two orders of magnitude higher than that reported in free convection of air, in which h = 10–25 W m^{-2} K^{-1},[10] which has been used

by studies to justify the exclusion of air-solid interfacial effects in the thermal transport in suspended 2D materials[2]. One possible misconception is that while the convective thermal transfer (typically associated with h) is low, conduction from the film to the air is high.

We note that this chapter was borne out of our own initial errors in our $\kappa_{||}$ measurement using Raman thermometry (Fig. 5.1). Our initial Raman thermometry measurements were performed at ambient pressures, so we measured higher $\kappa_{||}$ in our r-MoS_2 films. Our initial $\kappa_{||}$ values were two to three times higher than what we would eventually measure at weak vacuum ~ 10 Torr.

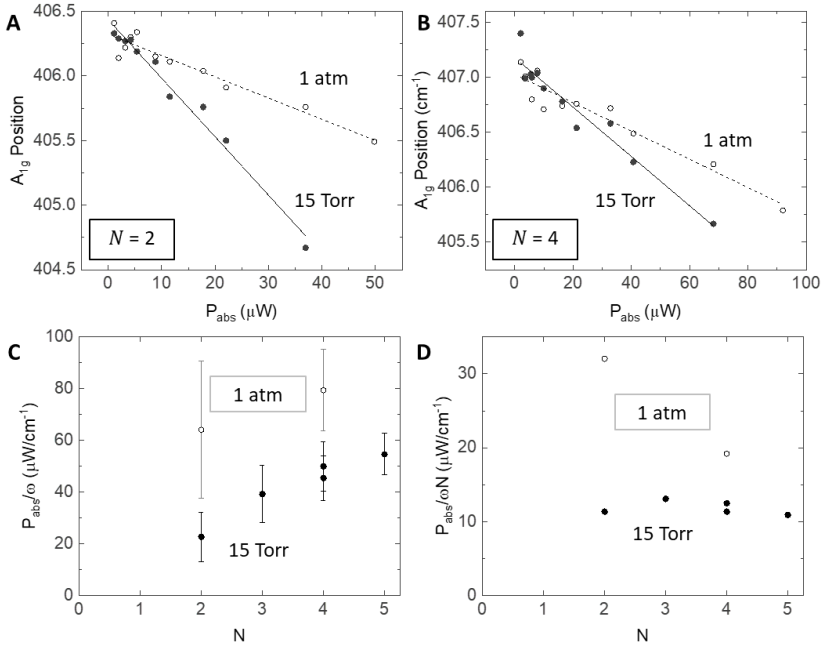

Figure 5.1 Preliminary experiments on the effect of ambient air on Raman thermometry results on suspended r- MoS_2 films. Peak shifts in Raman thermometry for N = 2 (A) and N = 4 (B) suspended r-MoS_2 samples at 15 Torr and at 1 atm of air. (C) In-plane thermal conductance, and the per layer values (D) measured from Raman thermometry for various N r-MoS_2 films. Measurements in air yield the incorrect N-dependence of thermal transport.

This chapter will discuss the factors affecting the gas-solid interfacial conductance, and how that may affect the measurements of intrinsic $\kappa_{||}$ in suspended vdW films. This chapter will present

qualitative arguments and preliminary quantitative data. For a more rigorous quantitative analysis, more data is required. This is currently an ongoing project in the research group.

5.2 Regimes of thermal conduction in gas at different pressures

To consider how gas thermal conduction affects our thermal transport measurements in our films, first we need to understand the different regimes of its pressure dependence (Fig. 5.2). This is dictated by the quantity called the Knudsen number, Kn, defined as

$$Kn = \frac{l}{L}$$

where l is the mean free path of the gas particle and L is the characteristic size of the measurement configuration. When $l \gg L$, heat-carrying air particles travel ballistically in the chamber and primarily interact with the walls of the chamber. This is the free molecular or Knudsen flow regime, where gas can be thought of as discrete particles. When $l \ll L$, air particles collide with each other more frequently than with the chamber walls, so heat flow is diffusive. This is the continuum flow regime, and gas can be thought of as a classical fluid where the Navier-Stokes equation and Fourier's law apply. Here, heat flux is independent of pressure.

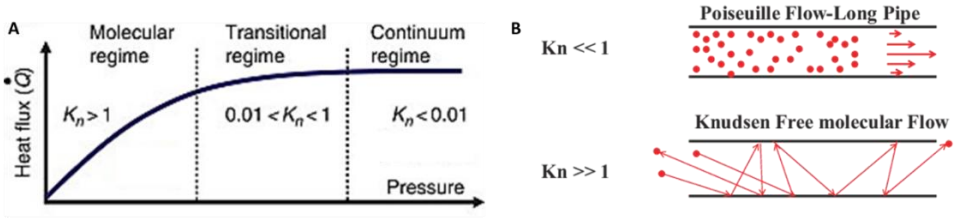

Figure 5.2 Pressure regimes (A) and their molecular picture (B) of thermal transport measurements in gaseous systems. Adapted from references [11] and [12].

The thermal transport in gaseous systems usually involves measurement of heat flux in solid systems separated by an air gap. The measurement geometry can consist of gas in between parallel plates, concentric cylinders, or concentric spheres. The measured heat flux is geometry dependent. A full description of the gas-dependent thermal conduction across the entire pressure regime can be derived from the Boltzmann transport equation, wherein gas particles are assumed to behave as classical hard spheres, but this is challenging to solve analytically, given the large number of variables involved[13]. Liu and Lees *et al.* came up with an approximation solution for a parallel-plate geometry, which is regarded as the expression for pressure-dependent heat flux that most closely agrees with experiment[14]. The solution by Liu and Lees *et al.* is

$$\frac{J}{J_{continuum}} = \frac{J_{free\ molecular}}{J_{continuum} + J_{free\ molecular}} = \frac{1}{1 + \frac{2\ k_B\ T}{L\left(\frac{\alpha}{2-\alpha}\right)\left(1+\frac{\xi}{4}\right)\bar{c}P}}$$

where p is the gas pressure, ξ is the molecular internal degrees of freedom, $\bar{c}$ is the mean molecular speed of the gas particles, and α is the thermal accommodation coefficient, or the fraction of impinging gas atoms that fully thermalize with the solid surface. Looking at the limits as $p \to 0$ or $p \to \infty$ gives a qualitative picture of the curve of J as a function of p, roughly matching our own experimental results, which we will show later in the chapter.

We note that our discussion here will neglect convection entirely. Convective thermal transport is more efficient when the temperature gradient spans a longer distance. To justify this assumption, we calculate the quantity known as the Rayleigh number, defined as

$$Ra = \frac{Time\ scale\ for\ diffusive\ thermal\ transport}{Time\ scale\ for\ convective\ transport} = \frac{\rho\ \beta\ \Delta T\ l^3\ g}{\eta\ \alpha'}$$

where ρ is the density of air, β is the expansion coefficient, l is the characteristic length scale, g is the gravitational acceleration, η is the dynamic viscosity of air, and α' is the thermal diffusivity of air. Even under atmospheric conditions and using ΔT = 100 K (upper limit of total $\Delta\omega$ from Raman measurements) and $l \sim R$ = 2.5 μm[a], we estimate this upper limit of $Ra \sim 10^{-7}$ << 1, indicating that heat transport from the laser spot to the TEM hole edge is dominated by diffusive air transport.

5.3 Pressure-dependent Raman thermometry measurements

To measure the interfacial thermal transport across the air-MoS_2 interface, we suspended a large area MOCVD-grown MoS_2 monolayer onto holey SiN_x/Si TEM grids, using the sample preparation protocol in Chapter 3. The SiN_x layer thickness is 200 nm. Monolayer MoS_2 is prone to rupture. To improve the sample yield, we used smaller grain sizes of MoS_2 $d \leq 500$ nm, which was found to give a higher success rate for suspension. Prior to peeling, we spincoated our as-grown MoS_2 with 495k PMMA A4 dissolved in anisole as the handling layer. Previous programmed vacuum stacking protocols of r-MoS_2 used a higher concentration of PMMA of A8, which would yield thicker PMMA handling layers. In this case, a thinner layer would allow for easier PMMA removal during the high-temperature Ar/H_2 annealing step and reduce the failure rate of suspending the MoS_2. We use monolayer MoS_2 to increase the sensitivity of our measurements to the interfacial thermal conductance, compared to higher N films, by reducing the fraction of heat dissipated through the solid as demonstrated in Fig. 5.1. We assume that the MoS_2-air interfacial thermal conductance is the same for all N.

[a] The other parameters used for the calculations are ρ = 1.225 kg m^{-3}, β = 3.4 x 10^{-3} K^{-1}, η = 18.32 x 10^{-6} Pa s^{-1}, α' = 22.39 x 10^{-6} m^2 s^{-1}.

To perform pressure-controlled Raman thermometry, we connected our Linkam stage to a piston pump (Fig. 5.3) and controlled the vacuum pumping rate of the stage by placing a needle valve between the stage and the pump. The minimum pressure achieved, measured via a Pirani Gauge on the load side of the chamber, is ~ 15 Torr. All experiments were performed in air.

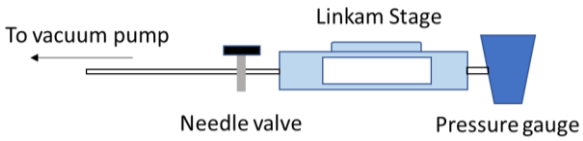

Figure 5.3 Schematic of instrument setup for pressure-dependent Raman thermometry.

As seen from Fig. 5.4, the measured Raman peak shift ω varies non-linearly on the air pressure. To explain this observation, we first identified three heat loss channels that contribute to the measured ω value, namely (i) Radial solid conduction through the suspended MoS_2 film, G_{MoS2}; (ii) solid-gas interfacial conduction G_{g-s}; (iii) gas conduction G_{air}. We provide a model to describe the pressure dependence, which matches the characteristic shape reported in other pressure-dependent thermal transport studies across gas-solid interfaces[15,16].

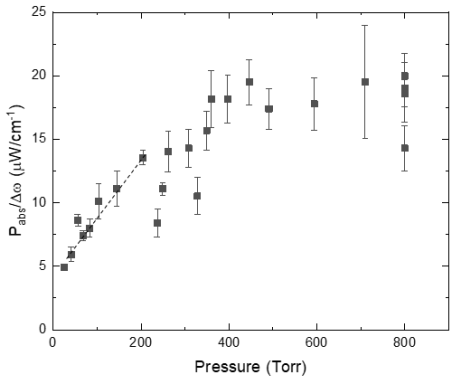

Figure 5.4 Pressure dependence of apparent thermal conductance of suspended monolayer MoS_2, measured using Raman thermometry. (The y axis intercept of the linear fit for the $p <$ 200 Torr regime signifies thermal conduction purely through the solid.) From our extrapolation, we calculate intrinsic κ = 20.4 W m^{-1} K^{-1} for monolayer MoS_2.

We describe heat transport in the system using an effective thermal circuit as shown in Fig. 5.5A.

Heat conduction through the MoS_2 film is independent of air pressure p. The y axis intercept corresponds to the lower limit on the intrinsic value of $\kappa_{||}$ in MoS_2. Extrapolating the linear fit at p < 200 Torr gives a lower limit on $\kappa_{||}$ of 20.4 W m^{-1} K^{-1}.

In Fig. 5.5B, we schematically show two regimes in the pressure dependence of the thermal conductance measured: the linearly increasing regime and the constant regime. At high p values near ambient pressures, thermal transport is limited by conduction through air, rather than the air-solid interface, so $G_{air} \ll G_{g-s}$. In this regime, air molecules collide with each other more frequently than with the MoS_2 surface. The thermal conductivity of air (neglecting convection effects) is independent of p. This relation can be observed from the relation $\kappa \sim C_v\, l$. For instance, at higher pressures, C_v increases with the number density of air molecules to store or transport energy, but at the same time l decreases proportionally. So, the opposing trends in C_v and l cancel each other out.

As p decreases, intermolecular collisions decrease and the air molecules start to experience fewer scattering events with each other, i.e., more resembling ballistic transport. At this stage, the air molecules collide with the surface of the MoS_2 rather than with other air molecules, and this becomes the limiting factor for thermal transport. Boundary scattering is the dominant scattering, so the transport characteristic length scale is no longer the air mean free path, but the system size that is independent of p. Equivalently, $\kappa \sim C_v$, so the conduction G_{g-s} scales with the rate of collision with the MoS_2 surface.

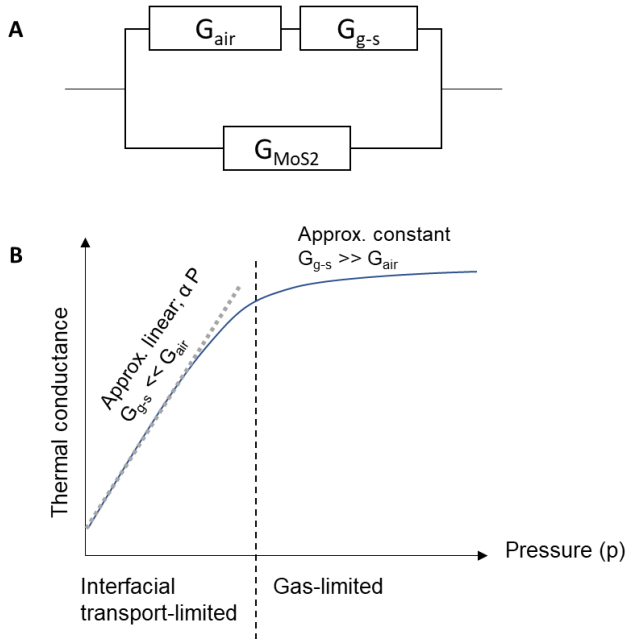

Figure 5.5 Model for understanding pressure-dependence of measured thermal conductance in suspended MoS_2. (A) Analogous circuit diagram representing the sources of thermal resistance in our sample configuration. The three heat loss channels are air conduction G_{air}, conduction through the gas-solid interface G_{g-s}, and conduction through the MoS_2 film G_{MoS2}. (B) Plot of the air-solid thermal conductance of suspended monolayer MoS_2 vs its surrounding air pressure.

An intriguing question is whether the transition pressure between the interfacial transport regime and the gas regime in Fig. 5.4 holds any physical meaning. This $p_{transition}$ in Fig. 5.4 is approximately 200 – 300 Torr. One possibility is that $p_{transition}$ occurs when $l \sim s$, denoting some characteristic length scale of the measurement system. If we assume that the mean free path of air scales proportionately with pressure in accordance with the ideal gas law[17] as shown in Fig. 5.6, using the mean free path of air under ambient pressures, we can estimate that s ~ 180 – 270 nm. This value is smaller than the laser beam $\frac{1}{e^2}$ radius $r_0 \sim 0.7$ μm as measured in Chapter 3. Future studies should look into the significance of this transition point, and find ways to conduct a more precise determination of this value. This may require using a measurement

chamber with a better control of the pressure, and perhaps that is able to descend to even lower pressures to confirm the linear relation of the conductance with p that $p_{transition}$ > 20 Torr.

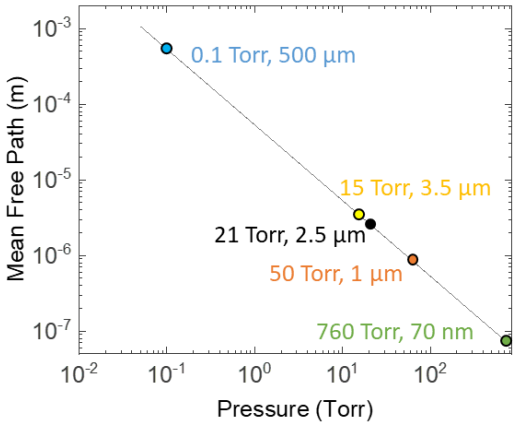

Figure 5.6 Calculation of the mean free path l of air molecules. We used the fact that at 1 atm = 760 Torr, l ~ 70 nm.

Raman thermometry may have insufficient precision in measuring this transition point. We note that this $p_{transition}$ value is weakly defined in Fig. 5.4, given the noise levels of the data points that are noticeably larger at higher p. Under these measurement conditions, the temperature rise due to laser heating was smaller, thanks to the efficient heat dissipation channel through the air. This reduces the magnitude of the Raman peak shift $\Delta\omega$ from the ambient temperature peak position and runs up against our Raman spectrometer sensitivity that is reasonably around 1 cm^{-1}, translating to a measurable temperature rise of 60 K. This poses a challenge for small temperature increase measurements that are especially apparent when heat dissipation from the heat source is efficient.

In the free molecular regime, the slope of the linear fit to the data points in Fig. 5.4 is theoretically proportional to the thermal accommodation coefficient α, defined by Maxwell as

$$\alpha = \frac{T_{incident} - T_{reflected}}{T_{incident} - T_{solid}}$$

It is tempting to derive from the slope a α value for MoS_2 and air. But this α value might be between air and some unknown substance on the MoS_2 surface, and not necessarily pristine MoS_2; we would first need to confirm that the surface of our MoS_2 is indeed free of contamination. Any hydrocarbon residue is known to increase the "stickiness" of air particles to the surface[18–20]. Moreover, experiments have shown that a layer of gas typically adsorbs onto metal surfaces even after cleaning by heating at elevated temperatures under ultrahigh vacuum[20,21]. We note that our MoS_2 top surface was coated with PMMA, which was later removed at high temperature under Ar/H_2 gas. At the molecular level, the MoS_2 surface is probably not entirely carbon free. Further characterization is needed to confirm the surface structure of our MoS_2 films before we can measure α.

Nevertheless, this could be an exciting direction to explore in the future: To the best of our knowledge, α has not been directly measured for any TMD material to date. Furthermore, α of 2D films could be abnormally low compared to bulk materials, such as what is predicted by MD simulations for carbon nanotubes[22] due to their low dimensionality. Moreover, previous research has demonstrated the capability to pattern large-area, suspended 2D films with corrugations at periodicities close to the mean free path of air molecules corresponding to a wide range of pressures. Surface cleanliness notwithstanding, this suggests that it may be possible to tune α of 2D vdW monolayers via a deliberate "roughening" nanostructuring strategy.

5.4 Other factors impacting air-solid heat loss rate

5.4.1 Laser spot size

We predict changing the laser spot size r_0 can alter the apparent thermal conductance of suspended MoS_2 films. First, it will impact the temperature rise of the MoS_2, since the laser power may either spread out or concentrate more tightly within the beam spot on the film. It may also affect conduction to air, as a larger beam spot size might increase the $\frac{1}{e^2}$ area of the film contributing to air-solid conduction, based on the temperature profile of the surface. All these outcomes also depend on the air pressure in the measurement chamber.

To investigate the effects of r_0 on the measured thermal conductance (power absorbed by film over its measured temperature rise) in the free molecular regime, we varied the laser spot size by altering the laser focus and measuring the subsequent ω-P curves similar to Fig. 3.14A. The beam spot sizes could not be set arbitrarily to a desired value before measurement; so we measured the beam spot size in situ every time we changed the lens height. To that end, we performed the same knife-edge method as described in Section 3.5.1.2 across the MoS_2 monolayer suspended on the TEM grid. We tracked the integrated A_{1g} Raman peak intensity for our linear Raman mapping. No Raman signal was observed in the region of the MoS_2 supported by the SiN_x, because the underlying 200 nm substrate provided complete destructive interference at the 532 nm excitation wavelength. We fit our linear map of the integrated Raman intensity to a step function. The circular step edge of the TEM hole (compared to the standard straight edge) yielded beam spot size values smaller than what we measured using a Si-Au substrate straight knife edge method. To account for the discrepancy, we performed a first order transformation of the error-function fitted beam radius to the value derived from direct camera images of the beam

that were fitted to a Gaussian intensity distribution using the software ImageJ. The r_0 values calculated this way matched what we observed under typical measurement conditions for the same focus as reported in Section 3.5.1.2.

We performed the measurements at the pressures of 20 Torr (Fig. 5.7), 80 Torr, and 160 Torr (Fig. 5.8A, B). For each pressure level, we observed that a larger beam spot size increased the measured absolute thermal conductance $\frac{P_{abs}}{\Delta\omega}$ of the film, indicating more efficient heat dissipation from the laser heat source. To determine which effect dominated in the 20 Torr measurements (Fig. 5.7), the film conduction or the air-solid interfacial conduction, we fit the data to the model

$$\frac{P_{abs}}{\Delta\omega} = \frac{A}{\ln\left(R/r_0\right)} + B \cdot (r_0 - r_c)^2 + C$$

where A, B, C, and r_c are fitted constants; and R is the radius of the suspended film area. The $\frac{A}{ln\left(R/r_0\right)}$ term refers to the contribution of the film conduction, as discussed in Section 3.5.2. The $B \cdot (r_0 - r_c)^2$ term refers to the contribution from the air-solid conduction, which is predicted to scale with the "hot" laser area size.

Given the noise levels of the data in Fig. 5.7, the fitted values for A, B, C, and r_c have large uncertainty. The value of B is also nonphysical as it is negative. As such, we cannot make any quantitative claims about these parameters[b]. The model may also need to be tweaked to account for other heat transfer channels not yet considered.

[b] The fitted values were A = 730 ± 680, B = -710 ± 530, C = -430 ± 430, and r_c = 0.40 ± 0.16.

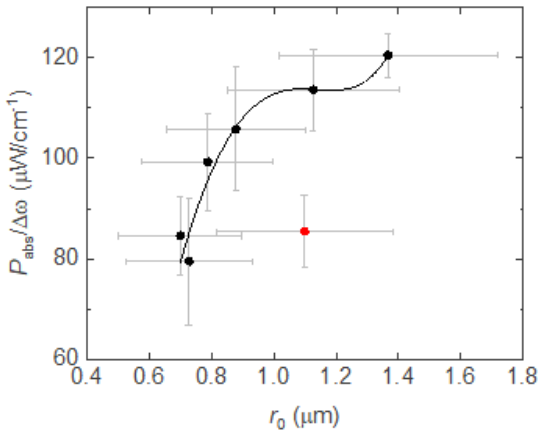

Figure 5.7 Effect of beam spot size r_0 on measured thermal conductance at 20 Torr using Raman thermometry. The data points were fitted to the model $y = \frac{A}{ln\left(R/r_0\right)} + B \cdot (r - r_c)^2 + C$. The red point is ignored as an outlier during fitting.

At higher pressures, the values for $\frac{P_{abs}}{\Delta\omega}$ increase, suggesting that air conduction increases with pressure. However, more data are necessary to verify the quantitative trend between the absolute conductance with r_0. Admittedly, we have a large uncertainty for the r_0 and $\frac{P_{abs}}{\Delta\omega}$ values to pinpoint a clear trend. The uncertainty in r_0, which stems from the error function fitting and the linear transformation, maybe reduced by solving the full or more complete equation of the knife edge method for the linear Gaussian beam intensity mapping over a circular step edge. The large uncertainty in $\frac{P_{abs}}{\Delta\omega}$ is also one of the limitations of Raman thermometry on our instrument. Higher resolution P_{abs}-$\Delta\omega$ data are needed for better linear fitting of $\frac{P_{abs}}{\Delta\omega}$, and this may require a revamp on the instrumentation, such as to accommodate more ND filters to access more P_{abs} options than as shown in Fig. 3.14A.

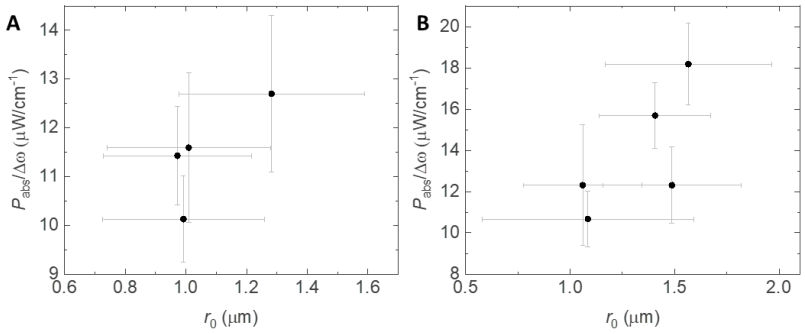

Figure 5.8 Measured thermal conductance of monolayer MoS_2 with various beam spot sizes at pressures of 80 Torr (A) and 120 Torr (B) respectively.

For future follow-up work and a more complete picture of the various mechanisms for heat dissipation channels, the same experiment should be conducted at higher pressures in the continuum regime. We predict that the effect of the beam spot size will have a smaller measurable effect of the absolute conductance. This is because the air-solid interfacial conduction has a significantly smaller contribution to the heat dissipation, compared to the pressure-independent thermal conduction through air, at pressure levels close to atmospheric values, as discussed in Section 5.2.

5.4.2 Suspended film area

Under vacuum conditions, the measured temperature rise of suspended MoS_2 should increase with the hole size following the relation $\sim \ln(R)$ as per Section 3.5.1.2, assuming $\kappa_{||}$ remains constant[8]. A larger hole size will also increase the heat loss rate to the environment, as a larger surface area is exposed to the ambient gas for thermal exchange. This may in turn temper the measured temperature rise.

Both competing effects might result in an overall small change in the temperature rise per power absorbed by the film for different TEM grid hole sizes. In other words, the hole size might have

little perceivable effect on the measured thermal conductance and hence apparent thermal conductivity of the film, depending on instrument sensitivity. This is similar to what has been observed by Chen and Ruoff *et al.*, who performed Raman thermometry on CVD-grown graphene suspended on various TEM grid hole sizes ranging from 3 to 10 μm in diameter in air[8]. However, we note that graphene has a higher $\kappa_{||}$ than MoS_2, so solid conduction in graphene is less sensitive to air conduction. Experiments are needed to verify whether MoS_2 may be able to reveal which heat dissipation channel dominates.

5.4.3 Other factors

We speculate that the value of G_{g-s} will be affected by the following factors, instrument sensitivity and hence measurability notwithstanding:

- Temperature of system and gas: In the free molecular regime, gas thermal exchange occurs by gas molecules adsorbing to the surface of the solid. Since adsorption is a thermally activated process, higher temperature gives adsorbates energy to liberate themselves from the surface. In other words, adsorbates have less interaction time with the solid surface at high temperatures. The effect of temperature will in particular change the value of α.

  In the continuum flow regime, the mean molecular speed of the particles increases with the square root of the temperature (internal energy ~ kinetic energy, $T \sim v^2$). So, we would expect the air heat loss channel to increase with T.

  The predicted impact of temperature on the pressure dependent thermal conductance curve as illustrated in Fig. 5.9.

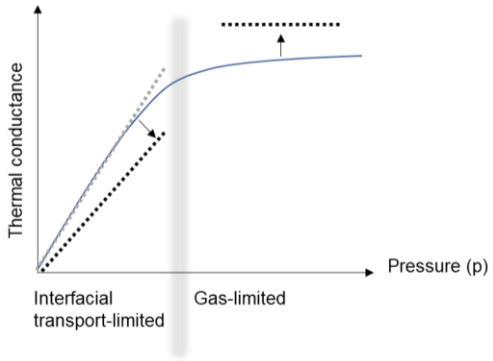

Figure 5.9 Predicted change in the measured pressure-dependent thermal conductance curve in gas with increasing temperature. The effect of temperature on the thermal conductivity of the solid itself is ignored.

- Chemical species of gas: Previous studies have observed or predicted that the higher the molecular mass of the gas particles, the more efficient the energy exchange between the gas and the solid, so the higher the value of α. Energy exchange also depends on the interaction energy between the gas particles and solid surface. vdW materials lack dangling bonds on the surface. This could be one reason that α of pristine surfaces of vdW materials could be smaller than that of metal surfaces in theory.
- Solid surface conditions: As mentioned previously, surface contamination might alter the value of α. Cleaning methods are required to expose the pristine MoS_2 surface for accurate α measurement, though this itself might be an engineering challenge. Metal surfaces can typically withstand temperatures over 1000 ºC and ion irradiation for intense cleaning purposes. Our MOCVD-grown MoS_2 is annealed at temperatures of 350 ºC or less. Its atomic thinness also makes it fragile, so the bombardment of chemical species (such as during a plasma treatment) might compromise the structural integrity and continuity of the material. Future work includes finding gentle yet effective cleaning

processes for vdW monolayers or developing new polymer free transfer and suspension methods to reduce carbon contamination on the surface[23,24].

5.5 Summary

In this chapter, we looked at several environmental factors that might impact the measured in-plane thermal conductance of suspended 2D films. Given the atomic thinness of these materials, surface conditions and the environment may have a large impact on the measured conductance. Air-solid interfacial conduction has often been neglected in previous studies, but we observed that this heat loss channel is significant and comparable to solid conduction through the film, which will be more pronounced with lower N.

A primary factor for interfacial thermal conduction is gas pressure. Its impact on thermal conductance can be separated into two regimes: free molecular and continuum flow. MoS_2's atomic thinness may open up new opportunities for the monolayer to be used as a gas sensor with electrical or optical interfacing beyond Raman thermometry, similar to the function of the filament in a Pirani gage.

How heat loss rate is affected by other factors such as sample preparation and measurement geometries and conditions is less straightforward, especially for factors that impact both solid conduction and air-gas conduction. We are currently limited in particular by the sensitivity of our instrument. More data and an improved instrument may be required to address the questions raised and pinpoint relationships between various parameters in the future.

5.6 References

1. Yan, R. *et al.* Thermal conductivity of monolayer molybdenum disulfide obtained from temperature-dependent Raman spectroscopy. *ACS Nano* **8**, 986–993 (2014).

2. Zhang, X. *et al.* Measurement of Lateral and Interfacial Thermal Conductivity of Single- and Bilayer MoS2 and MoSe2 Using Refined Optothermal Raman Technique. *ACS Applied Materials and Interfaces* **7**, 25923–25929 (2015).

3. Sahoo, S., Gaur, A. P. S., Ahmadi, M., Guinel, M. J. F. & Katiyar, R. S. Temperature-dependent Raman studies and thermal conductivity of few-layer MoS2. *Journal of Physical Chemistry C* **117**, 9042–9047 (2013).

4. Dolleman, R. J. *et al.* Transient thermal characterization of suspended monolayer MoS2. *Physical Review Materials* **2**, 114008 (2018).

5. Peimyoo, N. *et al.* Thermal conductivity determination of suspended mono- and bilayer WS2 by Raman spectroscopy. *Nano Research* **8**, 1210–1221 (2015).

6. Balandin, A. A. *et al.* Superior thermal conductivity of single-layer graphene. *Nano Letters* **8**, 902–907 (2008).

7. Cai, W. *et al.* Thermal transport in suspended and supported monolayer graphene grown by chemical vapor deposition. *Nano Letters* **10**, 1645–1651 (2010).

8. Chen, S. *et al.* Raman measurements of thermal transport in suspended monolayer graphene of variable sizes in vacuum and gaseous environments. *ACS Nano* **5**, 321–328 (2011).

9. Reig, D. S. *et al.* Unraveling Heat Transport and Dissipation in Suspended MoSe2 from Bulk to Monolayer. *Advanced Materials* **34**, 2108352 (2022).

10. Kosky, P., Balmer, R., Keat, W. & Wise, G. Mechanical Engineering. *Exploring Engineering* 317–340 (2021) doi:10.1016/B978-0-12-815073-3.00014-4.

11. Chae, J., Stark, B. H. & Najafi, K. A micromachined Pirani gauge with dual heat sinks. *IEEE Transactions on Advanced Packaging* **28**, 619–625 (2005).

12. Velasco, A. E., Friedman, S. G., Pevarnik, M., Siwy, Z. S. & Taborek, P. Pressure-driven flow through a single nanopore. *Physical Review E - Statistical, Nonlinear, and Soft Matter Physics* **86**, 025302 (2012).

13. Rader, D. J., Trott, W. M., Torczynski, J. R., Castañeda, J. N. & Grasser, T. W. *Measurements of Thermal Accommodation Coefficients*. http://www.ntis.gov/help/ordermethods.asp?loc=7-4-0#online (2005).

14. Springer, G. S. Heat Transfer in Rarefied Gases. *Advances in Heat Transfer* **7**, 163–218 (1971).

15. Peck, R. E. & Lokay, J. O. Accommodation coefficients of hydrogen, helium, air, and argon for chrome surfaces at reduced pressures. *Journal of Chemical and Engineering Data* **3**, 37–42 (1958).

16. Ganta, D., Dale, E. B., Rezac, J. P. & Rosenberger, A. T. Optical method for measuring thermal accommodation coefficients using a whispering-gallery microresonator. *Journal of Chemical Physics* **135**, 2–8 (2011).

17. Nave, R. Mean Free Path. *Hyperphysics* http://hyperphysics.phy-astr.gsu.edu/hbase/Kinetic/menfre.html.

18. Liang, Z., Evans, W., Desai, T. & Keblinski, P. Improvement of heat transfer efficiency at solid-gas interfaces by self-assembled monolayers. *Applied Physics Letters* **102**, 061907 (2013).

19. Saxena, S. C. & Joshi, R. K. *Thermal accommodation and adsorption coefficients of gases*. (Hemisphere Publishing Corporation, 1989).

20. Bayer-Buhr, D., Vimal, M., Prakash, A., Gross, U. & Fieback, T. Determination of thermal accommodation coefficients on CaSiO3 and SiO2 using molecular dynamics and experiments. *International Journal of Heat and Mass Transfer* **183**, 122219 (2022).

21. Thomas, L. B. & Olmer, F. The Accommodation Coefficients of He, Ne, A, H2, D2, O2, CO2, and Hg on Platinum as a Function of Temperature. *J Am Chem Soc* **65**, 1036–1043 (1943).

22. Schiffres, S. N. *et al.* Gas diffusion, energy transport, and thermal accommodation in single-walled carbon nanotube aerogels. *Advanced Functional Materials* **22**, 5251–5258 (2012).

23. Yang, J. *et al.* MoS 2 Liquid Cell Electron Microscopy Through Clean and Fast Polymer-Free MoS 2 Transfer. *Nano Letters* **19**, 1788–1795 (2019).

24. Zhang, J. *et al.* Clean Transfer of Large Graphene Single Crystals for High-Intactness Suspended Membranes and Liquid Cells. *Advanced Materials* **29**, 1700639 (2017).

CHAPTER 6: MUSINGS ON FUTURE RESEARCH DIRECTIONS

6.1 Introduction

Two dimensional materials have attracted significant research interest for their diverse optical, electrical, magnetic, and mechanical properties for both fundamental research and future practical applications. This thesis argues that 2D materials may offer up exciting new avenues for research into its thermal properties.

The atomic thinness of 2D vdW materials makes it especially suited for probing low-dimensional thermal transport and interfacial phenomena. We list below several exciting avenues for future research.

6.2 Rotation angle

Recent studies have opened up new questions on the extent to which the rotation angle between two stacked crystalline 2D films can tune the properties of the twisted bilayer. A lot, it seems—since the reveal of "magic angle" twisted bilayer graphene manifesting superconductivity in experiments[1], subsequent research has led to discoveries of other emergent properties such as ferromagnetic ordering[2,3], correlated insulators[4–6], Wigner crystal states[7], and more superconductivity observations[8–10] in stacked graphene, TMDs, h-BN, and their heterostructures. These discoveries notably pertain to the behavior of the electrons in response to a moiré lattice. A related question is whether twist angle may have a similar effect on the phononic transport properties. If affirmative, twist angle could be an exciting means to tune κ and hence ρ in stacked films, given the infinite tunability in twist angle in stacked 2D vdW films.

Liu and Wang *et al.* measured the effects of twist angle on the optical and vibrational properties of a MoS_2 bilayer[11]. The researchers reported that save the optimal AA (0 º) and AB (60 º) twist angles that saw maximum interlayer coupling, other twist angles led to an expanded interlayer spacing and reduced effective interlayer mechanical coupling in the bilayers, both characteristics of which were of similar magnitudes indiscriminate of the twist angle. However, the coarse ~ 10 º angular resolution in their experiments might have inadvertently concealed any fine-scale angular trend, or even potential "magic angle" effects analogous to superconductivity, which manifested at a slight twist angle of 1.08 º.[1]

Experimentally, the study of the angle dependence of κ requires high precision preparation methods. Our programmed vacuum stacking method and growth of polycrystalline films do not provide angular control in our stacked multilayers, so the technique is not suitable without modification for generating the necessary samples towards this systematic investigation. Nevertheless, on top of existing stacking techniques used for the array of "magic-angle" studies, my group has reported on a new robotic stacking approach that could provide a scalable and precise means for fabricating twisted 2D stacks, as long as the large crystalline domain (d > 100 μm), single crystalline, or aligned films can be prepared in pixelated form the first place[12]. Using this setup, Mannix and Ye *et al.* generated multilayer WS_2 samples with precise angle control that could, in theory, be used for angle-dependent measurements of $\kappa_\perp$ and $\kappa_{||}$ in stacked 2D vdW films (Fig. 6.1). Moreover, they observed lattice reconstruction in N = 4 angle-controlled r-WS_2, which could potentially impact lateral and vertical thermal transport in the film. I speculate that lattice reconstruction may lead to a higher $\kappa_\perp$ than films without reconstruction, which could be a thrilling avenue of research.

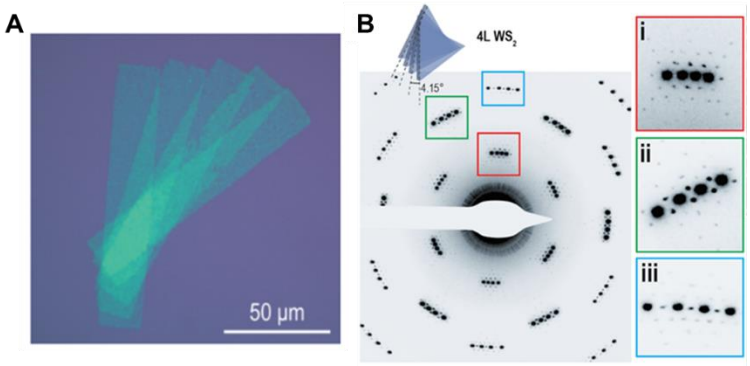

Figure 6.1 Angle control of stacking of single-crystal, MOCVD-grown WS_2, assembled using an automated stacking setup. (A) Optical image of N = 4 WS_2 stacked at a constant angle of 12.5 º. (B) Selected-area electron diffraction of N = 4 WS_2 films, with reconstruction effects observed (insets i, ii, iii). All the images here are reproduced from reference [12].

6.3 Heterostructures

There exists a broad library of 2D and thin film materials that can be intergrated to form an infinite library of heterostructures, whose vertical compositions are tailorable with atomic precision. Besides the family of 2D vdW films, recent years have also seen the development of large area 2D polymers (e.g., [13]), self-assembled nanocrystal films (e.g., [14,15]), and self-assembled molecular crystals (PTCDA[16]) that can also be used as building blocks for artificial hetero-solids. The resulting materials—and the possibilities for thermal design—are unlimited.

For vertically assembled stacked 2D heterostructures, adding in atomic-mass mismatch on top of rotational mismatch could yield two potential outcomes in $\kappa_\perp$: (i) a reduction or (ii) similar to higher value. Noting that our $\kappa_\perp$ in r-MoS_2 is already ultralow, a reduction in $\kappa_\perp$ may break the record for the lowest κ measured in a fully dense solid and possibly attain a higher ρ. On the other hand, an increase in or constant $\kappa_\perp$ raises new questions about the mechanism of thermal transport, such as why thermal transport is more sensitive to the rotation angle than the atomic mass mismatch.

Moreover, 2D vdW materials are compatible with nanofabrication techniques, which may allow for the nanostructuring or fabrication of lateral heterostructures to further tune the directionality of thermal transport and introduce thermal anisotropy in plane. First, we note that the resolution of these patterning techniques need to be of the order of 1 μm or less, as low as 10 nm. For example, graphene shows an exceptionally "long" average in-plane phonon mean free path of 800 nm. Such spatial resolution is achievable by current nanofabrication techniques, and the advancement in technology will only extend the capabilities to access even smaller length scales in a widening swath of materials.

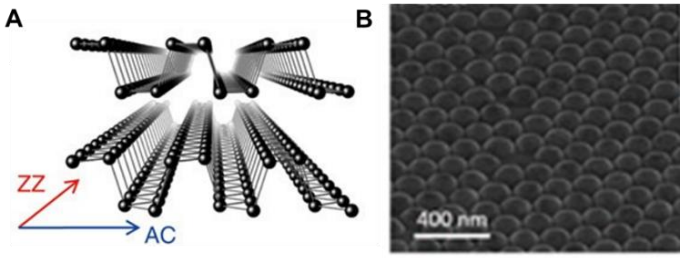

Figure 6.2 Nano- to atomic-level nanostructuring to tune $\kappa_{||}$ in 2D vdW monolayers. (A) At the atomic level, black phosphorus consists of layers of corrugated lamellae of phosphorus atoms that are bound by weak vdW forces in the vertical direction. Heat travels faster along the zigzag direction than the armchair direction. The same atomic structure could inspire nanotexturing efforts to imbue in-plane anisotropy in other atomically flat 2D vdW monolayers. Image is reproduced from reference [17]. (B) SEM image of monolayer MoS_2 conformally grown on a corrugated SiO_2/Si substrate. The image is reproduced from reference [18].

For example, one could introduce symmetry breaking or high-aspect-ratio texturing at the nanoscale to lengthen the transport pathways of thermal carriers and break the symmetry of the phonon dispersion, by generating nanoscale or atomically corrugated quasi-2D films analogous to the ruching of monolayer black phosphorus (Fig. 6.2A)[17]. Or, directional patterning at certain spatial frequencies might scatter the phonons with the corresponding mean free paths in that orientation. Research by Lee and Kang *et al.* has already showed one applicable nanostructuring

technique for this cause. They have developed the capabilities to grow nanocorrugated monolayer TMD films conformally on nanoparticle-textured substrates (Fig. 6.2B)[18].

Another strategy is the creation of 1D interfaces in-plane to scatter thermal carriers along a certain direction. Our group also has developed patterned-regrowth[19,20] and coherent superlattice growth[21] techniques that can introduce mass mismatch in the lattice to engineer the scattering of in-plane phonons in a monolayer (Fig. 6.3). The fabrication of these 2D heterostructures is likely compatible with many vdW layered materials that can be grown using the CVD process, with optimization.

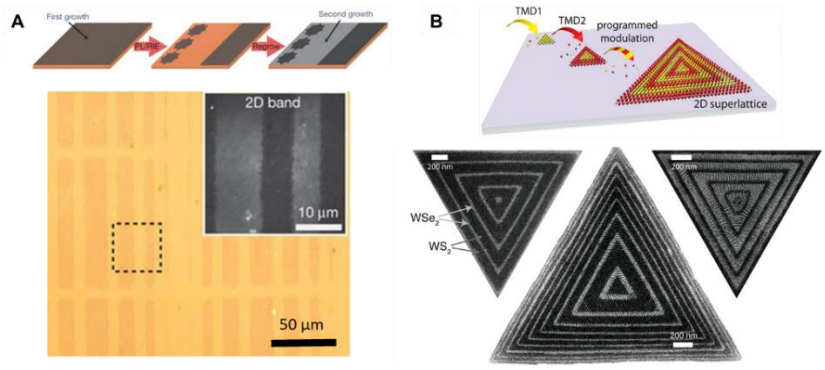

Figure 6.3 Fabrication of atomically thin lateral vdW heterojunctions and heterostructures. (A) Optical image of a graphene/h-BN heterostructure on a Si/SiO_2 substrate. Inset, a 2D map of the Raman graphene 2D band (area indicated by the dotted box), showing a stark contrast between the regions. Reproduced from reference [19]. (B) Schematic of the MOCVD steps to generate 2D monolayer TMD superlattices, and the SEM images of three resulting monolayer WS_2/WSe_2 superlattices with tunable domain sizes. Reproduced from reference [21].

One can imagine that the spatial patterning of nanoscale textured features and the incorporation of 1D interfaces can be combined with vertical compositional tailoring of the constituent monolayers to generate 3D anisotropic thermal conductors among stacked vdW films, in which heat can be routed along any direction on demand.

6.4 Strain

As discussed in Section 2.4.1, strain can potentially be used as a parameter to tune the thermal properties of 2D vdW crystals. We performed preliminary MD simulations on the effect of out-of-plane strain on $\kappa_\perp$ of r-MoS_2 and found a more pronounced effect for compressive strain compared to tensile strain (Fig. 6.4A). Out-of-plane expansion led to an effective decrease in v_g in this direction, due to the larger Brillouin zone and the weakening of the force constants. This v_g reduction led to a fall in $\kappa_\perp$ even if scattering (and hence lifetimes) remained unaffected[22]. On the other hand, applying an out-of-plane compressive strain (± 5 %; equivalent to a 0.3 Å decrease in d) increased $\kappa_\perp$ roughly four-fold to 0.7 W m^{-1} K^{-1}. This suggests that tweaking the interlayer spacing by applying pressure can alter the thermal conductivity and hence ρ in our r-TMD films. Moreover, this could potentially be a reversible effect.

In a previous study, Meng and Wang *et al.* showed that applying hydrostatic pressure to bulk MoS_2 up to 20 GPa to induce a compressive strain of 9 % can increase $\kappa_\perp$ from 3.5 to 25 W m^{-1} K^{-1}[123]. The researchers concluded that this was due to the increase in phonon group velocity in the Γ-A direction (Fig. 6.4B). Interestingly, the phonon group velocity did not change significantly along the in-plane Γ-M direction, which could suggest that $\kappa_{||}$ also did not change significantly (assuming material integrity is maintained).

We can envision that we can use this pressure to create a "thermal switch" in our r-TMD films, for which heat flowing in-plane will be redirected along the out-of-plane direction upon the application of pressure. The main challenge would be to scale up the thickness of r-MoS_2 such that the material does not leak heat through-plane, due to overall high extrinsic thermal *conductance* if the stacked film is *thin*, despite the low intrinic thermal *conductivity*. With its

larger anisotropy ratio, r-MoS_2 will have a higher fidelity as a thermal switch than bulk MoS_2, although a larger application of pressure will be necessary to reroute heat flow.

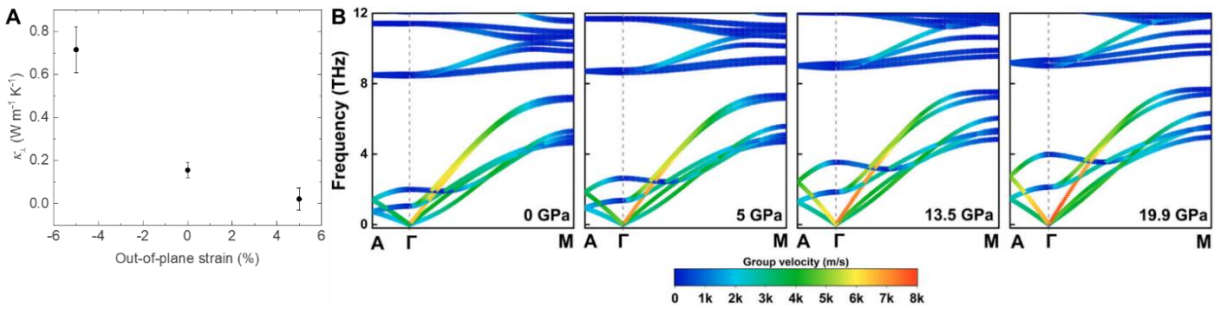

Figure 6.4 The effect of strain/interlayer spacing d/pressure on κ of r-MoS_2. (A) MD simulation results of $\kappa_\perp$ versus of out-of-plane strain for r-MoS_2. (B) First- principles calculations of the pressure induced change in the phonon dispersion and phonon group velocities in bulk MoS_2 along the through-plane (Γ-A) and in-plane (Γ-M) directions. The color gradient signifies the group velocities, with warmer colors indicating higher group velocities. The plots are reproduced from reference [23].

In the next section, we discuss the scalaility challenges of stacked 2D vDW films and recent progress made in this area.

6.5 Scalably thick, turbostratic vdW films

As alluded to previously, thermal conductance has more practical relevance than thermal conductvity, because the extrinsic property is the perceived measure by real-world materials and systems. To harness the ultralow through-plane thermal conductivity of r-TMD films, it is necessary to develop ways to scale up their fabrication to achieve sufficiently thick films.

To that end, our manual, layer-by-layer stacking method is not a practical strategy to generate thick, $N > 20$ films. Instead, our group's aforementioned robotic stacking setup is an alternative that is able to scalably generate 100 μm x 100 μm-area stacked TMD films, demonstrated up to $N = 80$ in thickness, all in an automated fashion and with a higher throughput[12]. Like our manual

stacking process, this robotic stacking technique is also solvent free and performed under vacuum, so it is similary able to generate clean interfaces.

Another method for the scaleable fabrication of thick 2D vdW stacks is the solution processing of exfoliated flakes from bulk crystals. These restacked films can be made to be micrometers thick and applied at an industrial, roll-to-roll scale. Liquid processing typically does not generate maximally turbostratic structures as does our MOCVD-manual stacking technique. The sonication exfoliation process typically generates flakes with thicknesses N = 2-10. Moreover, the use of solvent and intercalation compounds may trap contaminants between the exfoliated flakes. However, we note that these factors might not thwart the films' function that makes use of their ultralow thermal conductivity in the through-plane direction. Even if interlayer rotation occurs at every 2-10 layers given the flake thickness, the suppression in $\kappa_{\perp}$ may still be significant for a micrometer thick, N ~ 10,000 stacked film made up of restacked individual flakes of the same order of magnitude in number. The presence of contaminants may even further reduce $\kappa_{\perp}$ on top of the contribution of interlayer rotation.

To recreate a high ρ, the main challenge for solvent processed films is their small flake size and potential reduction in $\kappa_{||}$. Exfoliated flakes typically measure less than 1 μm across and more commonly tens of nanometers. Their properties are also usually diminished in performance compared to their single crystal counterparts. For example, some of the highest performing restacked graphene sheets stil have at least two orders of magnitude lower electrical conductivity than mechanically exfolatiated graphene [24,25]. While the thermal properties of these liquid processed, restacked graphene sheets have yet to be measured, future work in this area needs to

further optimize for the quality in-plane to retain or match the high ρ that the previous chapters in this thesis have demonstrated.

6.6 References

1. Cao, Y. *et al.* Unconventional superconductivity in magic-angle graphene superlattices. *Nature 2018 556:7699* **556**, 43–50 (2018).

2. Polshyn, H. *et al.* Electrical switching of magnetic order in an orbital Chern insulator. *Nature 2020 588:7836* **588**, 66–70 (2020).

3. Chen, G. *et al.* Tunable correlated Chern insulator and ferromagnetism in a moiré superlattice. *Nature 2020 579:7797* **579**, 56–61 (2020).

4. Wu, F., Lovorn, T., Tutuc, E., Martin, I. & Macdonald, A. H. Topological Insulators in Twisted Transition Metal Dichalcogenide Homobilayers. *Physical Review Letters* **122**, 086402 (2019).

5. Xu, Y. *et al.* Correlated insulating states at fractional fillings of moiré superlattices. *Nature 2020 587:7833* **587**, 214–218 (2020).

6. Burg, G. W. *et al.* Correlated Insulating States in Twisted Double Bilayer Graphene. *Physical Review Letters* **123**, 197702 (2019).

7. Regan, E. C. *et al.* Mott and generalized Wigner crystal states in WSe2/WS2 moiré superlattices. *Nature 2020 579:7799* **579**, 359–363 (2020).

8. Chen, G. *et al.* Signatures of tunable superconductivity in a trilayer graphene moiré superlattice. *Nature 2019 572:7768* **572**, 215–219 (2019).

9. Hao, Z. *et al.* Electric field–tunable superconductivity in alternating-twist magic-angle trilayer graphene. *Science (1979)* **371**, 1133–1138 (2021).

10. Park, J. M., Cao, Y., Watanabe, K., Taniguchi, T. & Jarillo-Herrero, P. Tunable strongly coupled superconductivity in magic-angle twisted trilayer graphene. *Nature 2021 590:7845* **590**, 249–255 (2021).

11. Liu, K. *et al.* Evolution of interlayer coupling in twisted molybdenum disulfide bilayers. *Nature Communications* **5**, (2014).

12. Mannix, A. J. *et al.* Robotic four-dimensional pixel assembly of van der Waals solids. *Nature Nanotechnology 2022* 1–6 (2022) doi:10.1038/s41565-021-01061-5.

13. Zhong, Y. *et al.* Wafer-scale synthesis of monolayer two-dimensional porphyrin polymers for hybrid superlattices. *Science (1979)* **366**, 1379–1384 (2019).

14. Wen, T. & Majetich, S. A. Ultra-large-area self-assembled monolayers of nanoparticles. *ACS Nano* **5**, 8868–8876 (2011).

15. Yun, H. & Paik, T. Colloidal Self-Assembly of Inorganic Nanocrystals into Superlattice Thin-Films and Multiscale Nanostructures. *Nanomaterials* **9**, (2019).

16. Huang, H., Chen, S., Gao, X., Chen, W. & Wee, A. T. S. Structural and electronic properties of PTCDA thin films on epitaxial graphene. *ACS Nano* **3**, 3431–3436 (2009).

17. Lee, S. *et al.* Anisotropic in-plane thermal conductivity of black phosphorus nanoribbons at temperatures higher than 100 K. *Nature Communications 2015 6:1* **6**, 1–7 (2015).

18. Lee, M. *et al.* Atomically Thin, Optically Isotropic Films with 3D Nanotopography. *Nano Letters* **21**, 7291–7297 (2021).

19. Levendorf, M. P. *et al.* Graphene and boron nitride lateral heterostructures for atomically thin circuitry. *Nature 2012 488:7413* **488**, 627–632 (2012).

20. Guimarães, M. H. D. *et al.* Atomically Thin Ohmic Edge Contacts between Two-Dimensional Materials. *ACS Nano* **10**, 6392–6399 (2016).

21. Xie, S. *et al.* Coherent, atomically thin transition-metal dichalcogenide superlattices with engineered strain. *Science (1979)* **359**, 1131–1136 (2018).

22. Erhart, P., Hyldgaard, P. & Lindroth, D. O. Microscopic Origin of Thermal Conductivity Reduction in Disordered van der Waals Solids. *Chemistry of Materials* **27**, 5511–5518 (2015).

23. Meng, X. *et al.* Thermal Conductivity Enhancement in MoS 2 under Extreme Strain. *Physical Review Letters* **122**, (2019).

24. Paton, K. R. *et al.* Scalable production of large quantities of defect-free few-layer graphene by shear exfoliation in liquids. *Nature Materials* **13**, 624–630 (2014).

25. De, S. *et al.* Flexible, Transparent, Conducting Films of Randomly Stacked Graphene from Surfactant-Stabilized, Oxide-Free Graphene Dispersions. *Small* **6**, 458–464 (2010).